C. elegans astrocytes mature in two phases from lineally distinct progenitors through CEH-43/DLX-mediated convergent transcription

Simin Liu (刘斯敏),[1] Kenneth Bradley,[1] Jinghong J. Tang (唐璟鸿),[1,2] Yoon A. Kim,[1] Ana Milosevic,[1] and Shai Shaham[1,*]

[1]Laboratory of Developmental Genetics, The Rockefeller University, New York, NY 10065, USA

[2]Present address: Lulu and Anthony Wang Laboratory of Neural Circuits and Behavior, The Rockefeller University, New York, NY 10065, USA

*Correspondence: shaham@rockefeller.edu

SUMMARY

Astrocytic glia regulate brain assembly, synapse formation/activity, neuronal energetics, and brain metabolism. Gene programs driving astrocyte specification are only partly understood. Here, we use lineage-restricted single-cell RNA sequencing to uncover a two-phase developmental program for *C. elegans* CEPsh astrocyte differentiation. In phase one, newly generated astrocytes acquire common transcription profiles despite arising from lineally and transcriptionally distinct progenitors. Convergent differentiation is mediated by the *distal-less* transcription factor CEH-43. CEH-43 is expressed in astrocytes and their progenitors, binds conserved astrocyte-expressed genes, and cell-autonomously controls astrocyte-specific gene expression. Forced misexpression of CEH-43 in the embryo promotes ectopic expression of astrocyte-specific reporters. The second gene expression phase, directing astrocyte maturation, is also under CEH-43 control. Homologs of CEPsh astrocyte-enriched genes are preferentially enriched in mammalian astrocytes, and the CEH-43 homologs DLX1/2 are expressed in mouse astrocytes. Our findings suggest parallels between CEPsh and mammalian astrocyte development, implicating conserved regulators in astrocyte cell-fate acquisition.

KEYWORDS

CEPsh astrocytes, Astrocyte Development, *Caenorhabditis elegans*, Convergent Differentiation, Glia Fate Specification, *ceh-43*, *DLX*, Single-cell Transcriptomics, Lineage Convergence, NanoDam

INTRODUCTION

Astrocytes are essential for central nervous system (CNS) development and function, where they promote neuronal survival[1] and play critical roles in synapse formation[2–5] and elimination[6,7], neurotransmitter recycling[8], ion and water homeostasis[9–12], neuronal cholesterol and nutrient supply[13–17], and modulation of synaptic transmission[18]. Astrocytes also associate with blood capillaries[19] and regulate blood–brain barrier integrity[20,21]. Possibly reflecting these diverse roles, astrocytes display a range of morphologies, gene expression profiles, and physiologies across the brain[22–24].

Lineage tracing studies suggest that mammalian astrocytes originate from bipolar radial glia (RG), the primary neuron and glia progenitors of the CNS. Following neurogenesis, RG give rise to gliogenic progenitors that divide locally to produce astrocytes[25]. The neurogenesis-to-gliogenesis transition is orchestrated by factors such as CNTF, LIF, CT-1[26–30], intracellular pathways including JAK–STAT[27], BMP[31], and Notch[32], as well as transcription factors *HES*, *NFIA*, *SOX9*, *ZBTB20*, *LHX2*, *ATF3*, and *RUNX2*[33–39]. *Pax6* and *Nkx6.1* regulate region-specific patterning of astrocyte subtypes in the spinal cord[40]. How these regulators interact to organize astrocyte specification is not well understood. Astrocytes can also arise directly from RG without cell division[41–43], and mechanisms driving this alternative differentiation route remain elusive.

Caenorhabditis elegans CEPsh astrocytes appear to share anatomical, morphological, and functional features with mammalian astrocytes. Each of the four mature CEPsh astrocytes extends ramified processes that ensheathe and infiltrate the central neuropil (the nerve ring), forming non-overlapping domains[44] reminiscent of mammalian astrocyte territorial tiling[45]. CEPsh astrocytes promote synaptogenesis[46],

contact synapses within the nerve ring[44], and in some instances ensheathe synapses in a tripartite-like configuration[47]. Mature CEPsh astrocytes express the conserved glial glutamate transporter *glt-1/EAAT2*. Loss of GLT-1 in CEPsh astrocytes or of its homolog GLT1/EAAT2 in mouse astrocytes results in repetitive behavior, suggesting common underlying functions[48,49]. Like some mammalian astrocytes, CEPsh astrocytes mature without cell division from bipolar RG-like precursors (early CEPsh astrocytes) whose processes serve as scaffolds that guide pioneer and follower neuron axon extension[50,51].

Although mature CEPsh astrocytes appear functionally and molecularly uniform, they originate from distinct embryonic lineages. Our prior work showed that while the Paired-box transcription factor VAB-3/Pax6/Pax7 is required for specifying mature CEPsh astrocytes irrespective of lineal origin[52], the homeobox transcription factor MLS-2/Nkx/Hmx selectively controls ventral CEPsh astrocyte maturation[52], perhaps reflecting dorsoventral differences in CEPsh astrocyte gene expression. Nonetheless, whether CEPsh astrocytes differ transcriptionally is not known, nor is it clear how they converge onto a common fate.

Here, we describe a lineage-restricted approach to temporally profile the transcriptomes of newly generated CEPsh astrocytes and their progenitors using single-cell RNA sequencing (scRNA-seq). We show that nascent dorsal and ventral CEPsh astrocytes are transcriptionally distinct but converge within ~90 minutes to a common transcriptional state. We identify several CEPsh astrocyte expressed genes required for convergent differentiation, including *ceh-43*, encoding a *distal-less* homeodomain transcription factor. *ceh-43* mutants exhibit impaired expression of CEPsh astrocyte gene reporters and display nerve ring axon guidance defects reminiscent of embryonic CEPsh

astrocyte ablation[50]. CEH-43 directly binds genes important for CEPsh astrocyte development and function, and its mis-expression is sufficient to drive ectopic CEPsh astrocyte reporter expression. Comparative transcriptome analyses reveal that nascent CEPsh astrocytes resemble early-stage mouse and human astrocytes. Notably, mouse DLX1 and DLX2, homologous to CEH-43, are expressed in cultured primary murine astrocytes and *in vivo*.

Our studies assemble a high-resolution transcriptional map of early CEPsh astrocyte generation and identify conserved regulators driving this developmental program. Similarities with mammalian astrocytes suggest that common programs may specify astrocytes across animal development.

RESULTS

A developmental transcriptome of early CEPsh astrocytes

scRNA-seq was previously used to profile the transcriptomes of *C. elegans* embryonic cells at three different time points[53], generating datasets that includes 127 embryonic CEPsh astrocytes. However, the temporal relationships and lineal origins of CEPsh astrocytes from these datasets cannot be resolved, and transcriptomes of some closely related sister or cousin cells were not identified. To generate a high-resolution developmental transcriptome of CEPsh astrocytes, we labeled embryonic sub-lineages that produce CEPsh astrocytes using fluorescent reporter combinations (**Figures 1A, 1B;** orange labels). Left (L) and right (R) dorsal CEPsh astrocyte lineages were co-labeled with *ceh-32p::H1-Wcherry* and *vab-3::mNeonGreen*, (**Figures 1A, S1A**), and ventral lineages with *ceh-36p::H1-Wcherry* and *sptf-1::TY1::EGFP* (**Figures 1B, S1B**). Embryos

were synchronized and collected at 240, 270 (ventral only), 330, or 420 minutes after the first post-fertilization cell division (Methods), time points that span CEPsh astrocyte birth at ~300 minutes[54]. Following embryo dissociation, co-labeled cells were isolated using fluorescence activated cell sorting (FACS) and processed for 10x Chromium scRNA-seq (**Figure 1C**). Cells from different strains and time points were processed separately to retain strain and time information (**Figure S2**).

After quality control (see Methods), 29,869 cells from the dorsal samples and 39,964 cells from the ventral samples were further analyzed (**Figures 1D, 1E**). To assess the precise embryo age from which individual cells were collected, we compared the transcriptome of each cell with a reference whole-embryo gene expression time course collected every 10 minutes until the onset of muscle movement and every 30 minutes thereafter[55]. Embryo age was assigned to the time point showing the highest similarity (**Figure S3**, see Methods). We found that for both ventral and dorsal lineages, cells plotted on a UMAP projection formed continuous trajectories correlating with embryo time (**Figures 1D, 1E,** temporal color coding), with 85% of the cells from dorsal samples and 76% of the cells from ventral samples assigned to 210-450 minutes, consistent with our embryo collection times (**Figures S2C, S2D**).

Cell types were annotated using published scRNA-seq data[53] and reporter expression patterns (**Table S1**). Ventral CEPsh astrocytes (CEPsh**V**) and progenitors were identified by *pros-1* expression and their lineage relationship to URA neurons marked by *cfi-1*[56] (**Figures S4A, S4B**). To validate annotations, we used a custom-built scanning iSPIM microscope[57,58] to track the embryonic expression patterns of four reporter transgenes. The patterns largely agree with scRNA-seq, aside from minor

discrepancies likely due to low level reporter expression not represented in the RNAseq data (**Figures S4C, S4D**).

The dorsal dataset comprises a more extensive diversity of cell types. To identify CEPsh**D** astrocyte lineages, we first partitioned cells by *pros-1* and *ham-2* expression (**Figure S4E**). *pros-1* was previously shown to be expressed in CEPshD astrocytes and their progenitors, ABarpaaaap and ABarpaaapa[53,59,60], whereas *ham-2* marks the OLQsoD glia progenitor ABarpaaaaa[53,60] (**Figures S4F, S4G**). CEPshD astrocytes were then distinguished from their OLQshD glia sister cells based on selective *aqp-7* and *lim-7* expression[60,61] (**Figures S4H, S4I**). CEPshD astrocytes and their progenitor identities were further validated using additional published marker gene lists[53] and by comparing their relative positions on the UMAP projection with the expected cell lineage structure (**Figures 1A, 1D, S4J-M**; see Methods).

As an independent validation, we identified differentially expressed genes[62] between CEPshD/V astrocyte progenitors and other progenitor cells and between CEPshD/V astrocytes and other terminal cells (**Figures 1F, 1G**). We find that cells annotated as CEPsh astrocytes and their progenitors are enriched for known glial regulators (e.g. *pros-1*, *mls-2*)[52,59], and are depleted for transcription factors that function in neuronal development (e.g. *ngn-1*, *hlh-16*, *ast-1*, *unc-86*)[63–68].

Cells we assigned as CEPsh astrocytes and their progenitors express at least 327 predicted DNA binding proteins[69,70]. We used RNA interference (RNAi) to knockdown 21 of these, including 13 enriched in CEPsh astrocytes (average $\log_2$FC > 0, adjusted p-value < 0.05), in RNAi-sensitized *eri-1(mg366)* animals[71] carrying a mature CEPsh astrocyte reporter, *hlh-17p::gfp*[52] (**Figure 1H, Table S2**). Knocking down nine of these

genes significantly reduces *hlh-17p::gfp* expression (**Figure 1I**), uncovering previously unknown regulators of CEPsh astrocyte fate. Of note, genomic mutations in *lin-26* and *ztf-29* also reduce *hlh-17p::gfp* expression in CEPsh astrocytes despite weak RNAi effects (**Figure S5**).

Together, these studies unveil a high-resolution transcriptional trajectory for CEPsh astrocyte development, revealing previously undescribed regulators of CEPsh astrocyte specification.

Nascent CEPsh astrocytes rapidly converge onto a shared transcriptional state

In development, terminal cells of similar type can arise from distantly related progenitors, but how this fate convergence takes place is not fully understood. Our scRNA-seq data presented an opportunity to study this question in the context of CEPsh astrocyte differentiation. To do so, we first characterized transcriptional differences between lineally distinct CEPsh astrocyte progenitors. Joint UMAP embedding of CEPsh astrocytes and their progenitors reveals three transcriptionally distinguishable progenitor cell types: the dorsal left (CEPsh**DL** progenitor), the dorsal right (CEPsh**DR** progenitor), and the ventral left/right (CEPshV progenitor) (**Figures 2A, 2B**). While CEPshDL and CEPshDR astrocyte progenitors initially exhibit distinct transcription profiles, these ultimately converge, as might be expected for cells giving rise to transcriptionally indistinguishable CEPshDL/R astrocytes (**Figure 2A**; lineage inset). Convergence is also evident from a comparison of transcription factor/DNA binding protein gene expression (**Figure 2B**, compare columns *a* vs. *c* and *b* vs. *d*. See **Table S3** for the complete gene expression profiles across clusters and **Table S13** for a complete list of transcription factors/DNA

binding protein genes[72,73]) and from more global differential gene expression analysis (**Figure 2C**). While left/right (L/R) differences are not evident between CEPsh**VL** and CEPsh**VR** astrocyte progenitors, these cells are markedly different from either CEPshDL/R astrocyte progenitors (**Figure 2A**; **Figure 2B** compare column *e* vs. columns *b* or *d*; compare **Figures 2D, 2E** vs. **Figure 2C**). Thus, CEPshD and CEPshV progenitors are transcriptionally distinct.

CEPshD astrocytes do not show measurable L/R gene expression differences (**Figure 2A**; note a single dorsal CEPshD (early) cluster). However, early CEPshD and CEPshV astrocytes are transcriptionally distinct, expressing different transcription factors and other genes (**Figure 2A**; **Figure 2B**, CEPshV (early) vs CEPshD (early) columns; **Figure 2F**). Remarkably, as early CEPshD and CEPshV astrocytes diverge from their sister cells (OLQshD and URAV, respectively; **Figures 2A, 2B; S6A-C**), they converge onto a common state within ~1-1.5 hours (Converged CEPsh astrocytes in **Figures 2A, 2B**). The 239 genes enriched in converged CEPsh astrocytes are upregulated in both CEPshD and CEPshV astrocytes (**Figure 2G**), with expression levels of individual genes showing strong positive correlations (**Figure S6D**). These genes are also expressed in ditional embryonic cells, suggesting that CEPsh astrocyte fate convergence is a result of combinatorial gene expression.

Genes enriched in the converged CEPsh astrocyte gene set have roles in neurodevelopment and tissue morphogenesis (**Figure 2H, Table S4**), and include membrane proteins important for axon growth, synaptogenesis, and nerve ring formation[50,74–78], a process we previously showed to be mediated by embryonic CEPsh astrocytes (**Figure 2I**). The expression of these genes is transient and diminishes in

adulthood[79] (**Figure 2J**). By contrast, 377 genes enriched in L2-L3 CEPsh astrocytes ($\log_2$FC > 1, adjusted p-value < 0.05)[48], or 323 genes enriched in adult CEPsh astrocytes ($\log_2$FC > 0, adjusted p-value < 0.05)[79] (**Table S5**), show little or no expression in converged CEPsh astrocytes and are not upregulated as CEPshD/V transcription profiles merge (**Figures 2J, S6E-G**). These results suggest a two-phase maturation program for CEPsh astrocytes (**Figure 2J**). In phase I, a transcriptional program supporting nerve ring assembly is induced[50], reminiscent of radial glial roles in neuronal migration and axon extension[80,81]. While in phase II, a distinct program is turned on that mediates the morphological transition of CEPsh astrocytes from bipolar to ramified cells that regulate neuronal activity (**Figure 2J**).

CEH-43 promotes CEPsh astrocyte differentiation

Two models can explain how lineally and transcriptionally divergent nascent CEPsh astrocytes ultimately converge in gene expression: in one, the transcription of convergently expressed genes is driven by either dorsal-specific or ventral-specific transcription factors that bind different, yet functionally equivalent, regulatory sequences in these genes. Alternatively, a handful of transcription factors shared between dorsal and ventral nascent CEPsh astrocytes bind the same elements in target genes, promoting convergent expression. Supporting the latter model, we identified transcription factors expressed in both CEPshD and CEPshV astrocyte progenitors and in nascent CEPshD and CEPshV astrocytes (**Figures 2B, 3B**). Among these is CEH-43, whose knockdown in our RNAi screen disrupted expression of the *hlh-17p::gfp* CEPsh astrocyte reporter (**Figure 1I**).

CEH-43 is a *distal-less* homeobox transcription factor orthologous to mammalian DLX proteins[82] (**Figure 3A**). An *SL2::GFP::H2B* transcriptional reporter integrated using CRISPR/Cas9 downstream of the *ceh-43* stop codon is continually expressed in all CEPsh astrocytes through adulthood (**Figures 3B, 3C**), consistent with *ceh-43* detection in both embryonic and adult CEPsh astrocytes using scRNAseq[79]. A *ceh-43(ot406)* missense mutation, predicted to change a single amino acid in the carboxyl terminus of the CEH-43 homeodomain (**Figure 3A**), blocks *hlh-17p::gfp* expression in most CEPsh astrocytes (**Figures 3D-F**) and causes defects in CEPsh astrocyte positioning and process morphology (**Figure S7A**). Nonetheless, *ceh-43(ot406)* mutants expressing the *mir-228p::2xNLS::iBlueberry* pan-glia reporter have the same number of head glia as wild-type animals (**Figures S7B, S7C**). Thus, although CEPsh astrocytes exhibit aberrations in morphology, cell placement, and gene expression, some aspects of their glial identity are not disrupted in this mutant.

To confirm that *ceh-43* disruption leads to loss of *hlh-17p::gfp* expression, we introduced a *ceh-43* fosmid (WRM0633Cc03, **Figure 3A**) into *ceh-43(ot406)* mutants. The fosmid restores *hlh-17p::gfp* expression to mature CEPsh astrocytes in three independent rescue lines (**Figure 3F**). *hlh-17p::gfp* expression is also restored by a PCR amplicon containing the endogenous *ceh-43* genomic locus including sequences 10 kb upstream of the start codon and 1.2 kb downstream of the stop codon (*ceh-43p::ceh-43*; **Figures 3A, 3G**). Thus, *ceh-43* is the gene responsible for CEPsh astrocyte defects.

CEH-43 is required for nerve ring assembly

During embryonic development, the *C. elegans* nerve ring is hierarchically assembled: CEPsh astrocyte processes extend to demarcate the presumptive nerve ring and guide sublateral (SubL) neuron axon extension into the neuropil[50]. Both cell types then cooperatively guide nerve ring entry of follower axons, such as AIY neuron axons[50]. Ablation of CEPsh astrocytes shortly after they are born results in aberrant SubL axon extension as well as failure of follower neuron nerve ring entry[50]. We found that c*eh-43(ot406)* mutants phenocopy CEPsh astrocyte ablation. In wild-type animals, SubL neuron axons labeled with *ceh-24p::gfp* enter the nerve ring and extend posteriorly (**Figure 4A**), but in c*eh-43(ot406)* mutants, SubL axons exhibit aberrant anterior processes (**Figures 4B, 4C, S8A-B**) and other defects (**Figures S8C-G**). Likewise, AIY axons fail to enter the nerve ring in c*eh-43(ot406)* mutants (**Figures 4D, 4E, S8H-L**). The latter defects are rescued by a 14 kb *ceh-43* genomic fragment, confirming that the *ceh-43* lesion is responsible for the nerve ring defects observed (**Figure 4F**). Notably, published[53] scRNA-seq data, as well as scRNA-seq data presented here, show that *ceh-43* is not expressed in embryonic SubL or AIY neurons, consistent with CEH-43 acting in CEPsh astrocytes.

CEH-43 functions cell autonomously in early CEPsh astrocytes

Our finding that a *ceh-43::SL2::GFP::H2B* endogenous reporter is expressed in CEPsh astrocytes (**Figure 3C**) suggests that *ceh-43* functions cell autonomously for CEPsh astrocyte fate determination. To further test this, we generated *ceh-43(ot406)*; *hlh-17p::gfp* mutants carrying an unstable extrachromosomal array consisting of a *ceh-43* fosmid and a ubiquitous *nhr-2p::H1-mCherry* reporter that allows tracking of cells

inheriting the fosmid (**Figure 5A**). Among CEPsh astrocytes carrying the array (mCherry+), 86% (96/111) express *hlh-17p::gfp* (**Figures 5B, 5D**). Importantly, 96/96 CEPsh astrocytes expressing *hlh-17p::gfp* carried the rescuing fosmid (mCherry+) (**Figures 5B, 5E**), while 0/6 that did not, lacked the array (**Figures 5C, 5F;** mCherry-). Similar results are obtained with the *ceh-43(tm480)* deletion allele (**Figures 3A, 5G–I**) or with a pan-glia *mir-228* promoter::*ceh-43* cDNA extrachromosomal transgene (**Figures S7F–N**). *mir-228* is expressed in CEPsh astrocytes but not in their progenitors (**Figure S7O**). Thus, *ceh-43* likely acts in CEPsh astrocytes and not in lineally related neurons, epithelial cells, or progenitors.

Consistent with this conclusion, *pros-1* is expressed in both CEPsh astrocytes and their progenitors (**Figure S7D**), and a *pros-1*p::*ceh-43* cDNA transgene, containing 4.2 kb of *pros-1* upstream regulatory sequences, partially, but significantly, rescues *ceh-43(ot406)*; *hlh-17p::gfp* mutants, as does a transgene with a 2 kb *mir-228* regulatory sequence (**Figure 5J**). However, a *sox-2*p::*ceh-43* cDNA transgene containing 3.9 kb of upstream regulatory sequences from the *sox-2* gene, expressed primarily in CEPsh astrocyte progenitors (**Figure S7E**), does not restore *ceh-43* function (**Figure 5J**).

CEH-43 expression is sufficient to induce embryonic CEPsh astrocyte gene expression

CEH-43 could function permissively, allowing other cell-specific regulators to control CEPsh astrocyte gene expression. Alternatively, CEH-43 may directly control CEPsh astrocyte gene expression. To distinguish between these possibilities, we ectopically expressed *ceh-43* cDNA using an *hsp-16.41* heat-shock inducible promoter in embryos

carrying the *hlh-17p::gfp* reporter transgene (**Figures 5K-N**). We found a modest increase in the number of *hlh-17p::gfp*-positive cells in *hsp-16.41p::ceh-43* transgenic embryos even without heat shock, likely due to leaky expression (**Figures 5L, 5O**). Upon heat shock, *hlh-17p::gfp* ectopic expression is further increased (**Figures 5N, 5O**), suggesting that CEH-43 directly regulates CEPsh astrocyte gene expression.

Heat-induced *ceh-43* expression in L4 larvae does not induce ectopic *hlh-17p::gfp* expression (**Figures 5P-T**), suggesting that *ceh-43* may only have the capacity to control CEPsh astrocyte gene expression in embryos. To test this idea further, we introduced a 3xGAS::GFP-AID (auxin-inducible degron[83,84]) tag at the C-terminus of the endogenous *ceh-43* locus in animals ubiquitously expressing the TIR1 E3 ligase, which mediates auxin-induced protein degradation (*eft-3p::TIR1-mRuby*, **Figure S9A**). 4 mM Auxin treatment of early L1 stage animals induces almost complete CEH-43::3xGAS::GFP::AID degradation within 2 hours (**Figure S9B**), but has no effect on *hlh-17p::gfp* expression in CEPsh astrocytes (**Figures S9C-G**). Similarly, auxin induced degradation of CEH-43 has little effect on larval expression of the CEPsh astrocyte gene *glt-1* (**Figures S9H-L**). Thus, CEH-43 is required during embryogenesis to establish CEPsh astrocyte gene expression but is largely dispensable for maintenance of target gene expression. Alternatively, CEH-43 may maintain the expression of some CEPsh astrocyte genes, but not others.

CEH-43 binds genes expressed during both phases of CEPsh astrocyte development

If CEH-43 actively controls CEPsh astrocyte gene expression, its targets should play important roles in CEPsh astrocyte biology, given the phenotypic consequences of *ceh-*

43 inactivation. To test this, we used the NanoDam method[85] to identify CEH-43 target genes *in vivo* (**Figure 6A**). Briefly, we generated animals in which *gfp* coding sequences are endogenously fused to the *ceh-43* gene and which also carry an *hsp-16.2*p::Dam-GFP Nanobody transgene, containing a fusion of *E. coli* Dam methyltransferase to GFP nanobody sequences (modified from [86]). Association of Dam-GFP Nanobody with CEH-43::GFP protein bound to DNA promotes methylation of adenine residues in 5'-GATC-3' motifs. Mapping methylated sites then allows *in vivo* CEH-43 binding loci to be identified. Since *C. elegans* DNA is normally unmethylated[87], the assay provides a high signal-to-noise ratio. Importantly, because methylation leaves a permanent signature, collecting L4 animals allows identification of both embryonic and postembryonic CEH-43 targets.

We collected two biological replicates from L4 animals, which show strong concordance (**Figure S10**). We then examined the genomic distribution of CEH-43 binding peaks (called at a false discovery rate (FDR) $<10^{-25}$ (**Figure S10**))[85]. Consistent with a role in transcriptional control, CEH-43 binding peaks are enriched upstream of transcription start sites (TSS; **Figure 6B**). 97% of binding peaks are located in non-exonic regions, even though these regions comprise only 75.8% of the genome and are less likely to contain GATC motifs than exons (predicted ratio of 1:1.39[88]; **Figure 6C**). Moreover, 361 target genes identified using NanoDam overlap with CEH-43 chromatin immunoprecipitation sequencing (ChIP-seq) targets reported in mixed-stage embryos[89] (**Figure 6D**).

Cross referencing NanoDam predicted CEH-43 binding sites with our scRNA-seq embryonic CEPsh astrocytes data identifies 111 high-confidence embryonic CEH-43 targets (**Figure 6D, Table S6**). Gene ontology analysis reveals enrichment for genes

involved in asymmetric cell division, fate commitment, migration, and Wnt signaling (**Figure 6E**). Examples include *pop-1*, a Wnt signaling target regulating asymmetric cell division[90]; *sox-2*, involved in neuron fate specification[91]; and *vab-3*, involved in CEPsh astrocyte fate determination[52] (**Figure 6F**). Other target genes include *fmi-1*, encoding an adhesion GPCR Flamingo/CELSR/ADGRC protein, and *kpc-1*, encoding a Furin-like protease, both required in CEPsh astrocytes to promote nerve ring axon extension[50] (**Figure 6F**).

To assess whether CEH-43 also binds genes expressed in the second phase of CEPsh astrocyte maturation, we compared our NanoDam gene list with a list of genes expressed post-embryonically in CEPsh astrocytes[79] and identified 324 putative targets (**Figure 6G, Table S7**). Among these, *glt-1*, encoding a glutamate transporter homologous to mammalian GLT1/EAAT2, is highly expressed (**Figure 6H**). However, *glt-1* was not identified as a target in published CEH-43 ChIP-seq studies of mixed-stage embryos[89], nor is it expressed in our converged embryonic CEPsh astrocyte dataset. Importantly, expression of a *glt-1p::gfp* reporter in CEPsh astrocytes is significantly reduced in *ceh-43(ot406)* mutants (**Figures 6J-Q**). Thus, CEH-43 controls expression of genes during both phases of CEPsh astrocyte maturation (**Figure 2J**).

To determine when CEH-43 is required for *glt-1* expression, we treated CEH-43::AID; *glt-1p::gfp* early L1 larvae with auxin. This, however, has little effect on *glt-1p::gfp* reporter expression (**Figures S9H-L**). We conclude, therefore, that because *glt-1p::gfp* is already expressed in early L1 larvae prior to auxin treatment, CEH-43 likely acts in the embryo or in very early L1 larvae to initiate *glt-1p::gfp* expression and is dispensable for

its maintenance. More broadly, these findings suggest that the second phase of CEPsh astrocyte maturation (**Figure 2J**) is initiated in embryos or in very early L1 animals.

Finally, we note that *eat-6*, homologous to mammalian *ATP1A2*, encoding the astrocytic Na+/K+ ATPase α2, is co-expressed with *glt-1* in adult CEPsh astrocytes[79] and is bound by CEH-43 (**Figure S10C**). Mammalian α2 is essential for maintaining astrocytic Na+ homeostasis, which supports GLT1- and GLAST-mediated glutamate uptake[92–94]. Loss of α2 impairs glutamate clearance and is linked to cortical dendritic hyperexcitability and cranial pain in familial hemiplegic migraine mouse model[95]. The co-expression and co-regulation of *eat-6* and *glt-1* by CEH-43 suggests conserved mechanisms of astrocytic glutamate regulation in *C. elegans*.

Gene expression similarities between *C. elegans* and mammalian astrocytes

Developmental, morphological, and functional parallels between *C. elegans* CEPsh astrocytes and mammalian astrocytes[96] raise the possibility that these cell types express homologous genes. To investigate this, we reanalyzed published single-cell datasets of cultured human glial progenitor cells, human induced pluripotent stem cells (iPSC), and mouse embryonic stem cells (mESCs) undergoing differentiation[97,98] (**Figure 7A**; Wang et al., Frazel et al. (Human), and Frazel et al. (Mouse), respectively). Using criteria reported in the original publications, we identified early astrocyte and neuronal clusters (**Figures S11A-F**). From each dataset, we identified the 50 highest expressed neuron- or astrocyte-enriched genes with *C. elegans* orthologs (**Table S8-S10**), and examined normalized average gene expression for these orthologs across CEPsh astrocyte lineages (**Figure 7A** bottom; see Methods).

We found that genes in all three ortholog sets are enriched in converged CEPsh astrocytes, moderately enriched in nascent CEPsh astrocytes, and not enriched in progenitors (**Figures 7B-D**). Orthologs of mammalian astrocyte-enriched genes are also enriched in *C. elegans* OLQshD glia, but either not enriched or slightly enriched in *C. elegans* URAV neurons. By contrast, neuron-enriched orthologs are significantly enriched in URAV neurons but not in converged CEPsh astrocytes in two of the three datasets (**Figures 7B-D**).

We also compared the entire list of astrocyte-enriched genes from each of the three mammalian datasets with genes enriched in converged CEPsh astrocytes (**Figures 7E-G, Table S11**). The combined set of overlapping genes (**Figure 7H**) includes sodium/potassium-transporting ATPase subunits (*eat-6/ATP1A2*, *nkb-3/ATP1B2*), cell adhesion molecules (*lec-1/3/LGALS3*, *wrk-1/NEGR1*), intercellular signaling components (*slt-1/SLIT1/2*), GFAP-related genes (*ifa-1*, *ifa-4*, *ifb-1*), aquaporins (*aqp-2,7/AQP4*) and other genes (**Figure 7H**). Many of these genes also contain CEH-43 NanoDam binding peaks, implicating CEH-43 in the control of a core astrocytic gene expression program (**Figure 7H**). Thus, despite their evolutionary distance, gene expression similarities between mammalian and *C. elegans* astrocytes are evident.

The CEH-43 homologs DLX1 and DLX2 are expressed in mammalian astrocytes

We specifically examined whether *C. elegans* and mammalian astrocytes express common transcription factors, as these are often indicators of cell-type specificity. Of 327 transcription factors expressed in CEPsh astrocytes or their progenitors, 201 have one or more identifiable mouse or human orthologs. Of 671 putative human homologs, 323 and

318 are expressed in the Wang et al.[97] and Frazel et al.[98] astrocyte datasets, respectively. Of 551 putative mouse orthologs, 317 are expressed in the Frazel et al. dataset[98] (**Figure S11G, Table S12**). Shared factors included *NFIA*, a regulator of astrocyte generation[33–35]; *TCF7L2*[99], involved in astrocyte maturation; and *PROX1/prospero*, a regulator of glia development in *Drosophila* and mice[100,101] (**Figure S11H**). Although *C. elegans* lacks a direct *SOX9* ortholog, related *Sox* family members (*sox-2* and *sem-2*) are expressed in CEPsh progenitors, and SOX-2 is the *C. elegans* protein most similar to mammalian *SOX9*.

Inspection of the mammalian datasets also reveals that both DLX1 and DLX2, homologs of *C. elegans* CEH-43, are expressed in a subset of astrocytes (**Figure S11H**). This is a surprising finding given previously described roles for these proteins in dopaminergic and GABAergic neuron differentiation[102–105]. To directly confirm this, we stained fixed primary astrocytes isolated from embryonic mouse brain with antibodies against DLX1 or DLX2. Remarkably, both proteins are detected. Expression is largely confined to nuclei, as expected for transcription factors (**Figures 7I-P**). We also examined DLX1 and DLX2 localization *in vivo*. We found that in the retrosplenial cortex of adult JD130 (*Aldh1l1-EGFP/Rpl10a*) mice, DLX1 but not DLX2 is detected in astrocyte nuclei (**Figures 7Q, 7R**). These findings suggest that, like CEH-43, DLX1 and DLX2 may regulate astrocyte gene expression during early mammalian astrocyte development. Of note, we found that DLX1 and DLX2 are not expressed in all astrocytes, consistent with the mammalian gene expression datasets in which only some astrocytes appear to express DLX1 or DLX2 (**Figure S11H**).

DISCUSSION

We present here a high-resolution transcriptomic analysis of the early stages of *C. elegans* CEPsh astrocyte development. Our studies reveal that CEPsh astrocyte maturation involves at least two distinct phases (**Figure 2J**). In the first phase, early embryonic CEPsh astrocytes express a battery of genes implicated in cell adhesion and axon guidance, consistent with our previous findings demonstrating pioneer roles for early embryonic CEPsh astrocytes in nerve ring assembly[50]. In the second phase, which likely begins prior to animal hatching and once nerve ring assembly is sufficiently advanced, CEPsh astrocytes express a substantially different gene set that includes genes involved in regulating neuronal activity[48,79]. We uncover the *distal-less* transcription factor CEH-43 as an important regulator of CEPsh astrocyte gene expression in both phases of differentiation, controlling early expression of FMI-1/Flamingo/CELSR and other nerve ring assembly proteins, as well as later expression of the glutamate transporter GLT-1/EAAT2 which modulates animal reversal locomotion patterns.

Parallels between *C. elegans* CEPsh astrocyte and mammalian astrocyte development

While many CNS astrocytes are thought to arise from local transiently amplifying progenitor cells derived from radial glia[51], other astrocytes arise directly from radial glia without cell division[41,42,51]. In the latter case, bipolar radial glia, which guide neuronal migration and axon extension, remodel to acquire the signature ramified and tufted morphology of astrocytes, just as bipolar axon-guiding early CEPsh astrocytes remodel in shape[50] and gene expression (this work and [48,79]). Very little is known about

mechanisms controlling the direct radial-glia-to-astrocyte route, and our findings raise the possibility that these mechanisms may be conserved. Indeed, by comparing the transcriptomes of early CEPsh astrocytes to those of newly generated mammalian astrocytes produced from cultured iPSCs or stem cells, we demonstrate a significant enrichment of orthologous genes.

Consistent with this idea, we show that the CEH-43 homologs DLX1 and DLX2 are expressed in early mouse astrocytes, and DLX1 is expressed *in vivo* in adult mouse astrocytes in brain slices, in line with data from large-scale gene expression studies[24,106]. Both mammalian proteins are implicated in dopaminergic neuron development[103,104], a role shared with CEH-43, which controls *C. elegans* dopaminergic neuron specification[107], and in GABAergic neuron development[102,105]. However, their roles in astrocytes are unknown, although expression of DLX2 in astrocyte progenitors has been reported[108], and forced expression of DLX2 can convert astrocytes back to neuroprogenitors[109]. It may be that like CEH-43, which is expressed in CEPsh astrocytes but also in their immediate progenitors, DLX1/2, expressed in astrocytes and their progenitors, regulates astrocyte specification.

Additional evidence supporting conserved roles of DLX transcription factors comes from our NanoDam experiment mapping CEH-43 bound genes. Among these are genes encoding the transcription factors *vab-3*/Pax6 and *pop-1*/TCF. We previously showed that VAB-3/PAX6 is required for CEPsh astrocyte differentiation[52], and studies of the mouse olfactory bulb reveal that DLX2 cooperates with PAX6 to promote dopaminergic neuron fate[104]. POP-1/TCF functions downstream of Wnt/β-catenin signaling to mediate asymmetric cell divisions during development[110,111], and interactions between DLX and

Wnt signaling occur in vertebrate neural progenitors[112]. Thus, it is possible that not only DLX proteins, but additional conserved transcription factors work together in both *C. elegans* and vertebrates to coordinate astrocyte specification.

CEH-43/DLX instructively initiates CEPsh astrocyte gene expression

We demonstrate that CEH-43 directly binds to genes whose expression it controls, and that CEH-43 is expressed in CEPsh astrocytes throughout the lifetime of the animal. Furthermore, many other cells that express CEH-43 are glia. These findings raise the possibility that CEH-43 may be a terminal selector transcription factor, directly regulating cell-type-specific gene expression[113–116]. Yet, unlike terminal selectors, which also maintain cell-type-specific gene expression, postembryonic auxin-induced degradation of CEH-43 appears to have little or no effect on maintenance of CEPsh astrocyte gene expression. Furthermore, ectopic expression of CEH-43 in embryos, but not in larvae, yields ectopic target gene expression, suggesting that CEH-43 instructively drives gene expression only when terminal gene expression is first established. Thus, CEH-43 does not appear to function as a classical terminal selector.

Might CEH-43, instead, be a lineage-selective transcription factor? These regulators are expressed in terminal cells related by lineage and not necessarily by function. Lineage-selective transcription factors are implicated in development of the *C. elegans* inner labial socket (ILso) glia[117]. The six ILso glia arise from three distinct lineages, and the Forkhead transcription factor UNC-130 is specifically required for generating dorsal, but not ventral or lateral, ILso glia[117]. Supporting this notion, CEH-43 is expressed in all terminal cells derived from some early progenitors (e.g. ABarap,

ABalpp, and others[60,118]). However, because CEH-43 is also expressed in smaller sub-lineages that give rise to only two or four progeny cells (e.g. ABarpaaaa, ABalaaapar[60,118]), it may not act as a lineage-specific factor in all cases. Since CEH-43 shares only some features of terminal selector and lineage-selective transcription factors, we suggest that it may function differently in different contexts.

The control of convergent differentiation

Our studies reveal that nascent CEPshV and CEPshD astrocytes differ significantly in gene expression, reflecting the transcriptional and lineal differences of their immediate progenitors. Yet, within about an hour, the transcriptional repertoire of these cells converges, even as they each become distinct from their sister cells. Convergence of cells from disparate lineages onto similar functional states is common in *C. elegans* and in other animals, but the mechanisms are still incompletely understood. Our studies suggest that CEH-43, expressed in progenitors and early CEPsh astrocytes of both dorsal and ventral lineages, plays an important role in driving transcriptional convergence. However, convergence may not necessarily be reliant on common transcription factors. We previously reported that mutations in the HMX-factor MLS2 differentially affects gene expression in dorsal and ventral CEPsh astrocytes[52]. This finding suggests that cells originating from different lineages may also utilize different transcription factors to produce the same terminal cell fate. This alternative mechanism appears to require extensive evolutionary engineering to equip each target gene with separate binding sites for lineage-specific transcription factors. Thus, genes regulated by this mechanism may have been later additions to the gene expression profile of CEPsh astrocytes.

Lineage-restricted scRNA-seq for transcriptome tracking in development

Our study highlights the power of lineage-restricted single-cell transcriptome analysis in resolving cell-type-specific developmental trajectories. Although comprehensive single-cell atlases of *C. elegans* embryogenesis and the development of other animals are available[53,55,119–122], these global datasets do not always offer the temporal and lineage resolution necessary to dissect dynamic cell-specific transcriptional changes within a narrow developmental window. This can result from the small number of cells representing each cell type or stage, leading to ambiguities in assigning largely similar cell types.

We show that by focusing on specific lineages giving rise to cells of interest at key developmental time points, we resolve individual cell division and cell fate convergence events. An important feature of our strategy is the collection of embryos roughly staged at several developmental times, such that the developmental timing distribution due to staging inaccuracies is of the same order as the separation between time points collected. Knowing the developmental time bin from which transcriptomes were generated allowed us to corroborate time arrows predicted based on computational relatedness of cells. Although embryo staging was not exact, it gave us a highly continuous developmental trajectory, with cells representing essentially every time point between the first and last stages investigated. Indeed, we estimate a resolution of ~1-2 min over a nearly four-hour experimental time span. In our studies, cells belonging to a certain lineage were isolated by FACS based on reporter transgene expression. However, it should be possible to

bypass sorting and identify cells from a certain lineage *post hoc* through the detection of reporter transgene mRNAs within the single-cell transcriptomes.

Limitations of the study

The transcriptome profiles were generated using 3'-end sequencing, which limits detection of alternative mRNA isoforms. Furthermore, some of our functional analyses relied on assaying CEPsh astrocytes reporter transgene expression, which may only partially reflect the endogenous CEPsh astrocyte gene regulation. Finally, while our comparative analysis identified conserved genes enriched in both CEPsh astrocytes and mammalian astrocytes, some of which are direct *ceh-43* targets, further studies will be needed to determine whether DLX factors similarly regulate their mammalian orthologs during astrocyte development.

RESOURCE AVAILABILITY

Lead contact

Further information and requests for resources and reagents should be directed to and will be fulfilled by the lead contact, Shai Shaham (shaham@rockefeller.edu).

Materials availability

Plasmids and strains generated in this study are available by contacting Shai Shaham (shaham@rockefeller.edu).

Data and code availability

- Raw single-cell RNA-seq data and NanoDam sequencing data have been deposited to DDBJ at PRJDB37786 and is publicly available as of the date of publication.

- Microscopy data reported in this paper will be shared by the lead contact upon request.
- Processed data and original code have been deposited to Zenodo (DOI: 10.5281/zenodo.17114839) and is publicly available as of the date of publication.
- Any additional information required to reanalyze the data reported in this paper is available from the lead contact upon request.

ACKNOWLEDGMENTS

We thank members of the Shaham lab for comments on the manuscript and discussions; Dr. John I. Murray for sharing the code for embryo time analysis; Dr. Andrea Brand for sharing the NanoDam plasmid; and Dr. Peter Meister for sharing DamID strain IS3675. Some strains were provided by the CGC, which is funded by NIH Office of Research Infrastructure Programs (P40 OD010440). FACS was performed at the Rockefeller University Flow Cytometry Resource Center (RRID:SCR_017694), and single-cell library preparation and sequencing was performed at the Rockefeller University Genomics Resource Center (RRID:SCR_020986). Some analyses were performed on computational resources from the Rockefeller University High Performance Computing Resource Center (RRID:SCR_025889). This work was funded by NIH grant R35NS105094 to S.S. S.L. is a Kavli Neural Systems Institute graduate fellow.

AUTHOR CONTRIBUTIONS

S.L. and S.S. conceptualized the study. S.L. performed all scRNA-seq and NanoDam experiments and conducted the computational analyses with conceptual input from S.S. S.L. performed functional experiments. K.B. carried out the *ztf-29* mutant experiment.

J.J.T. characterized AIY neuron defects. Y.A.K. performed the DLX1/2 cell culture antibody staining experiments. A.M. performed antibody staining on mouse brain slices. S.L. wrote the original manuscript draft. S.L. and S.S. reviewed and edited the manuscript. S.S. acquired funding and supervised the study.

DECLARATION OF INTERESTS

The authors declare no competing interests.

DECLARATION OF GENERATIVE AI AND AI-ASSISTED TECHNOLOGIES

ChatGPT was used to polish text for clarity in preparing the first draft this work. Authors subsequently extensively reviewed and edited the manuscript and take full responsibility for the content of the publication.

SUPPLEMENTAL INFORMATION

Document S1. Figures S1–S11, and supplemental references

Table S1. Marker genes for ventral dataset annotation

Table S2. RNAi screen raw data and statistics

Table S3. Gene expression profiles across clusters of the CEPshD and CEPshV lineages

Table S4. Converged CEPsh astrocyte enriched genes

Table S5. Genes enriched in L2-L3 or adult CEPsh astrocytes

Table S6. Embryonic CEH-43 targets identified by overlapping NanoDam, ChIP-seq, and scRNA-seq gene lists

Table S7. Genes expressed in adult CEPsh astrocytes and potential CEH-43 targets

Table S8. Top 50 astrocyte- and neuron-enriched genes with *C. elegans* orthologs (Wang et al., 2025)

Table S9. Top 50 astrocyte- and neuron-enriched genes with *C. elegans* orthologs (Frazel et al., 2023, human)

Table S10. Top 50 astrocyte- and neuron-enriched genes with *C. elegans* orthologs (Frazel et al., 2023, mouse)

Table S11. Shared enriched genes between converged CEPsh astrocytes and mammalian astrocytes

Table S12. Transcription factors expressed in CEPsh astrocytes and progenitors, and their conservation in mammalian datasets

Table S13. Transcription factor/DNA binding protein list

FIGURE TITLES AND LEGENDS

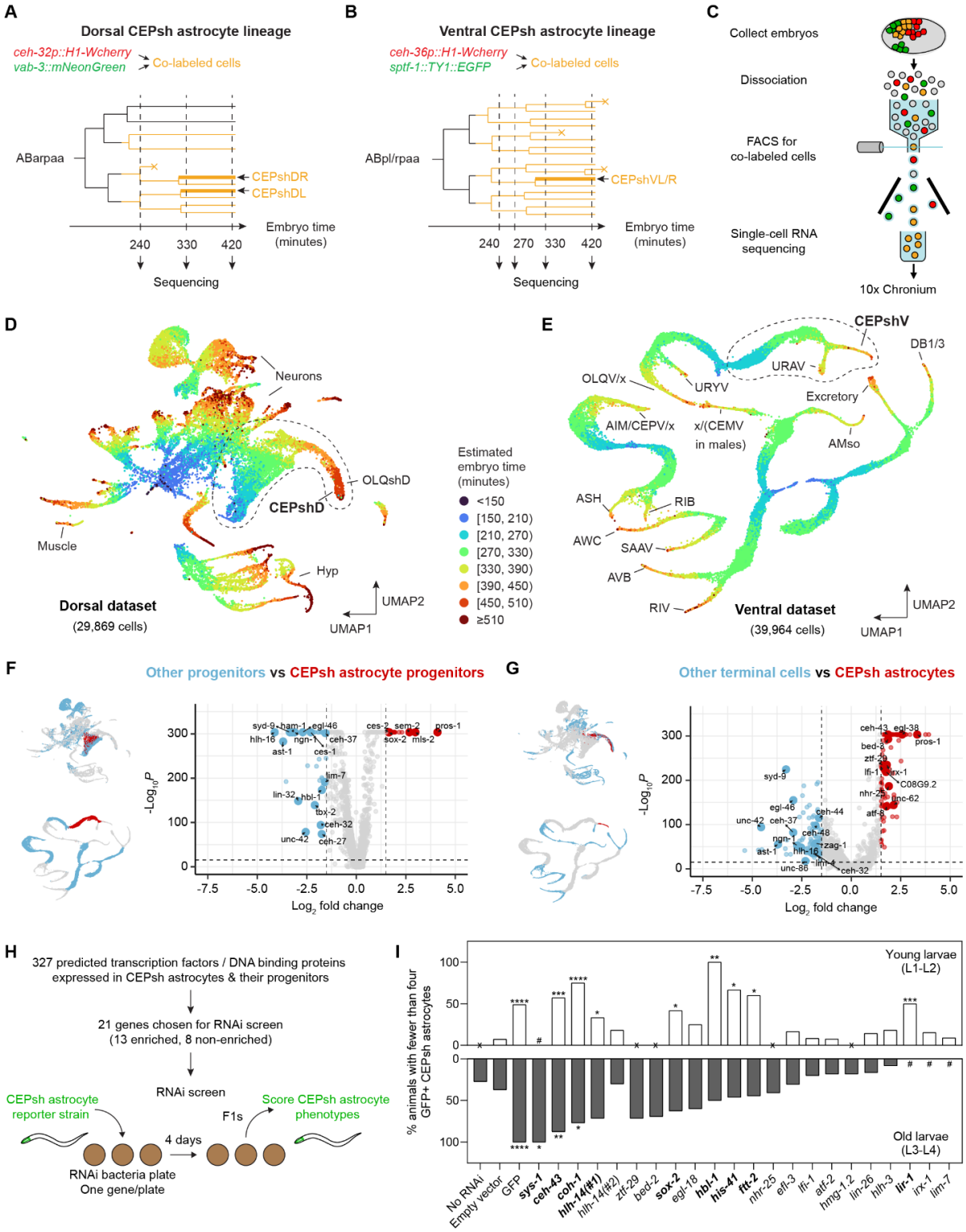

Figure 1. A developmental transcriptome of early CEPsh astrocytes

(A) Strategy for isolating developing dorsal CEPsh astrocytes. Cells from dorsal CEPsh astrocytes lineages were co-labeled with the two indicated fluorescent reporters. Synchronized embryos were collected at the indicated developmental time points.

(B) Same as (A) but for ventral CEPsh astrocytes.

(C) Workflow outlining FACS isolation of co-labeled cells followed by single-cell RNA sequencing.

(D) UMAP projection of 29,869 cells from the dorsal dataset. Each cell is color-coded by the estimated developmental age of the embryo from which the cell was isolated. The sub-lineage containing CEPshD astrocytes and their progenitors is circled.

(E) UMAP projection of the 39,964 cells from the ventral dataset. The sub-lineage containing CEPshV astrocytes and their progenitors is circled.

(F) Differential gene expression analysis comparing CEPsh astrocyte progenitors versus other progenitors. Genes enriched (red) or depleted (blue) in CEPsh astrocyte progenitors are highlighted. Transcription factors are labeled. Dorsal and ventral datasets were combined for analysis.

(G) Same as (F), but comparing CEPsh astrocytes with other terminal cell types.

(H) Workflow of the RNAi screen targeting candidate transcription factors and DNA binding proteins. Animals expressing the *hlh-17p::gfp* CEPsh astrocyte reporter were exposed to RNAi, and F1 progeny were scored for GFP expression.

(I) Summary of RNAi screen results. Columns with zero values are marked with “x”. #, phenotype not scored. Fisher’s exact test, $*p < 0.05$, $**p < 0.01$, $***p < 0.001$, $****p < 0.0001$. Raw data, n, and *p*-values are provided in Supplementary Table S2.

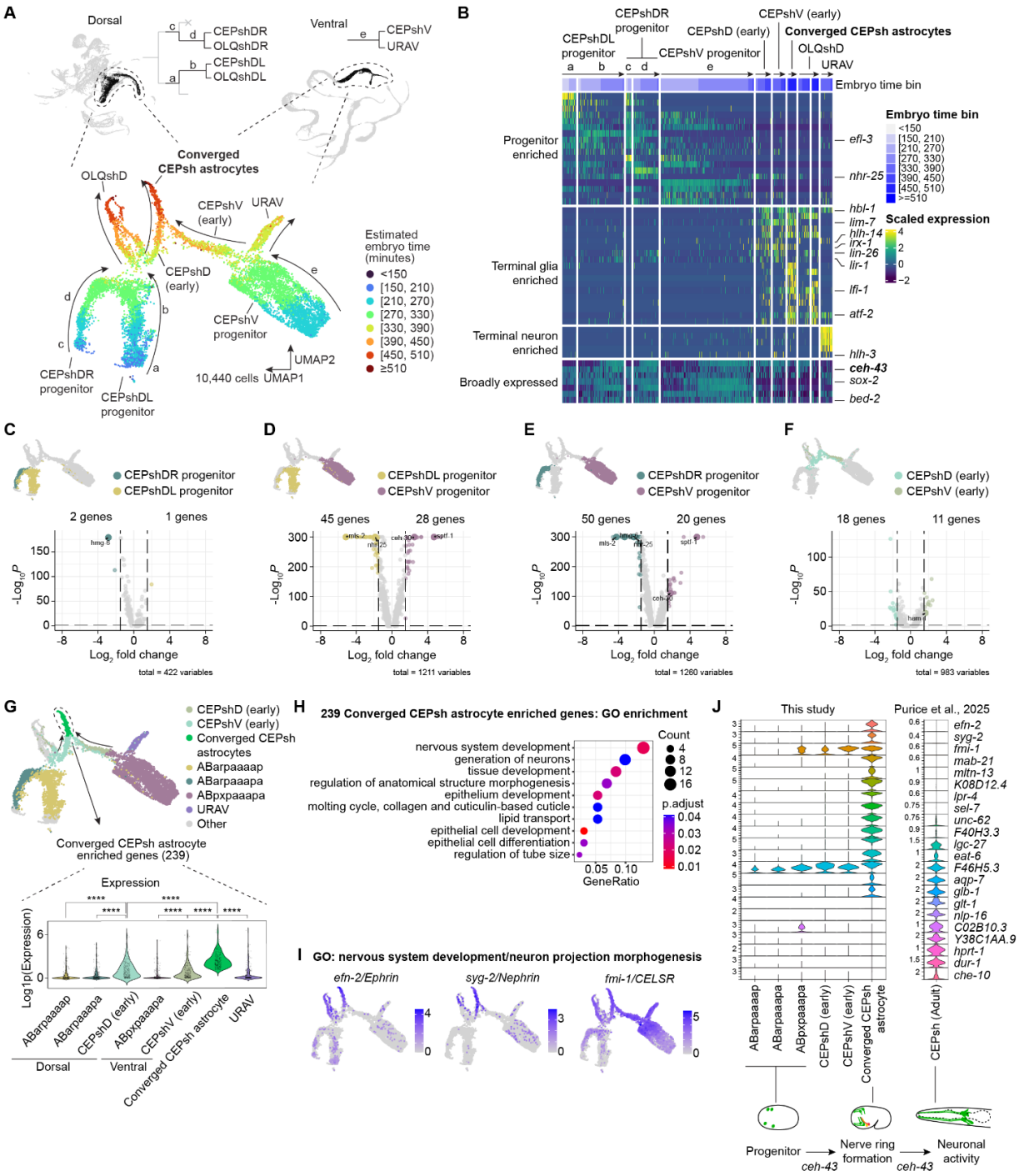

Figure 2. Nascent CEPsh astrocytes rapidly converge onto a shared transcriptional state

(A) UMAP projection of 10,440 cells from the CEPshD and CEPshV lineages. The lineage relationships are shown in the dendrogram above. Arrows indicate developmental

progression over time on the UMAP. Lower case letters (a-e) indicate cells whose transcription profiles are shown in panel (B).

(B) Heatmap showing expression patterns of transcription factor and DNA binding genes in representative CEPsh astrocytes and their progenitors at different time points. Lower case letters (a-e) correspond to panel (A). Expression values were log-transformed, centered, and scaled by the standard deviation of each gene (row).

(C-F) Differential gene expression analysis between the indicated clusters, as illustrated in the corresponding UMAP projections.

(G) Expression dynamics of converged CEPsh astrocyte enriched genes across clusters highlighted in the UMAP projection. For each cluster, the average expression level of each gene is calculated and plotted as an individual dot. ****$p < 0.0001$ by Kruskal–Wallis tests with Bonferroni correction for multiple comparisons.

(H) Significantly enriched Gene Ontology (GO) terms among genes upregulated in converged CEPsh astrocytes.

(I) Genes encoding cell membrane proteins implicated in axon guidance and outgrowth (*efn-2*, *fmi-1*) and synapse formation (*syg*-2) are expressed in converged CEPsh astrocytes.

(J) Top, violin plots showing expression dynamics of representative CEPsh astrocyte genes at different developmental stages. Adult CEPsh astrocyte transcriptomic data are from Purice et al. (2025). Bottom, schematic model of CEPsh astrocyte development. In phase I, nascent CEPsh astrocytes express genes supporting axon guidance and nerve ring assembly (red and yellow indicate pioneer and follower nerve ring neurons), reminiscent of mammalian radial glia. Upon completion of nerve ring formation, phase II

begins, activating genes that regulate neurotransmitter uptake and other aspects of neuronal activity control.

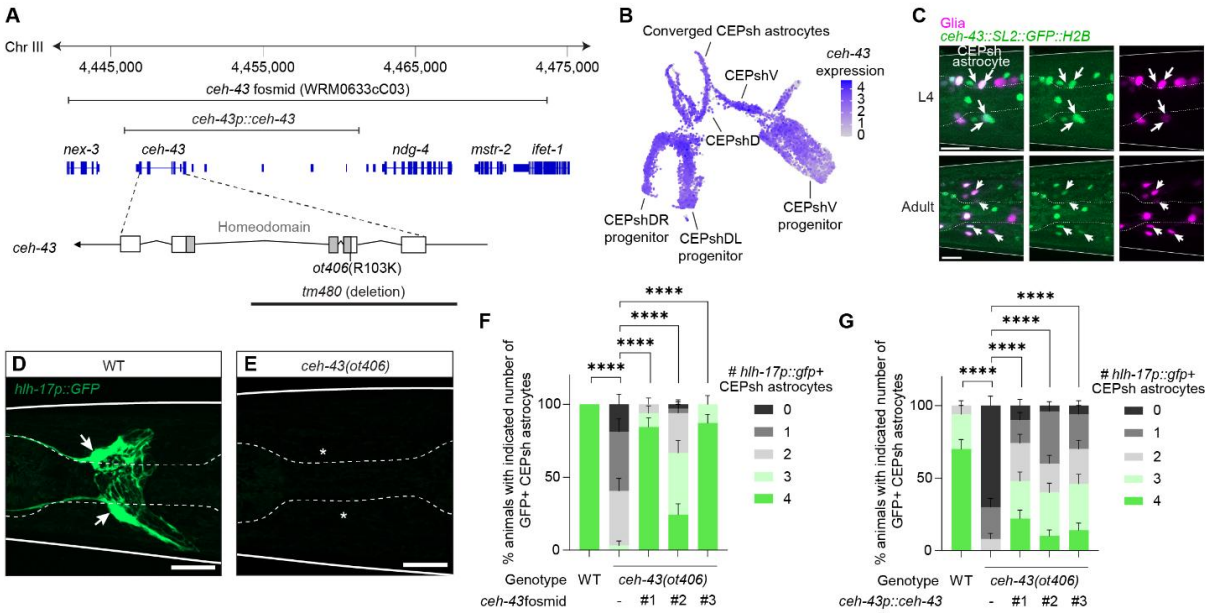

Figure 3. CEH-43 promotes CEPsh astrocyte differentiation.

(A) Schematic of the *ceh-43* locus and DNA constructs used in this study.

(B) Embryonic expression of *ceh-43* in CEPshD and CEPshV lineages.

(C) Post-embryonic *ceh-43* expression (green) in L4 larvae and young adults. Glia (magenta) are labeled with *mir-228p::2xNLS::iBlueberry*. Maximum-projection images of whole animals are shown. Arrows, CEPsh astrocyte nuclei.

(D, E) Representative confocal images of *hlh-17p::gfp* expression in CEPsh astrocytes of L4 larvae in wild-type (D) or *ceh-43(ot406)* mutant (E) animals. Arrows, CEPsh astrocytes. Asterisks indicate loss of *hlh-17p::gfp* expression in CEPsh astrocytes.

(F) A *ceh-43* fosmid transgene restores *hlh-17p::gfp* expression to CEPsh astrocytes of *ceh-43*(*ot406*) mutants. n = 31, 32, 32, 33, 31 animals per genotype from three independent scoring sessions. Three independent fosmid lines (#1, #2, #3) were analyzed. ****$p < 0.0001$ by Fisher's exact test.

(G) Same as (F) except that rescue was achieved with a PCR fragment containing only *ceh-43* coding and regulatory regions (see panel A). n = 50 animals per genotype from three independent scoring sessions.

Scale bars, 10 μm. Error bars, mean ± s.e.m.

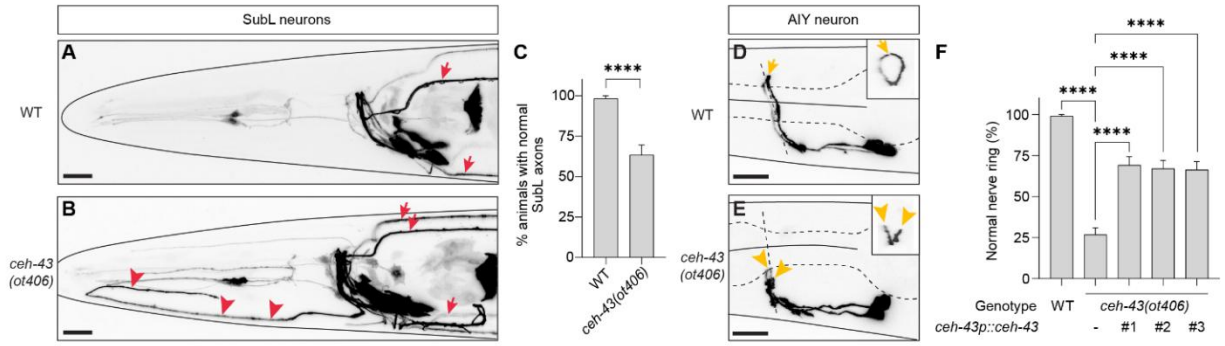

Figure 4. CEH-43 is required for nerve ring assembly

(A, B) Representative maximum-projection confocal images of sublateral (SubL) neurons labeled with *ceh-24p::gfp* in wild-type (A) and *ceh-43(ot406)* (B) L4 larvae. Arrows, normal posteriorly extending processes. Arrowheads, aberrant anterior processes.

(C) Quantification of SubL axon guidance defects. n = 60 animals per genotype from three independent imaging sessions. ****$p < 0.0001$ by Fisher's exact test.

(D, E) Representative maximum-projection confocal images of AIY interneurons labeled with *ttx-3p::gfp* in wild-type (A) and *ceh-43(ot406)* (B) L4 larvae. Arrows, the dorsal apex of left and right AIY axon trajectories. Arrowheads, abnormal AIY axons.

(F) Quantification of AIY axon defects. n = 100, 112, 81, 88, and 86 animals per genotype from three independent imaging sessions. Three independent transgenic lines were analyzed (#1, #2, #3). ****$p < 0.0001$ by Fisher's exact test.

Scale bar, 10 μm. Error bars, mean ± s.e.m.

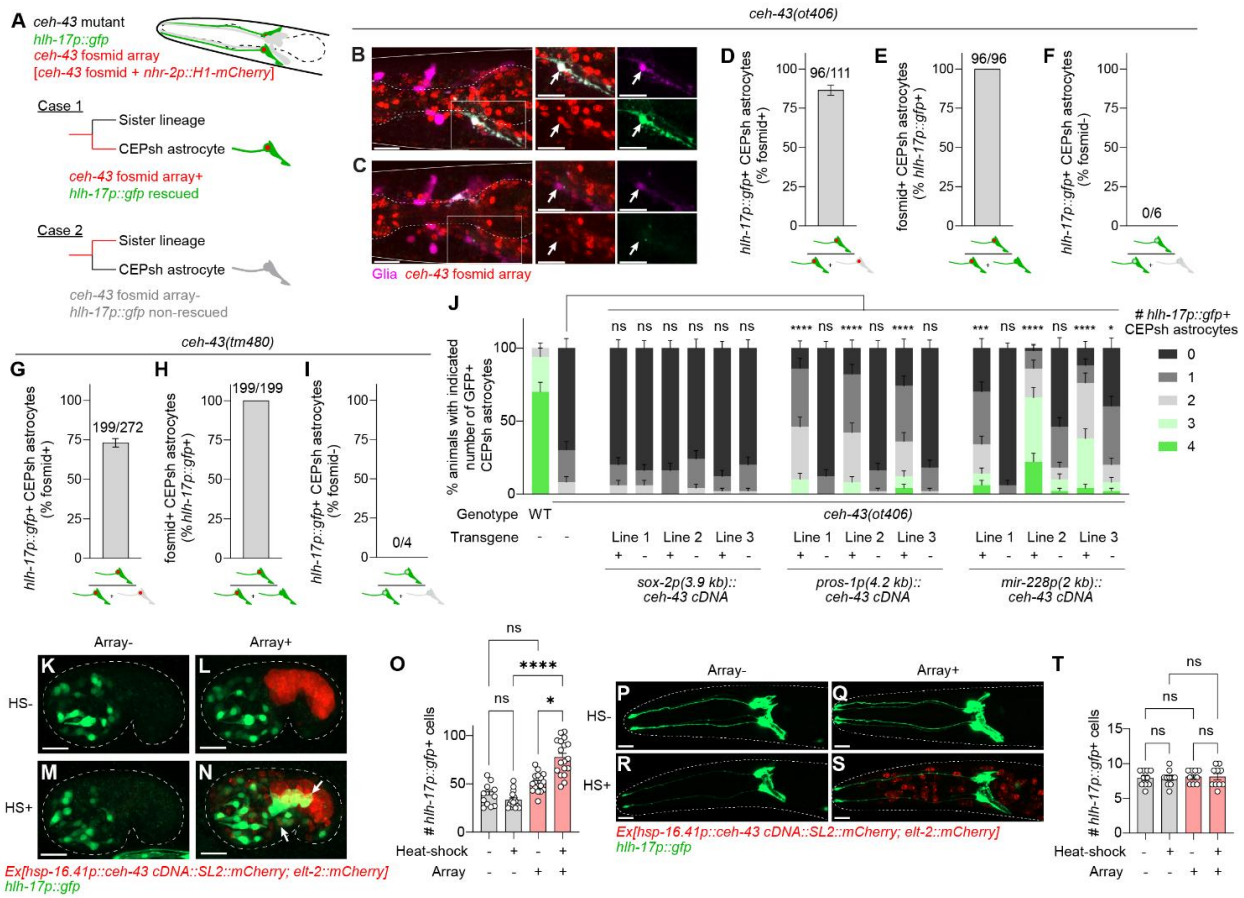

Figure 5. CEH-43 functions cell autonomously in early CEPsh astrocytes and is sufficient to induce embryonic CEPsh astrocyte gene expression

(A) General strategy for mosaic analysis. An unstable extrachromosomal array containing wild-type *ceh-43* genomic sequences (fosmid) and a pan-cellular nuclear reporter transgene (*nhr-2p::H1-mCherry*) was introduced into *ceh-43(ot406)* or *ceh-43(tm480)* mutants and assessed for co-expression with the *ceh-43* target reporter *hlh-17p::gfp*. If *ceh-43* acts cell autonomously, mCherry presence in a CEPsh astrocyte should correlate with GFP presence in that same cell (Case 1), and conversely, the absence of mCherry should correlate with the absence of GFP (Case 2).

(B) Presence of *ceh-43* fosmid, visualized by *nhr-2p::H1-mCherry* (red), overlaps with *hlh-17::gfp* expression (green). Glia are marked with *mir-228p::2xNLS::iBlueberry* (magenta).

Insets show enlarged views of the boxed regions on the left. Arrow indicates CEPsh astrocytes.

(C) Same as (B) except that *nhr-2p::H1-mCherry* (red) is absent from the indicated CEPsh astrocyte (arrow), and *hlh-17::gfp* expression (green) is not induced in this cell.

(D-F) Quantification of mosaic analysis in *ceh-43(ot406)* mutants.

(D) Overall efficiency of *ceh-43* fosmid-mediated restoration of *hlh-17::gfp* expression.

(E) All CEPsh astrocytes expressing *hlh-17::gfp* carry the *ceh-43* fosmid.

(F) No CEPsh astrocytes lacking the *ceh-43* fosmid express *hlh-17p::gfp*.

Numbers above bars indicate CEPsh astrocytes analyzed across three imaging sessions (30 L4 larvae total).

(G-I) Same as (D-F), but for *ceh-43(tm480)* mutants. A total of 70 L4 larvae were examined.

(J) Quantification of rescue efficiency for the indicated transgenes in *ceh-43(ot406)* mutants. n = 50 animals per genotype from >3 independent scoring sessions. *$p < 0.05$, ***$p < 0.001$, ****$p < 0.0001$ by Fisher's exact test.

(K–O) Ectopic CEH-43 expression induces ectopic *hlh-17p::gfp* expression in comma-stage embryos.

(K-N) Maximum projections of confocal z-stacks. Without heat shock (K, M), no ectopic expression is observed in embryos lacking (Array-) the *hsp-16.41p::ceh-43 cDNA::SL2 mCherry* construct (coinjected with *elt-2::mCherry*, red). HS- Array+ embryos (L) display mild ectopic *hlh-17p::gfp* expression, likely due to promoter leakiness, while HS+ Array+ (N) embryos exhibit stronger ectopic expression.

(O) Quantification of the heat-shock experiment. n = 15, 13, 18, and 17 embryos from 2–3 imaging sessions. *$p < 0.05$; ****$p < 0.0001$; ns, not significant by Kruskal-Wallis test with Dunn's multiple comparisons correction.

(P-T) Same as (K-O), except performed in L4 larvae. (T) n = 10 animals from two imaging sessions.

Scale bars, 10 μm. Error bars, mean ± s.e.m.

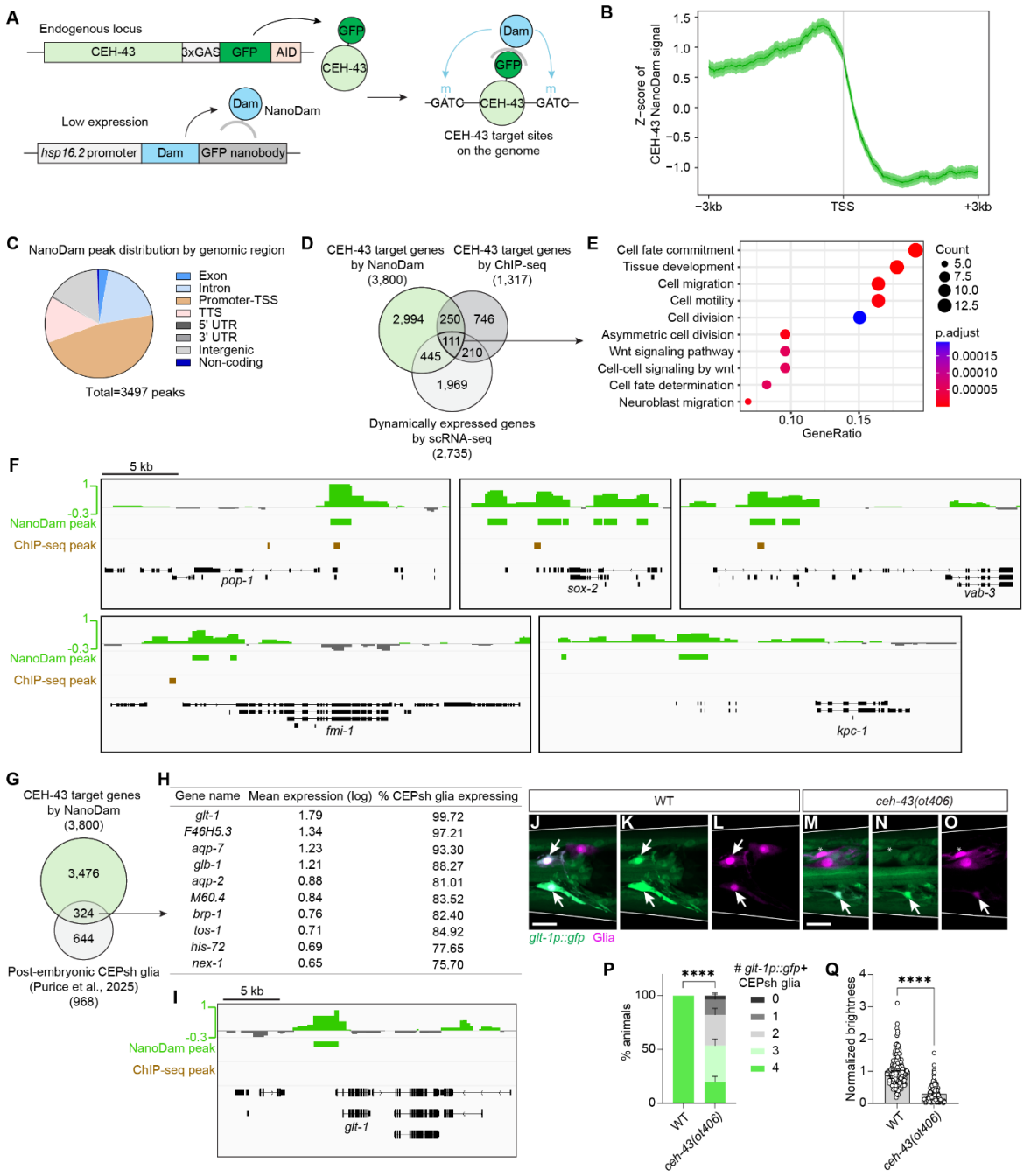

Figure 6. CEH-43 binds genes regulating CEPsh astrocyte development and function

(A) Schematic of the CEH-43 NanoDam strategy. A leaky *hsp-16.2* promoter drives low-level expression of a GFP nanobody-Dam methylase fusion protein (NanoDam) in all cells

in the absence of heat shock. Endogenous CEH-43 protein is C-terminally tagged with GFP. The GFP nanobody binds GFP-tagged CEH-43, recruiting Dam methylase to CEH-43 DNA binding sites, leading to methylation of nearby GATC sequences.

(B) Aggregation plot of CEH-43 NanoDam signal (Z-score) centered on transcription start sites (TSS) across all detected peaks, showing enrichment upstream of TSS.

(C) Genomic distribution of 3,497 NanoDam peaks, revealing enrichment in non-coding regions. Peaks were called at a false discovery rate (FDR) $<10^{-25}$. TTS, transcription termination site.

(D) Venn diagram showing overlap between CEH-43 target genes identified by NanoDam, ChIP-seq (Kudron et al., 2024), and dynamically expressed genes from the CEPsh astrocyte scRNA-seq studies (**Figure 1**).

(E) Gene Ontology (GO) enrichment analysis of 111 high-confidence embryonic CEH-43 target genes.

(F) Representative CEH-43-targeted genes. NanoDam binding intensities are shown as $\log_2$-fold enrichment of CEH-43 NanoDam over NanoDam-alone controls. Identified binding peaks are marked in green. ChIP-seq peaks from Kudron et al. (2024) are shown in brown. Gene names and exon-intron structures shown below.

(G) Overlap between CEH-43 NanoDam target genes and genes expressed in post-embryonic CEPsh astrocytes (Purice et al., 2025).

(H) Top 10 CEH-43 NanoDam target genes ranked by expression level in post-embryonic CEPsh astrocytes (Purice et al., 2025).

(I) NanoDam binding profile upstream of *glt-1* coding sequences.

(J–O) CEH-43 is required for *glt-1* expression. Maximum-projection confocal images of representative wild-type (J–L) and *ceh-43(ot406)* (M–O) L4 larvae. (J, M) Merged channels; (K, N) *glt-1p::gfp* expression; (L, O) *mir-228p::2xNLS::iBlueberry* pan-glial marker labeling CEPsh astrocytes. Arrows, *glt-1p::gfp*-positive CEPsh astrocytes. Asterisks, CEPsh astrocytes lacking *glt-1p::gfp* expression.

(P) Quantification showing that the number of *glt-1p::gfp*-positive CEPsh astrocytes is significantly reduced in *ceh-43(ot406)* mutants compared to wild type. ****$p < 0.0001$ by Fisher's exact test.

(Q) Quantification of *glt-1p::gfp* expression levels in CEPsh astrocytes, which is significantly reduced in *ceh-43(ot406)* mutants compared to wild type. ****$p < 0.0001$ by Welch's t-test.

Scale bar, 10 μm. Error bars, mean ± s.e.m.

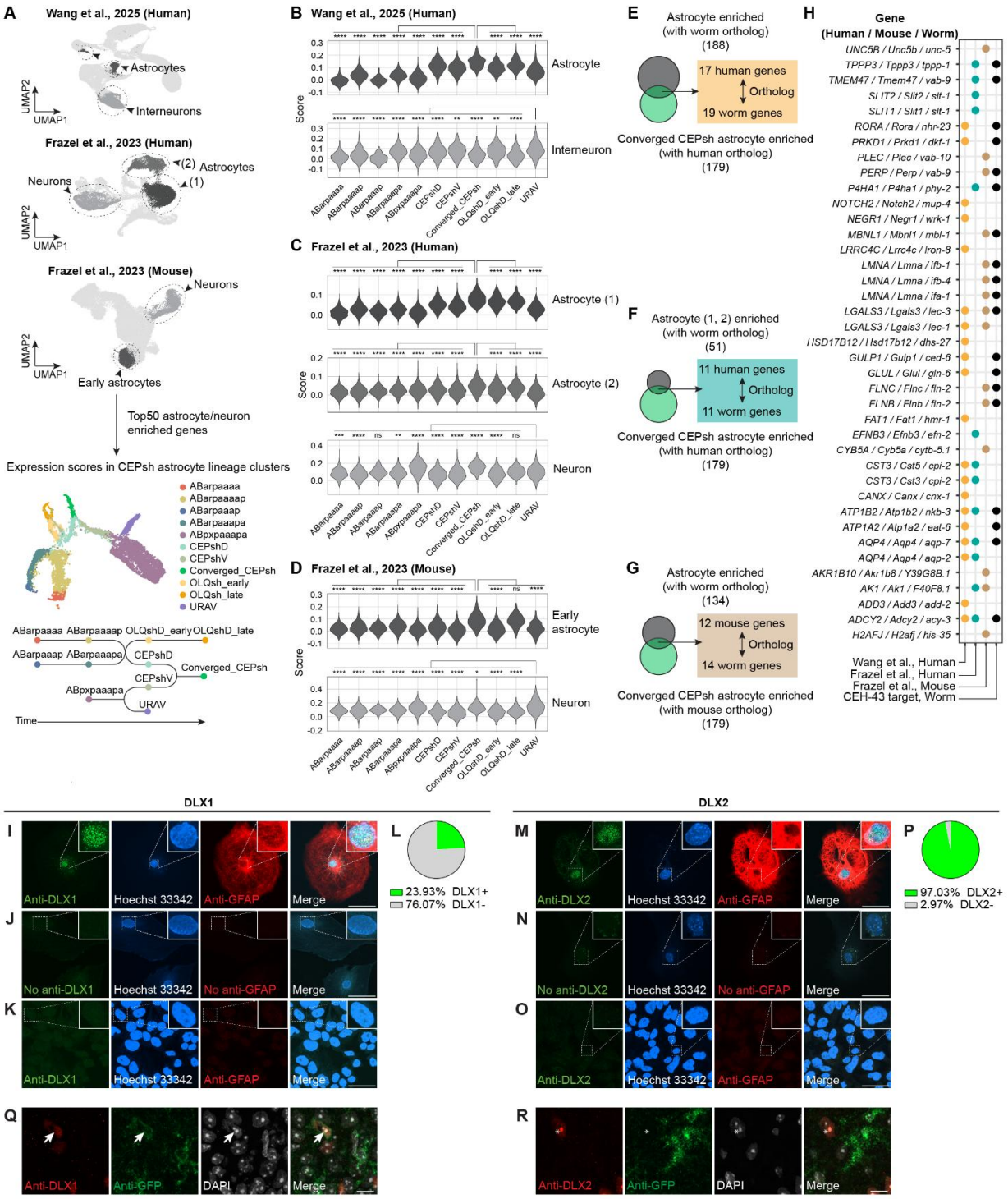

Figure 7. Conserved transcriptional and molecular features of *C. elegans* and mammalian astrocytes

(A) Top: UMAP projections of three published single-cell RNA-seq datasets (Wang et al., 2025; Frazel et al., 2023, human; Frazel et al., 2023, mouse) highlighting astrocyte and neuron populations. Bottom, UMAP projection of cell types within the *C. elegans* CEPsh astrocyte lineage, with a schematic of the lineage relationship.

(B-D) Module scores of astrocyte- and neuron-enriched genes from the Wang et al. (2025) dataset (B), the Frazel et al. (2023) human dataset (C), and the Frazel et al. (2023) mouse dataset (D) plotted across *C. elegans* CEPsh lineage cells. Statistical significance was determined by Wilcoxon test with Bonferroni correction. *$p < 0.05$; **$p < 0.01$; ****$p < 0.0001$, ns, not significant.

(E-G) Orthologous gene pairs enriched in both CEPsh astrocytes and mammalian astrocytes (average $\log_2$FC >0.5, adjusted *p*-value <0.05): (E) Wang et al. (2025); (F) Frazel et al. (2023, human); (G) Frazel et al. (2023, mouse).

(H) Genes enriched in both CEPsh astrocytes and mammalian astrocytes. Dot plot showing the presence of each gene in human and mouse astrocyte datasets and whether the corresponding *C. elegans* ortholog is a CEH-43 NanoDam target.

(I) Immunofluorescence staining of primary astrocytes showing DLX1, GFAP, and Hoechst 33342 nuclear counterstain. Representative Z-stack images are shown. Scale bar, 50μm.

(J) Same as (I) but without primary antibodies.

(K) Same as (I) but staining undifferentiated P19 cells as a negative control.

(L) Quantification of the proportion of DLX1+ astrocytes.

(M) Immunofluorescence staining of primary astrocytes showing DLX2, GFAP, and Hoechst 33342. Representative Z-stack images are shown. Scale bar, 50μm.

(N) Same as (M) but without primary antibodies.

(O) Same as (M) but staining undifferentiated P19 cells as a negative control.

(P) Quantification of the proportion of DLX2+ astrocytes.

(Q) Immunofluorescence staining of adult JD130 (*Aldh1l1-EGFP/Rpl10a*) mouse brain slice showing a DLX1+ astrocyte (arrow) in the retrosplenial cortex. Representative Z-stack images are shown. Scale bar, 10μm.

(R) Same as (Q) but showing a DLX2+ non-astrocyte (asterisk).

SUPPLEMENTAL FIGURE TITLES AND LEGENDS

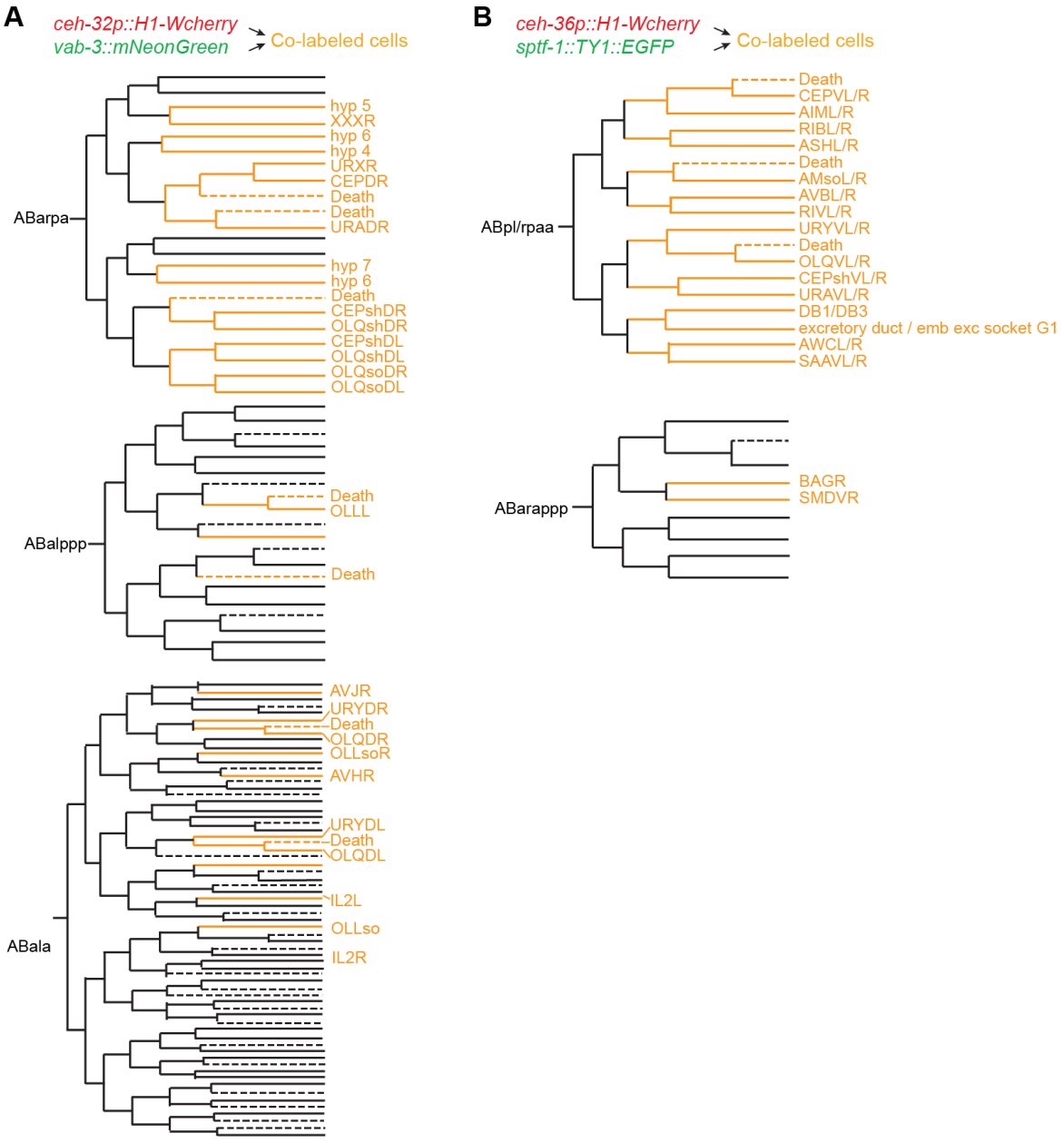

Figure S1. Predicted expression patterns of fluorescent reporter combinations labeling dorsal and ventral CEPsh astrocyte lineages

(A,B) Predicted co-labeled cell types based on previously published reporter expression data[60,118] for the dorsal (A) and ventral (B) datasets.

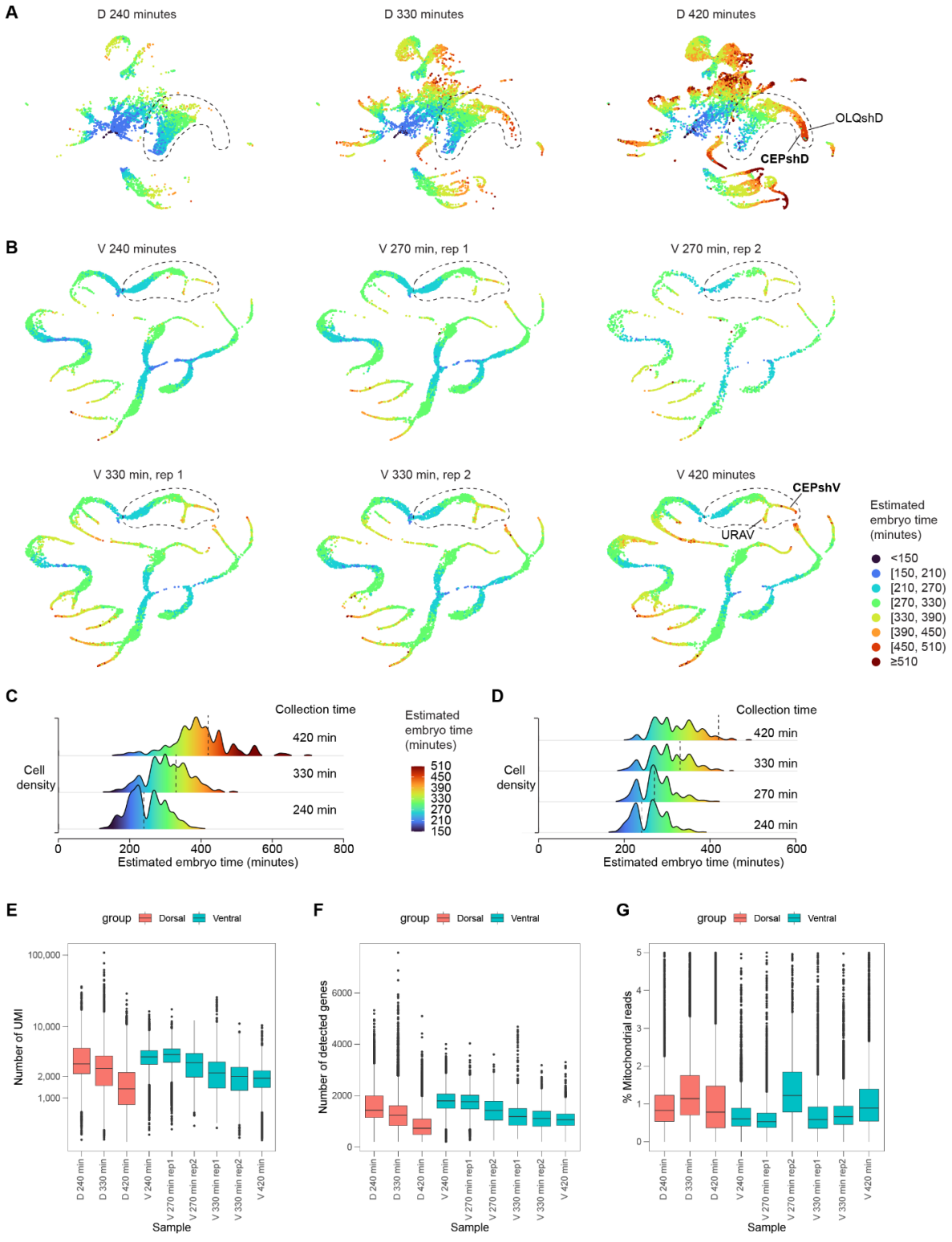

Figure S2. scRNA-seq quality control and developmental timing distribution

(A, B) UMAP projections of cells from dorsal (A) or ventral (B) samples at the indicated time points post-fertilization. Colors indicate estimated embryo time. The sub-lineage containing CEPsh astrocytes, along with their direct sister and progenitor cells, is circled.

(C, D) Ridge plots of estimated embryo time distributions for cells in the dorsal (C) and ventral (D) datasets, based on comparisons to bulk embryo development data set[55]. Dashed vertical lines, target sample collection times. For the ventral dataset, embryo collections at 270 and 330 minutes were performed in two independent replicates.

(E–G) Quality control metrics for scRNA-seq samples: (E) number of UMIs per cell, (F) number of detected genes per cell, and (G) percent mitochondrial reads per cell.

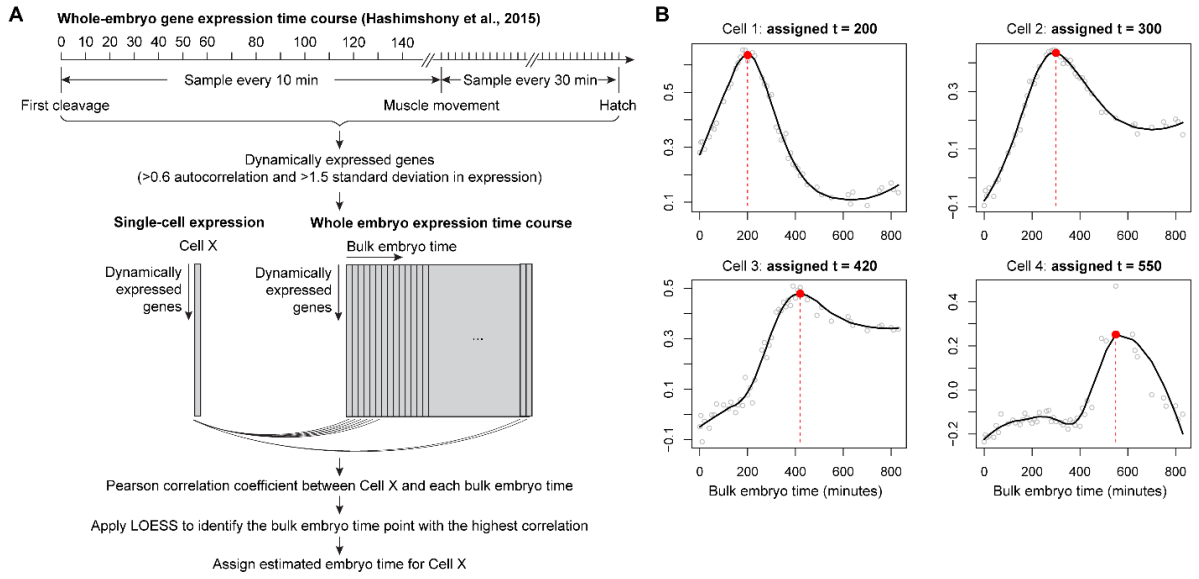

Figure S3. Embryo time estimation

(A) Workflow of embryo time estimation. Dynamically expressed genes were identified from a whole-embryo time course[55]. For each single cell, expression levels of these genes were correlated with bulk embryo time points using Pearson correlation. After LOESS smoothing, the time point with the highest correlation was assigned as the cell's estimated embryo time.

(B) Example embryo time estimation for four single cells. Open circles, Pearson correlation coefficient. Black curve, best fit with LOESS smoothing. Red circle, curve maximum.

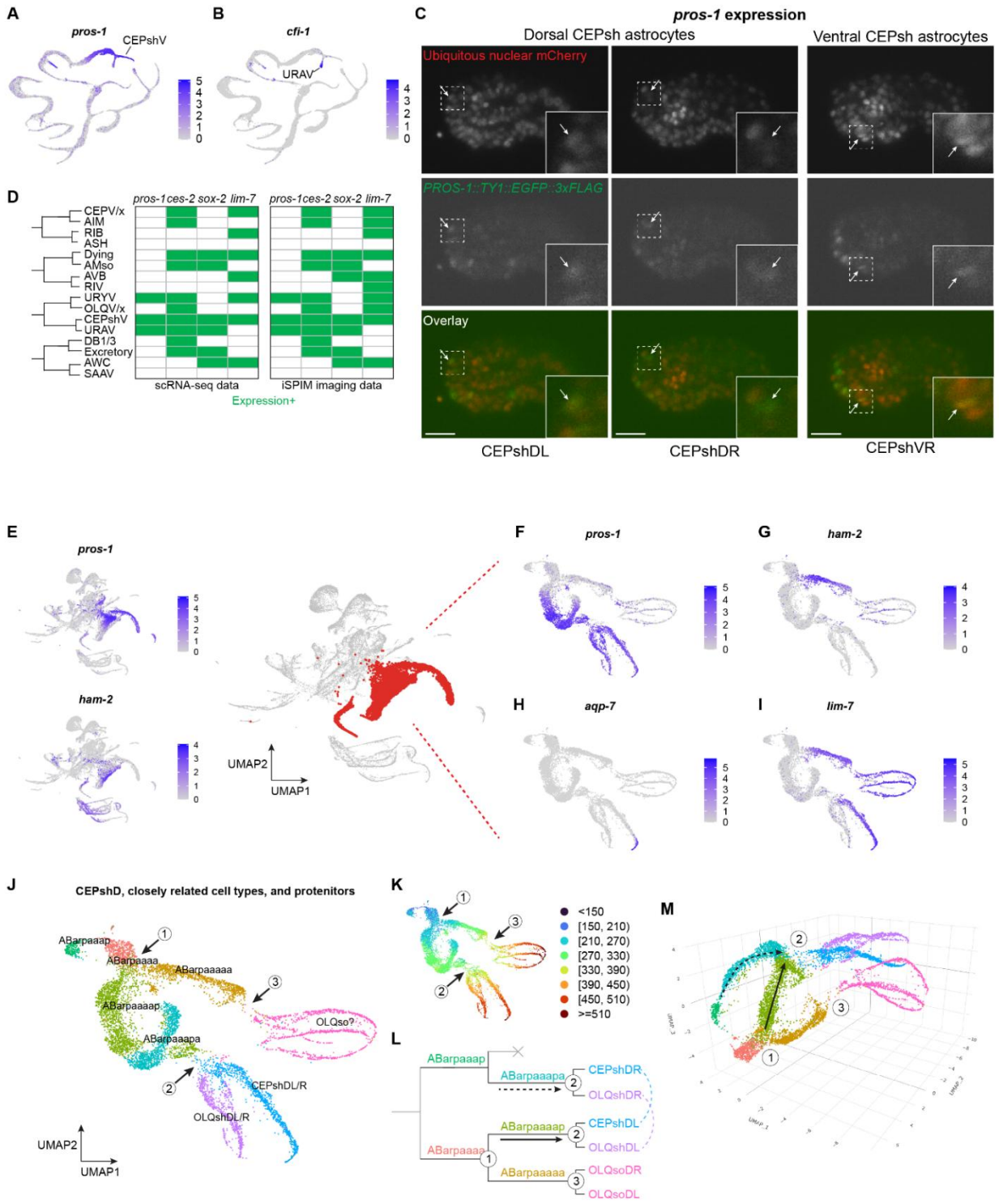

Figure S4. Identification of CEPsh astrocyte lineages and validation of marker gene expression

(A, B) Expression patterns of *pros-1* (A), a CEPshV marker, and *cfi-1* (B), a URAV marker.

(C) iSPIM imaging with lineage tracking showing *PROS-1::TY1::EGFP::3xFLAG* expression in dorsal and ventral CEPsh astrocytes. Insets show enlarged view of the dash line-boxed region highlighting dorsal (CEPshDL, CEPshDR) and ventral (CEPshVR) CEPsh astrocytes (arrows). Scale bar, 10 μm.

(D) iSPIM imaging validating marker gene expression in lineages related to ventral CEPsh astrocytes. n = 1, 2, 1, 3 embryos for iSPIM imaging data.

(E) Expression patterns of *pros-1* and *ham-2* in the dorsal dataset, identifying CEPshD astrocyte lineages.

(F-I) Expression patterns of *pros-1* (F), *ham-2* (G), *aqp-7* (H), *lim-7* (I) in CEPshD astrocyte lineages.

(J, K) UMAP projections showing cell type annotations (J) and estimated embryo times (K) in CEPshD astrocyte lineages. Cell division events are indicated by numbers (see also L and M). The OLQso clusters may represent OLQso cells as well as another socket glial type (CEPso/ILso), which cannot be definitely verified from available gene expression data.

(L) Lineage diagram of CEPshD astrocyte lineages. Solid and dash arrows indicate two converging CEPsh progenitor lineages (see also panel M).

(M) 3D UMAP projection of CEPshD astrocyte lineages. The two CEPshD progenitor lineages (solid and dash lines, respectively) converge and give rise to a shared CEPshD astrocyte cluster.

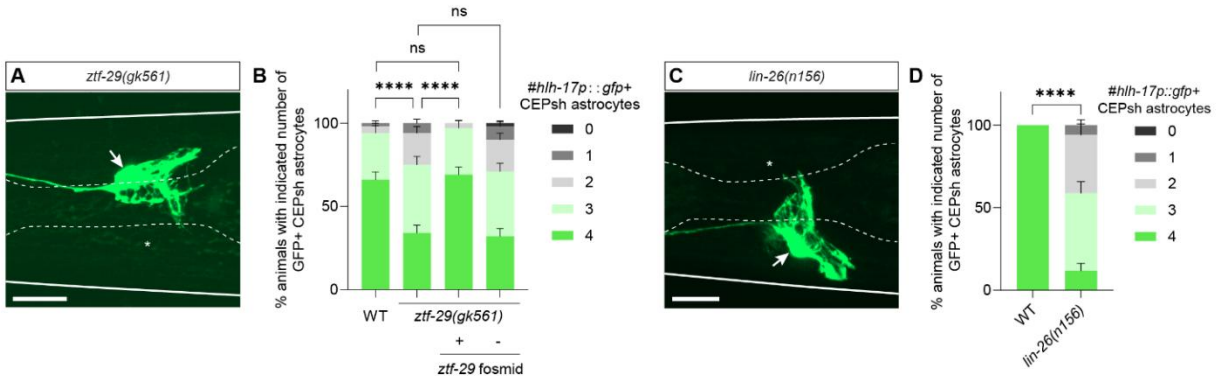

Figure S5. Loss of CEPsh astrocyte reporter expression in *lin-26* and *ztf-29* mutants

(A) Representative confocal image of *hlh-17p::gfp* expression in a *ztf-29(gk561)* mutant L4 larva. Arrows, a CEPsh astrocyte. Asterisks, loss of *hlh-17p::gfp* expression in CEPsh astrocytes.

(B) Quantification of *hlh-17p::gfp* expression in *ztf-29(gk561)* mutants and rescue lines carrying a *ztf-29* fosmid. n = 100 animals per genotype from three independent scoring sessions. ****$p < 0.0001$ by Fisher's exact test.

(C) Same as (A) but in *lin-26(n156)* mutants.

(D) Same as (B) but for *lin-26(n156)* mutants.

Scale bars, 10 μm. Error bars, mean ± s.e.m.

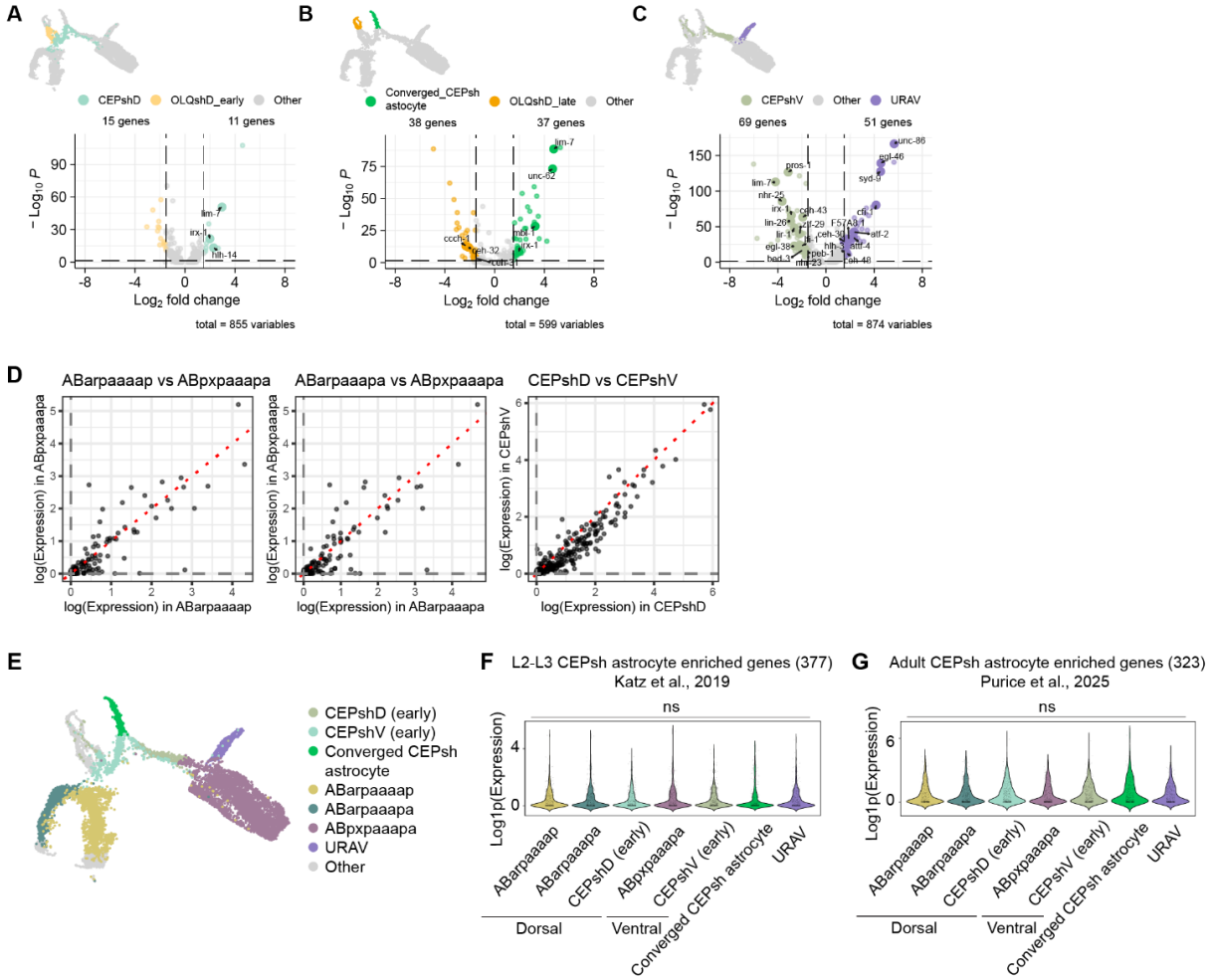

Figure S6. Differential gene expression, converged CEPsh astrocyte-enriched gene expression dynamics, and expression of post-embryonic CEPsh astrocyte-enriched genes in embryonic CEPsh astrocyte lineages

(A–C) Differential gene expression analyses showing divergence of CEPsh astrocyte gene expression from their sister cell types. Transcription factors are highlighted. See Figure 2C-F legend for details.

(D) Scatter plots comparing log-transformed average expression of converged CEPsh astrocyte- or progenitor-enriched genes between dorsal and ventral clusters. Note the

strong correlation between dorsal and ventral CEPsh astrocytes. Red dashed lines, line of equal expression.

(E) UMAP projection showing cell type clusters from CEPshD and CEPshV lineages analyzed in (F) and (G).

(F) Violin plots showing expression of 377 CEPsh-enriched genes identified in L2–L3 larval astrocytes[48] across CEPshD and CEPshV lineage clusters. Each dot represents the average expression of one gene. ns, not significant using Kruskal–Wallis test with Bonferroni correction. Note the very low or absent expression, suggesting that embryonic and larval CEPsh glia are transcriptionally distinct.

(G) Same as (F) but for adult CEPsh astrocytes[79].

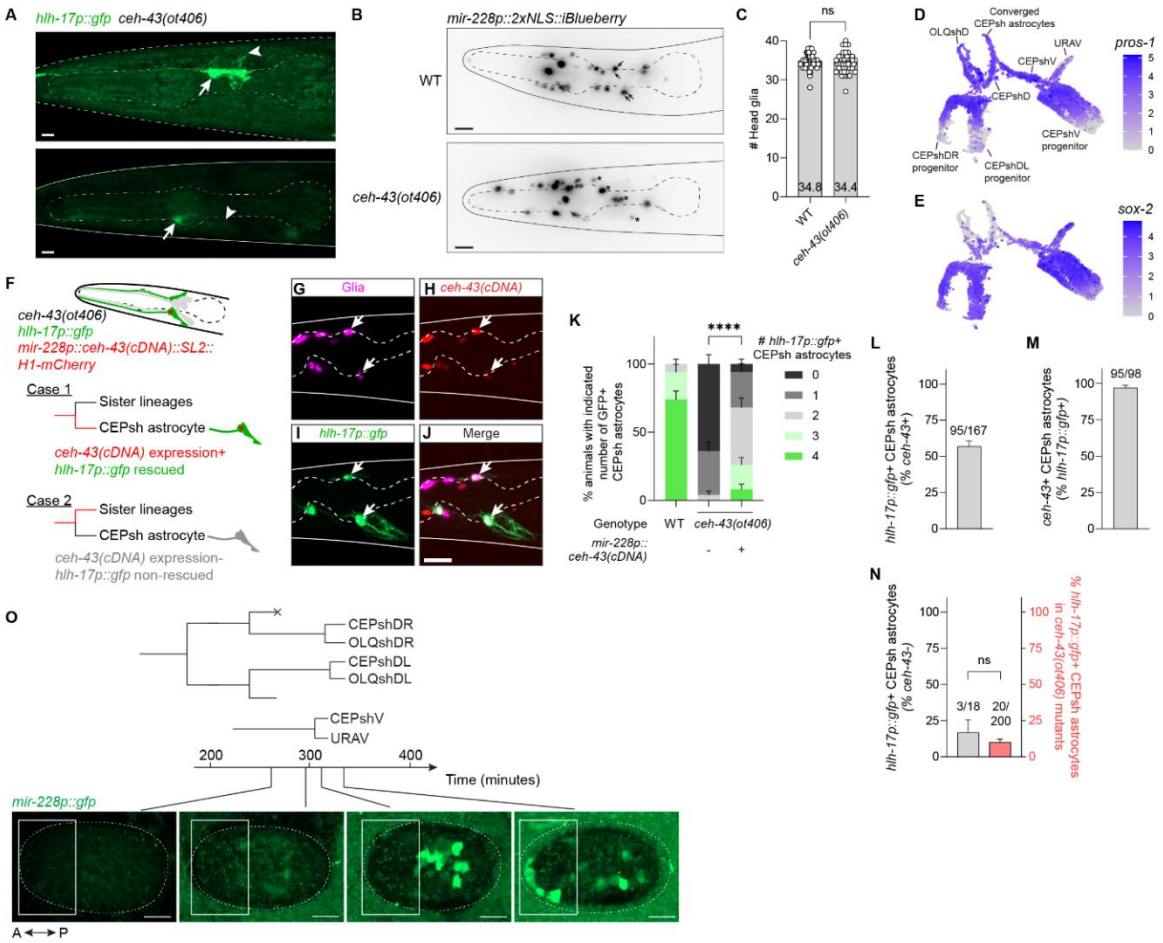

Figure S7. CEH-43 functions cell-autonomously to regulate *hlh-17p::gfp* expression in CEPsh astrocytes

(A) Remaining *hlh-17p::gfp*-positive CEPsh astrocytes in two *ceh-43(ot406)* mutant animals. Arrows, CEPsh astrocytes somata. Arrowheads, CEPsh astrocytes posterior processes.

(B) Representative maximum-projection confocal images of L4 wild-type and *ceh-43(ot406)* mutant larvae carrying the pan-glial marker *mir-228p::2xNLS::iBlueberry*. Arrows, CEPsh astrocytes in the wild-type larva. Asterisks, putative CEPsh astrocytes in the mutant larva; because CEPsh cell bodies are displaced in the mutant, their identification is uncertain.

(C) Quantification of total head glia number, which is unchanged in *ceh-43(ot406)* mutants compared with wild type. Numbers within columns, average head glia counts (n = 50 for wild-type and 41 for mutant L4 larvae from three imaging sessions). ns, not significant by Mann–Whitney test.

(D, E) Embryonic expression of *pros-1* (D) and *sox-2* (E) in CEPsh astrocytes and their progenitors.

(F) Mosaic analysis strategy, using the *mir-228p::ceh-43(cDNA)::SL2::H1-mCherry* rescue construct, which drives pan-glial expression of *ceh-43(cDNA)*.

(G–J) Maximum-projection confocal image showing CEPsh astrocytes of *ceh-43(ot406)* mutant animals, rescued using a *mir-228p::ceh-43(cDNA)::SL2::H1-mCherry* transgene. Glia are marked with *mir-228p::2xNLS::iBlueberry* (magenta). Arrows, CEPsh astrocytes.

(K) Pan-glial *ceh-43(cDNA)* expression rescues *hlh-17p::gfp* expression in CEPsh astrocytes. n = 50 animals per group from 2-5 independent scoring sessions. ****$p < 0.0001$ by Fisher's exact test.

(L) Rescue efficiency of *mir-228p::ceh-43(cDNA)* in CEPsh astrocytes.

(M) Nearly all CEPsh astrocytes expressing *hlh-17p::gfp* also carry the *mir-228p::ceh-43(cDNA)::SL2::H1-mCherry* rescuing transgene.

(N) Among CEPsh astrocytes lacking *ceh-43* rescue array expression, only 3 of 18 express *hlh-17p::gfp*, not significantly different from non-transgenic *ceh-43(ot406)* mutants. ns, not significant using Fisher's exact test.

(O) Expression of the pan-glial reporter *mir-228p::gfp* in developing embryos. Boxed regions highlight the anterior region containing CEPsh progenitors and differentiated

CEPsh astrocytes. *mir-228p::gfp* expression is absent in the anterior region during CEPsh progenitor stages and becomes detectable only after the generation of CEPsh astrocytes. Scale bar, 10 μm. Error bars, mean ± s.e.m.

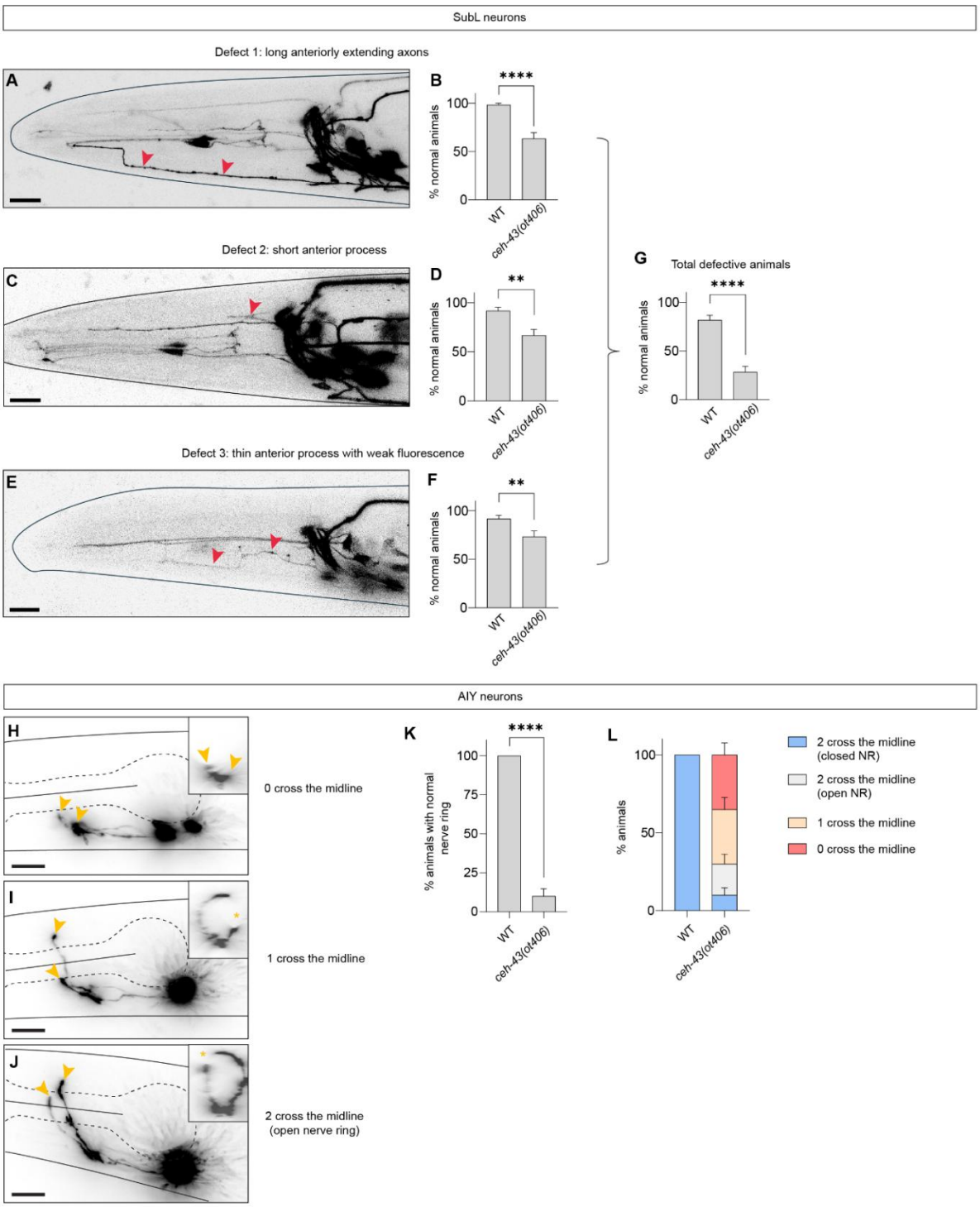

Figure S8. SubL and AIY neuron defects in *ceh-43(ot406)* mutants

(A, C, E) Representative maximum-projection confocal images of *ceh-43(ot406)* mutant animals showing distinct sublateral (SubL) neuron defects (see wild type in Figure 4A).

(B, D, F, G) Quantification of SubL neuron defects. n = 60 animals per genotype from three independent imaging sessions. All quantifications were performed on the same cohort of 60 wild-type and 60 *ceh-43(ot406)* mutant animals. $^{**}p < 0.01$, $^{****}p < 0.0001$ by Fisher's exact test.

(H–J) Representative maximum-projection confocal images illustrating the three categories of AIY axon extension defects (see wild type in Figure 4D). Arrowheads, short AIY axons; asterisks, openings in the AIY axon ring.

(K, L) Quantification of overall AIY axon extension defects. n = 40 animals per genotype from three imaging sessions. $^{****}p < 0.0001$ by Fisher's exact test.

Scale bar, 10 μm. Error bars, mean ± s.e.m.

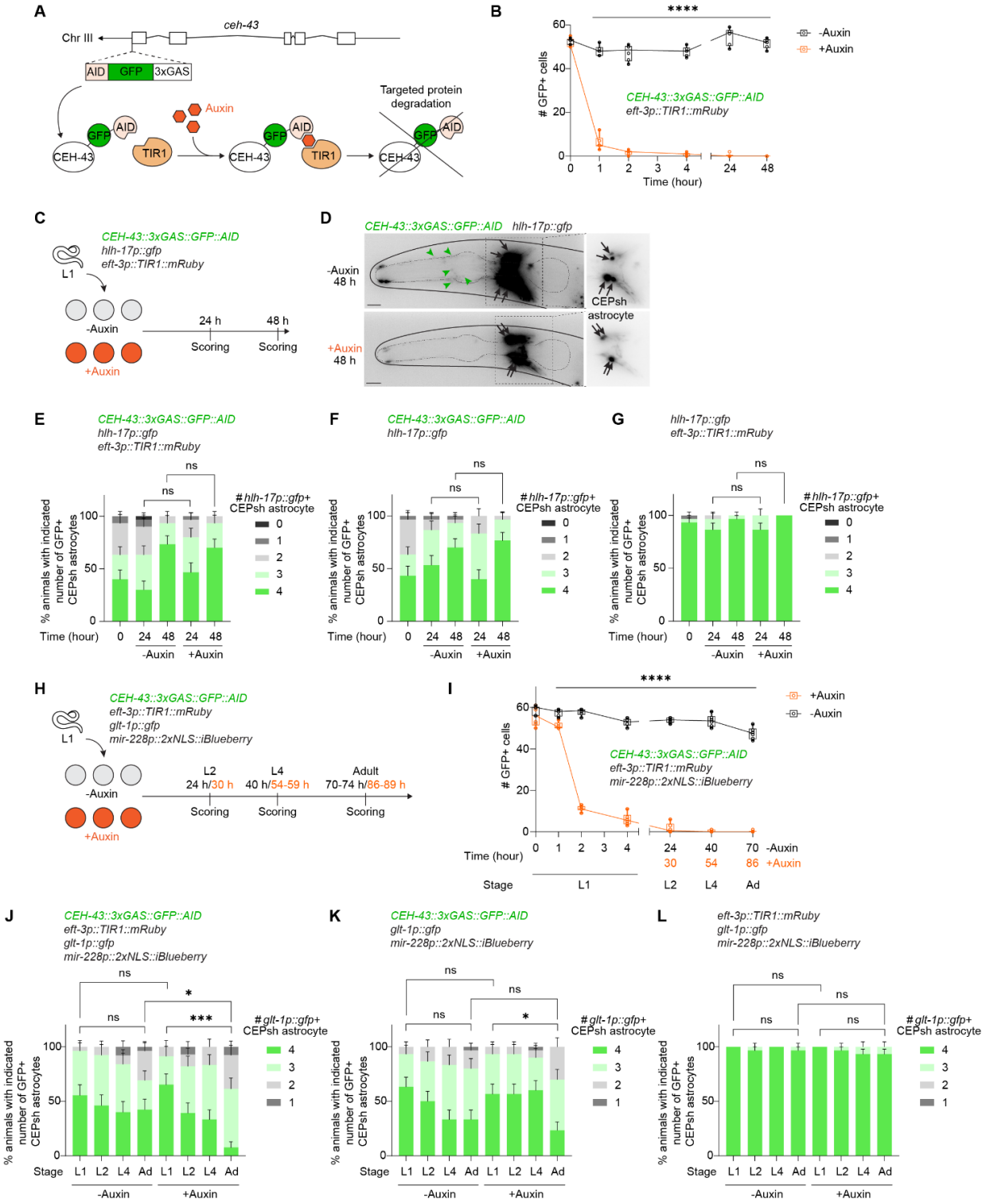

Figure S9. CEH-43 is not required to maintain post-embryonic *hlh-17p::gfp* or *glt-1p::gfp* expression

(A) Strategy for auxin-inducible CEH-43 protein degradation.

(B) Time course of CEH-43 protein degradation. n = 6 animals per time point and condition from two duplicate plates in one experiment. Adjusted *p*-values were calculated by Šidák's multiple comparisons test following two-way ANOVA. ****$p < 0.0001$.

(C) Workflow for testing *hlh-17p::gfp* expression following post-embryonic CEH-43 degradation.

(D) Representative images of animals grown without (-Auxin) or with (+Auxin) 4 mM Auxin for 48 hours. Boxed areas are enlarged with adjusted contrast to visualize CEPsh astrocytes. Green arrowheads, nuclear CEH-43::GFP signal, which disappears after auxin treatment; black arrows, *hlh-17p::gfp*-positive CEPsh astrocytes. Scale bar, 10 μm.

(E-G) Quantification of *hlh-17p::gfp*-positive CEPsh astrocytes upon auxin treatment in TIR1 + AID (E), TIR-only (F), and AID-only (G) strains. n = 30 animals from three duplicate plates in one experiment. ns, not significant by Fisher's exact test.

(H) Workflow for testing *glt-1p::gfp* expression following post-embryonic CEH-43 degradation.

(I) Time course of CEH-43 protein degradation, as in (B). n = 6 animals per time point and condition from two duplicate plates in one experiment. Adjusted *p*-values were calculated by Šidák's multiple comparisons test following two-way ANOVA. ****$p < 0.0001$.

(J-L) Quantification of the number of *glt-1p::gfp*-positive CEPsh astrocytes after auxin treatment in TIR1 + AID (J), TIR-only (K), and AID-only (L) strains. All results are from three duplicate plates in one experiment. Fisher's exact test, *$p < 0.05$, ***$p < 0.001$, ns, not significant.

(J) n = 27, 26, 25, 26, 23, 28, 24, 26 animals.

(K) n = 30 animals per group.

(L) n = 27, 30, 30, 30, 26, 30, 30, 30 animals.

Scale bar, 10 μm. Error bars, mean ± s.e.m.

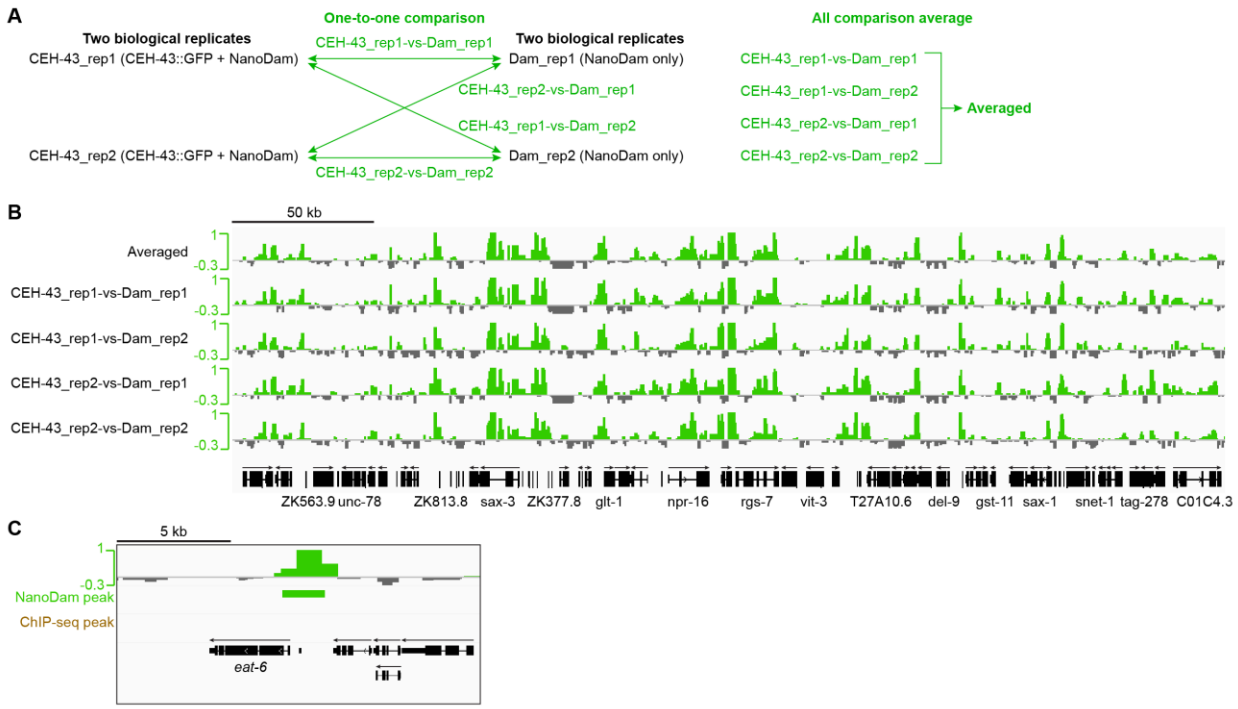

Figure S10. Comparison of CEH-43 NanoDam biological replicates

(A) Design of one-to-one comparisons between duplicates of CEH-43 NanoDam samples and duplicates of NanoDam-only controls. An averaged signal track was generated by combining all one-to-one comparisons.

(B) Peak tracks from all one-to-one comparisons and the averaged track show strong concordance. A representative genomic region from chromosome X is shown.

(C) CEH-43 NanoDam binding intensities upstream of *eat-6* coding sequences.

Arrows in (B, C) indicate the direction of coding sequences.

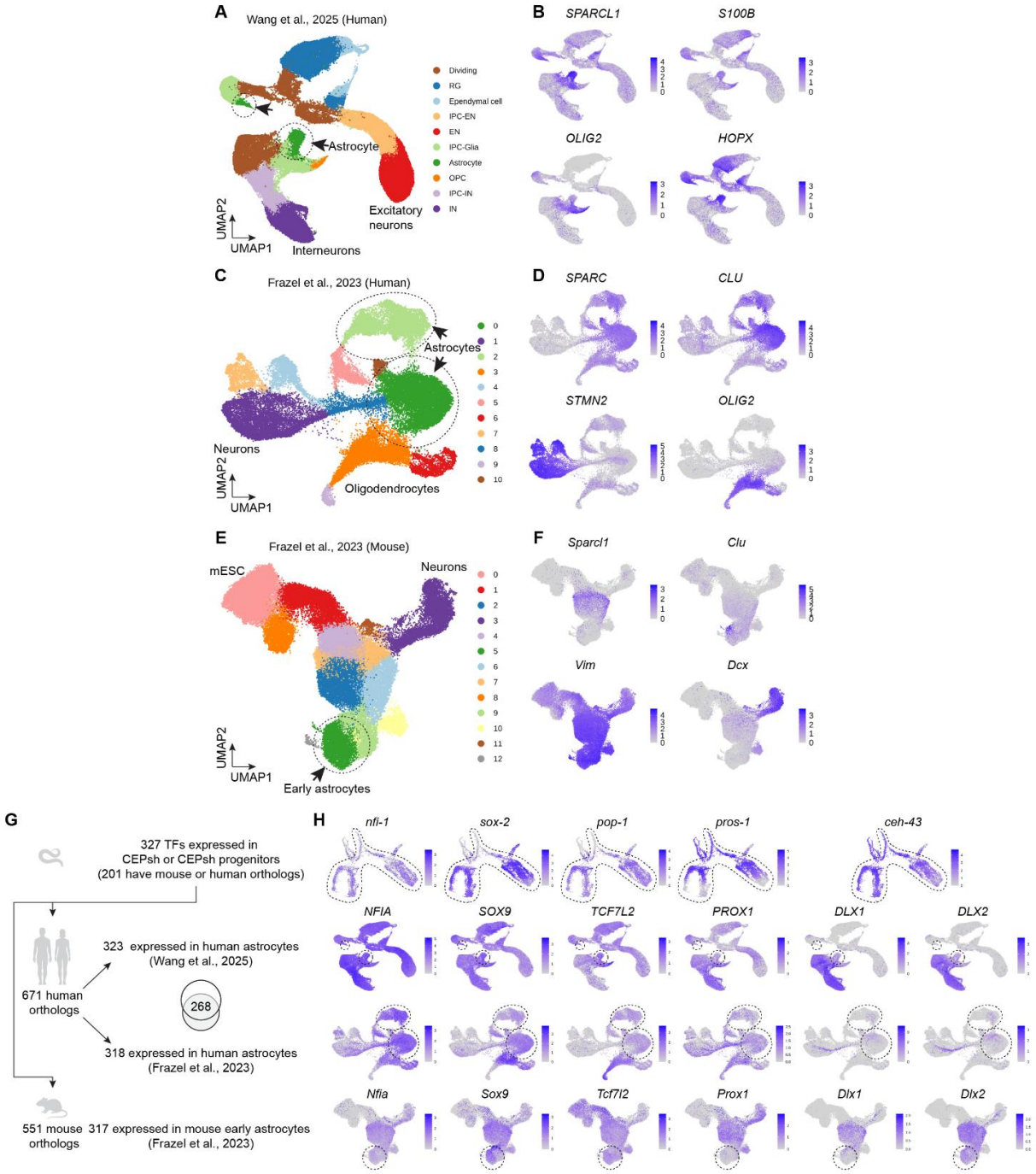

Figure S11. Shared transcription factor expression between CEPsh astrocytes and mammalian developing astrocytes

(A, B) Data reproduced from human cortical glial progenitor *in vitro* differentiation (Extended Data Fig.15, Wang et al., 2025), showing the original cell-type annotation (A) and representative marker gene expression (B).

(C, D) Reanalysis of human iPSC-derived glial differentiation scRNA-seq data from Frazel et al. (2023). UMAP visualization of cell clusters (C) and expression of representative marker genes (D).

(E, F) Reanalysis of mouse mESC-derived glial differentiation scRNA-seq data from Frazel et al. (2023). UMAP visualization of cell clusters (E) and selected marker gene expression (F).

(G) Overlap of transcription factors expressed in *C. elegans* CEPsh astrocytes or their progenitors and mammalian astrocytes.

(H) Expression patterns of selected transcription factors in CEPsh astrocytes and progenitors and their human and mouse homologs expressed in astrocytes.

REFERENCES

1. Banker, G.A. (1980). Trophic Interactions Between Astroglial Cells and Hippocampal Neurons in Culture. Science *209*, 809–810. https://doi.org/10.1126/science.7403847.

2. Christopherson, K.S., Ullian, E.M., Stokes, C.C.A., Mullowney, C.E., Hell, J.W., Agah, A., Lawler, J., Mosher, D.F., Bornstein, P., and Barres, B.A. (2005). Thrombospondins Are Astrocyte-Secreted Proteins that Promote CNS Synaptogenesis. Cell *120*, 421–433. https://doi.org/10.1016/j.cell.2004.12.020.

3. Kucukdereli, H., Allen, N.J., Lee, A.T., Feng, A., Ozlu, M.I., Conatser, L.M., Chakraborty, C., Workman, G., Weaver, M., Sage, E.H., et al. (2011). Control of excitatory CNS synaptogenesis by astrocyte-secreted proteins Hevin and SPARC. Proc. Natl. Acad. Sci. *108*, E440–E449. https://doi.org/10.1073/pnas.1104977108.

4. Allen, N.J., Bennett, M.L., Foo, L.C., Wang, G.X., Chakraborty, C., Smith, S.J., and Barres, B.A. (2012). Astrocyte glypicans 4 and 6 promote formation of excitatory synapses via GluA1 AMPA receptors. Nature *486*, 410–414. https://doi.org/10.1038/nature11059.

5. Pfrieger, F.W., and Barres, B.A. (1997). Synaptic Efficacy Enhanced by Glial Cells in Vitro. Science *277*, 1684–1687. https://doi.org/10.1126/science.277.5332.1684.

6. Chung, W.-S., Clarke, L.E., Wang, G.X., Stafford, B.K., Sher, A., Chakraborty, C., Joung, J., Foo, L.C., Thompson, A., Chen, C., et al. (2013). Astrocytes mediate synapse elimination through MEGF10 and MERTK pathways. Nature *504*, 394–400. https://doi.org/10.1038/nature12776.

7. Vainchtein, I.D., Chin, G., Cho, F.S., Kelley, K.W., Miller, J.G., Chien, E.C., Liddelow, S.A., Nguyen, P.T., Nakao-Inoue, H., Dorman, L.C., et al. (2018). Astrocyte-derived interleukin-33 promotes microglial synapse engulfment and neural circuit development. Science *359*, 1269–1273. https://doi.org/10.1126/science.aal3589.

8. Weber, B., and Barros, L.F. (2015). The Astrocyte: Powerhouse and Recycling Center. Cold Spring Harb. Perspect. Biol. *7*, a020396. https://doi.org/10.1101/cshperspect.a020396.

9. Olsen, M.L., Khakh, B.S., Skatchkov, S.N., Zhou, M., Lee, C.J., and Rouach, N. (2015). New Insights on Astrocyte Ion Channels: Critical for Homeostasis and Neuron-Glia Signaling. J. Neurosci. *35*, 13827–13835. https://doi.org/10.1523/JNEUROSCI.2603-15.2015.

10. Parpura, V., and Verkhratsky, A. (2012). Homeostatic function of astrocytes: Ca2+ and Na+ signalling. Transl. Neurosci. *3*, 334–344. https://doi.org/10.2478/s13380-012-0040-y.

11. Kimelberg, H.K. (2004). Water homeostasis in the brain: Basic concepts. Neuroscience *129*, 851–860. https://doi.org/10.1016/j.neuroscience.2004.07.033.

12. Pham, C., Komaki, Y., Deàs-Just, A., Le Gac, B., Mouffle, C., Franco, C., Chaperon, A., Vialou, V., Tsurugizawa, T., Cauli, B., et al. (2024). Astrocyte aquaporin mediates a tonic water efflux maintaining brain homeostasis. eLife *13*, RP95873. https://doi.org/10.7554/eLife.95873.

13. Mauch, D.H., Nägler, K., Schumacher, S., Göritz, C., Müller, E.-C., Otto, A., and Pfrieger, F.W. (2001). CNS Synaptogenesis Promoted by Glia-Derived Cholesterol. Science *294*, 1354–1357. https://doi.org/10.1126/science.294.5545.1354.

14. Goritz, C., Mauch, D.H., and Pfrieger, F.W. (2005). Multiple mechanisms mediate cholesterol-induced synaptogenesis in a CNS neuron. Mol. Cell. Neurosci. *29*, 190–201. https://doi.org/10.1016/j.mcn.2005.02.006.

15. Pfrieger, F.W. (2003). Outsourcing in the brain: Do neurons depend on cholesterol delivery by astrocytes? BioEssays *25*, 72–78. https://doi.org/10.1002/bies.10195.

16. Meeks, J.P., and Mennerick, S. (2003). Feeding Hungry Neurons: Astrocytes Deliver Food for Thought. Neuron *37*, 187–189. https://doi.org/10.1016/S0896-6273(03)00027-8.

17. Bélanger, M., Allaman, I., and Magistretti, P.J. (2011). Brain Energy Metabolism: Focus on Astrocyte-Neuron Metabolic Cooperation. Cell Metab. *14*, 724–738. https://doi.org/10.1016/j.cmet.2011.08.016.

18. Liu, X., Ying, J., Wang, X., Zheng, Q., Zhao, T., Yoon, S., Yu, W., Yang, D., Fang, Y., and Hua, F. (2021). Astrocytes in Neural Circuits: Key Factors in Synaptic Regulation and Potential Targets for Neurodevelopmental Disorders. Front. Mol. Neurosci. *14*. https://doi.org/10.3389/fnmol.2021.729273.

19. Hösli, L., Zuend, M., Bredell, G., Zanker, H.S., Porto de Oliveira, C.E., Saab, A.S., and Weber, B. (2022). Direct vascular contact is a hallmark of cerebral astrocytes. Cell Rep. *39*, 110599. https://doi.org/10.1016/j.celrep.2022.110599.

20. Manu, D.R., Slevin, M., Barcutean, L., Forro, T., Boghitoiu, T., and Balasa, R. (2023). Astrocyte Involvement in Blood–Brain Barrier Function: A Critical Update Highlighting Novel, Complex, Neurovascular Interactions. Int. J. Mol. Sci. *24*, 17146. https://doi.org/10.3390/ijms242417146.

21. Díaz-Castro, B., Robel, S., and Mishra, A. (2023). Astrocyte Endfeet in Brain Function and Pathology: Open Questions. Annu. Rev. Neurosci. *46*, 101–121. https://doi.org/10.1146/annurev-neuro-091922-031205.

22. Batiuk, M.Y., Martirosyan, A., Wahis, J., de Vin, F., Marneffe, C., Kusserow, C., Koeppen, J., Viana, J.F., Oliveira, J.F., Voet, T., et al. (2020). Identification of region-specific astrocyte subtypes at single cell resolution. Nat. Commun. *11*, 1220. https://doi.org/10.1038/s41467-019-14198-8.

23. Endo, F., Kasai, A., Soto, J.S., Yu, X., Qu, Z., Hashimoto, H., Gradinaru, V., Kawaguchi, R., and Khakh, B.S. (2022). Molecular basis of astrocyte diversity and morphology across the CNS in health and disease. Science *378*, eadc9020. https://doi.org/10.1126/science.adc9020.

24. Allen, D.E., Donohue, K.C., Cadwell, C.R., Shin, D., Keefe, M.G., Sohal, V.S., and Nowakowski, T.J. (2022). Fate mapping of neural stem cell niches reveals distinct origins of human cortical astrocytes. Science *376*, 1441–1446. https://doi.org/10.1126/science.abm5224.

25. Ge, W.-P., Miyawaki, A., Gage, F.H., Jan, Y.N., and Jan, L.Y. (2012). Local generation of glia is a major astrocyte source in postnatal cortex. Nature *484*, 376–380. https://doi.org/10.1038/nature10959.

26. Ware, C.B., Horowitz, M.C., Renshaw, B.R., Hunt, J.S., Liggitt, D., Koblar, S.A., Gliniak, B.C., McKenna, H.J., Papayannopoulou, T., Thoma, B., et al. (1995). Targeted disruption of the low-affinity leukemia inhibitory factor receptor gene causes placental, skeletal, neural and metabolic defects and results in perinatal death. Development *121*, 1283–1299. https://doi.org/10.1242/dev.121.5.1283.

27. Bonni, A., Sun, Y., Nadal-Vicens, M., Bhatt, A., Frank, D.A., Rozovsky, I., Stahl, N., Yancopoulos, G.D., and Greenberg, M.E. (1997). Regulation of Gliogenesis in the Central Nervous System by the JAK-STAT Signaling Pathway. Science *278*, 477–483. https://doi.org/10.1126/science.278.5337.477.

28. Rajan, P., and McKay, R.D.G. (1998). Multiple Routes to Astrocytic Differentiation in the CNS. J. Neurosci. *18*, 3620–3629. https://doi.org/10.1523/JNEUROSCI.18-10-03620.1998.

29. Ochiai, W., Yanagisawa, M., Takizawa, T., Nakashima, K., and Taga, T. (2001). ASTROCYTE DIFFERENTIATION OF FETAL NEUROEPITHELIAL CELLS INVOLVING CARDIOTROPHIN-1-INDUCED ACTIVATION OF STAT3. Cytokine *14*, 264–271. https://doi.org/10.1006/cyto.2001.0883.

30. Barnabé-Heider, F., Wasylnka, J.A., Fernandes, K.J.L., Porsche, C., Sendtner, M., Kaplan, D.R., and Miller, F.D. (2005). Evidence that Embryonic Neurons Regulate the Onset of Cortical Gliogenesis via Cardiotrophin-1. Neuron *48*, 253–265. https://doi.org/10.1016/j.neuron.2005.08.037.

31. Agius, E., Decker, Y., Soukkarieh, C., Soula, C., and Cochard, P. (2010). Role of BMPs in controlling the spatial and temporal origin of GFAP astrocytes in the embryonic spinal cord. Dev. Biol. *344*, 611–620. https://doi.org/10.1016/j.ydbio.2010.05.017.

32. Ge, W., Martinowich, K., Wu, X., He, F., Miyamoto, A., Fan, G., Weinmaster, G., and Sun, Y.E. (2002). Notch signaling promotes astrogliogenesis via direct CSL-mediated glial gene activation. J. Neurosci. Res. *69*, 848–860. https://doi.org/10.1002/jnr.10364.

33. Deneen, B., Ho, R., Lukaszewicz, A., Hochstim, C.J., Gronostajski, R.M., and Anderson, D.J. (2006). The Transcription Factor NFIA Controls the Onset of Gliogenesis in the Developing Spinal Cord. Neuron *52*, 953–968. https://doi.org/10.1016/j.neuron.2006.11.019.

34. Kang, P., Lee, H.K., Glasgow, S.M., Finley, M., Donti, T., Gaber, Z.B., Graham, B.H., Foster, A.E., Novitch, B.G., Gronostajski, R.M., et al. (2012). Sox9 and NFIA Coordinate a Transcriptional Regulatory Cascade during the Initiation of Gliogenesis. Neuron *74*, 79–94. https://doi.org/10.1016/j.neuron.2012.01.024.

35. Tchieu, J., Calder, E.L., Guttikonda, S.R., Gutzwiller, E.M., Aromolaran, K.A., Steinbeck, J.A., Goldstein, P.A., and Studer, L. (2019). NFIA is a gliogenic switch enabling rapid derivation of functional human astrocytes from pluripotent stem cells. Nat. Biotechnol. *37*, 267–275. https://doi.org/10.1038/s41587-019-0035-0.

36. Medeiros de Araújo, J.A., Barão, S., Mateos-White, I., Espinosa, A., Costa, M.R., Gil-Sanz, C., and Müller, U. (2021). ZBTB20 is crucial for the specification of a subset of callosal projection neurons and astrocytes in the mammalian neocortex. Development *148*, dev196642. https://doi.org/10.1242/dev.196642.

37. Subramanian, L., Sarkar, A., Shetty, A.S., Muralidharan, B., Padmanabhan, H., Piper, M., Monuki, E.S., Bach, I., Gronostajski, R.M., Richards, L.J., et al. (2011). Transcription factor Lhx2 is necessary and sufficient to suppress astrogliogenesis and promote neurogenesis in the developing hippocampus. Proc. Natl. Acad. Sci. *108*, E265–E274. https://doi.org/10.1073/pnas.1101109108.

38. Melo, J. de, Zibetti, C., Clark, B.S., Hwang, W., Miranda-Angulo, A.L., Qian, J., and Blackshaw, S. (2016). Lhx2 Is an Essential Factor for Retinal Gliogenesis and Notch Signaling. J. Neurosci. *36*, 2391–2405. https://doi.org/10.1523/JNEUROSCI.3145-15.2016.

39. Tiwari, N., Pataskar, A., Péron, S., Thakurela, S., Sahu, S.K., Figueres-Oñate, M., Marichal, N., López-Mascaraque, L., Tiwari, V.K., and Berninger, B. (2018). Stage-Specific Transcription Factors Drive Astrogliogenesis by Remodeling Gene Regulatory Landscapes. Cell Stem Cell *23*, 557-571.e8. https://doi.org/10.1016/j.stem.2018.09.008.

40. Hochstim, C., Deneen, B., Lukaszewicz, A., Zhou, Q., and Anderson, D.J. (2008). Identification of Positionally Distinct Astrocyte Subtypes whose Identities Are Specified by a Homeodomain Code. Cell *133*, 510–522. https://doi.org/10.1016/j.cell.2008.02.046.

41. Voigt, T. (1989). Development of glial cells in the cerebral wall of ferrets: Direct tracing of their transformation from radial glia into astrocytes. J. Comp. Neurol. *289*, 74–88. https://doi.org/10.1002/cne.902890106.

42. Culican, S.M., Baumrind, N.L., Yamamoto, M., and Pearlman, A.L. (1990). Cortical radial glia: identification in tissue culture and evidence for their transformation

to astrocytes. J. Neurosci. *10*, 684–692. https://doi.org/10.1523/JNEUROSCI.10-02-00684.1990.

43. Bonfanti, L., and Peretto, P. (2007). Radial glial origin of the adult neural stem cells in the subventricular zone. Prog. Neurobiol. *83*, 24–36. https://doi.org/10.1016/j.pneurobio.2006.11.002.

44. White, J.G., Southgate, E., Thomson, J.N., and Brenner, S. (1986). The structure of the nervous system of the nematode Caenorhabditis elegans. Philos. Trans. R. Soc. Lond. B Biol. Sci. *314*, 1–340. https://doi.org/10.1098/rstb.1986.0056.

45. Ogata, K., and Kosaka, T. (2002). Structural and quantitative analysis of astrocytes in the mouse hippocampus. Neuroscience *113*, 221–233. https://doi.org/10.1016/S0306-4522(02)00041-6.

46. Colón-Ramos, D.A., Margeta, M.A., and Shen, K. (2007). Glia Promote Local Synaptogenesis Through UNC-6 (Netrin) Signaling in C. elegans. Science *318*, 103–106. https://doi.org/10.1126/science.1143762.

47. Halassa, M.M., Fellin, T., and Haydon, P.G. (2007). The tripartite synapse: roles for gliotransmission in health and disease. Trends Mol. Med. *13*, 54–63. https://doi.org/10.1016/j.molmed.2006.12.005.

48. Katz, M., Corson, F., Keil, W., Singhal, A., Bae, A., Lu, Y., Liang, Y., and Shaham, S. (2019). Glutamate spillover in C. elegans triggers repetitive behavior through presynaptic activation of MGL-2/mGluR5. Nat. Commun. *10*, 1882. https://doi.org/10.1038/s41467-019-09581-4.

49. Aida, T., Yoshida, J., Nomura, M., Tanimura, A., Iino, Y., Soma, M., Bai, N., Ito, Y., Cui, W., Aizawa, H., et al. (2015). Astroglial glutamate transporter deficiency increases synaptic excitability and leads to pathological repetitive behaviors in mice. Neuropsychopharmacol. Off. Publ. Am. Coll. Neuropsychopharmacol. *40*, 1569–1579. https://doi.org/10.1038/npp.2015.26.

50. Rapti, G., Li, C., Shan, A., Lu, Y., and Shaham, S. (2017). Glia initiate brain assembly through noncanonical Chimaerin–Furin axon guidance in C. elegans. Nat. Neurosci. *20*, 1350–1360. https://doi.org/10.1038/nn.4630.

51. Tabata, H. (2015). Diverse subtypes of astrocytes and their development during corticogenesis. Front. Neurosci. *9*, 114. https://doi.org/10.3389/fnins.2015.00114.

52. Yoshimura, S., Murray, J.I., Lu, Y., Waterston, R.H., and Shaham, S. (2008). mls-2 and vab-3 control glia development, hlh-17/Olig expression and glia-dependent neurite extension in C. elegans. Development *135*, 2263–2275. https://doi.org/10.1242/dev.019547.

53. Packer, J.S., Zhu, Q., Huynh, C., Sivaramakrishnan, P., Preston, E., Dueck, H., Stefanik, D., Tan, K., Trapnell, C., Kim, J., et al. (2019). A lineage-resolved molecular

atlas of C. elegans embryogenesis at single-cell resolution. Science *365*, eaax1971. https://doi.org/10.1126/science.aax1971.

54. Sulston, J.E., Schierenberg, E., White, J.G., and Thomson, J.N. (1983). The embryonic cell lineage of the nematode Caenorhabditis elegans. Dev. Biol. *100*, 64–119. https://doi.org/10.1016/0012-1606(83)90201-4.

55. Hashimshony, T., Feder, M., Levin, M., Hall, B.K., and Yanai, I. (2015). Spatiotemporal transcriptomics reveals the evolutionary history of the endoderm germ layer. Nature *519*, 219–222. https://doi.org/10.1038/nature13996.

56. Li, Y., Smith, J.J., Marques, F., Osuma, A., Huang, H.-C., and Kratsios, P. (2023). Cell context-dependent CFI-1/ARID3 functions control neuronal terminal differentiation. Cell Rep. *42*, 112220. https://doi.org/10.1016/j.celrep.2023.112220.

57. Insley, P., and Shaham, S. (2018). Automated C. elegans embryo alignments reveal brain neuropil position invariance despite lax cell body placement. PLOS ONE *13*, e0194861. https://doi.org/10.1371/journal.pone.0194861.

58. Wu, Y., Ghitani, A., Christensen, R., Santella, A., Du, Z., Rondeau, G., Bao, Z., Colón-Ramos, D., and Shroff, H. (2011). Inverted selective plane illumination microscopy (*i* SPIM) enables coupled cell identity lineaging and neurodevelopmental imaging in *Caenorhabditis elegans*. Proc. Natl. Acad. Sci. *108*, 17708–17713. https://doi.org/10.1073/pnas.1108494108.

59. Wallace, S.W., Singhvi, A., Liang, Y., Lu, Y., and Shaham, S. (2016). PROS-1/Prospero Is a Major Regulator of the Glia-Specific Secretome Controlling Sensory-Neuron Shape and Function in *C. elegans*. Cell Rep. *15*, 550–562. https://doi.org/10.1016/j.celrep.2016.03.051.

60. Ma, X., Zhao, Z., Xiao, L., Xu, W., Kou, Y., Zhang, Y., Wu, G., Wang, Y., and Du, Z. (2021). A 4D single-cell protein atlas of transcription factors delineates spatiotemporal patterning during embryogenesis. Nat. Methods *18*, 893–902. https://doi.org/10.1038/s41592-021-01216-1.

61. Taylor, S.R., Santpere, G., Weinreb, A., Barrett, A., Reilly, M.B., Xu, C., Varol, E., Oikonomou, P., Glenwinkel, L., McWhirter, R., et al. (2021). Molecular topography of an entire nervous system. Cell *184*, 4329-4347.e23. https://doi.org/10.1016/j.cell.2021.06.023.

62. Hao, Y., Hao, S., Andersen-Nissen, E., Mauck, W.M., Zheng, S., Butler, A., Lee, M.J., Wilk, A.J., Darby, C., Zager, M., et al. (2021). Integrated analysis of multimodal single-cell data. Cell *184*, 3573-3587.e29. https://doi.org/10.1016/j.cell.2021.04.048.

63. Nakano, S., Ellis, R.E., and Horvitz, H.R. (2010). Otx-dependent expression of proneural bHLH genes establishes a neuronal bilateral asymmetry in C. elegans. Development *137*, 4017–4027. https://doi.org/10.1242/dev.058834.

64. Christensen, E.L., Beasley, A., Radchuk, J., Mielko, Z.E., Preston, E., Stuckett, S., Murray, J.I., and Hudson, M.L. (2020). ngn-1/neurogenin Activates Transcription of Multiple Terminal Selector Transcription Factors in the Caenorhabditis elegans Nervous System. G3 GenesGenomesGenetics *10*, 1949–1962. https://doi.org/10.1534/g3.120.401126.

65. Hobert, O. (2016). Chapter Twenty-Five - Terminal Selectors of Neuronal Identity. In Current Topics in Developmental Biology Essays on Developmental Biology, Part A., P. M. Wassarman, ed. (Academic Press), pp. 455–475. https://doi.org/10.1016/bs.ctdb.2015.12.007.

66. Flames, N., and Hobert, O. (2009). Gene regulatory logic of dopamine neuron differentiation. Nature *458*, 885–889. https://doi.org/10.1038/nature07929.

67. Bertrand, V., Bisso, P., Poole, R.J., and Hobert, O. (2011). Notch-Dependent Induction of Left/Right Asymmetry in C. elegans Interneurons and Motoneurons. Curr. Biol. *21*, 1225–1231. https://doi.org/10.1016/j.cub.2011.06.016.

68. Sze, J.Y., Zhang, S., Li, J., and Ruvkun, G. (2002). The C. elegans POU-domain transcription factor UNC-86 regulates the tph-1 tryptophan hydroxylase gene and neurite outgrowth in specific serotonergic neurons. Development *129*, 3901–3911. https://doi.org/10.1242/dev.129.16.3901.

69. Weirauch, M.T., Yang, A., Albu, M., Cote, A.G., Montenegro-Montero, A., Drewe, P., Najafabadi, H.S., Lambert, S.A., Mann, I., Cook, K., et al. (2014). Determination and Inference of Eukaryotic Transcription Factor Sequence Specificity. Cell *158*, 1431–1443. https://doi.org/10.1016/j.cell.2014.08.009.

70. Reece-Hoyes, J.S., Deplancke, B., Shingles, J., Grove, C.A., Hope, I.A., and Walhout, A.J. (2005). A compendium of Caenorhabditis elegans regulatory transcription factors: a resource for mapping transcription regulatory networks. Genome Biol. *6*, R110. https://doi.org/10.1186/gb-2005-6-13-r110.

71. Kennedy, S., Wang, D., and Ruvkun, G. (2004). A conserved siRNA-degrading RNase negatively regulates RNA interference in C. elegans. Nature *427*, 645–649. https://doi.org/10.1038/nature02302.

72. Weirauch, M.T., Yang, A., Albu, M., Cote, A.G., Montenegro-Montero, A., Drewe, P., Najafabadi, H.S., Lambert, S.A., Mann, I., Cook, K., et al. (2014). Determination and Inference of Eukaryotic Transcription Factor Sequence Specificity. Cell *158*, 1431–1443. https://doi.org/10.1016/j.cell.2014.08.009.

73. Reece-Hoyes, J.S., Deplancke, B., Shingles, J., Grove, C.A., Hope, I.A., and Walhout, A.J. (2005). A compendium of Caenorhabditis elegans regulatory transcription factors: a resource for mapping transcription regulatory networks. Genome Biol. *6*, R110. https://doi.org/10.1186/gb-2005-6-13-r110.

74. Shen, K., Fetter, R.D., and Bargmann, C.I. (2004). Synaptic Specificity Is Generated by the Synaptic Guidepost Protein SYG-2 and Its Receptor, SYG-1. Cell *116*, 869–881. https://doi.org/10.1016/S0092-8674(04)00251-X.

75. Özkan, E., Chia, P.H., Wang, R.R., Goriatcheva, N., Borek, D., Otwinowski, Z., Walz, T., Shen, K., and Garcia, K.C. (2014). Extracellular Architecture of the SYG-1/SYG-2 Adhesion Complex Instructs Synaptogenesis. Cell *156*, 482–494. https://doi.org/10.1016/j.cell.2014.01.004.

76. Sengupta, T., Koonce, N.L., Vázquez-Martínez, N., Moyle, M.W., Duncan, L.H., Emerson, S.E., Han, X., Shao, L., Wu, Y., Santella, A., et al. (2021). Differential adhesion regulates neurite placement via a retrograde zippering mechanism. eLife *10*, e71171. https://doi.org/10.7554/eLife.71171.

77. Tucker, D.K., Adams, C.S., Prasad, G., and Ackley, B.D. (2022). The Immunoglobulin Superfamily Members syg-2 and syg-1 Regulate Neurite Development in C. elegans. J. Dev. Biol. *10*, 3. https://doi.org/10.3390/jdb10010003.

78. Buyannemekh, K., Villoutreix, P., and Bertrand, V. (2025). Left/right asymmetrically expressed ephrin and Flamingo proteins regulate lateralized axon growth in *C. elegans*. Dev. Biol. *517*, 117–125. https://doi.org/10.1016/j.ydbio.2024.09.014.

79. Purice, M.D., Quitevis, E.J.A., Manning, R.S., Severs, L.J., Tran, N.-T., Sorrentino, V., Finkbeiner, C., Wu, F., Zager, M., Setty, M., et al. (2025). Molecular profiling of adult C. elegans glia across sexes by single-nuclear RNA-seq. Dev. Cell *0*. https://doi.org/10.1016/j.devcel.2025.05.013.

80. Norris, C.R., and Kalil, K. (1991). Guidance of callosal axons by radial glia in the developing cerebral cortex. J. Neurosci. *11*, 3481–3492. https://doi.org/10.1523/JNEUROSCI.11-11-03481.1991.

81. Kaur, N., Han, W., Li, Z., Madrigal, M.P., Shim, S., Pochareddy, S., Gulden, F.O., Li, M., Xu, X., Xing, X., et al. (2020). Neural Stem Cells Direct Axon Guidance via Their Radial Fiber Scaffold. Neuron *107*, 1197-1211.e9. https://doi.org/10.1016/j.neuron.2020.06.035.

82. Aspöck, G., and Bürglin, T.R. (2001). The Caenorhabditis elegans Distal-less ortholog ceh-43 is required for development of the anterior hypodermis. Dev. Dyn. *222*, 403–409. https://doi.org/10.1002/dvdy.1201.

83. Nishimura, K., Fukagawa, T., Takisawa, H., Kakimoto, T., and Kanemaki, M. (2009). An auxin-based degron system for the rapid depletion of proteins in nonplant cells. Nat. Methods *6*, 917–922. https://doi.org/10.1038/nmeth.1401.

84. Zhang, L., Ward, J.D., Cheng, Z., and Dernburg, A.F. (2015). The auxin-inducible degradation (AID) system enables versatile conditional protein depletion in C. elegans. Development *142*, 4374–4384. https://doi.org/10.1242/dev.129635.

85. Tang, J.L.Y., Hakes, A.E., Krautz, R., Suzuki, T., Contreras, E.G., Fox, P.M., and Brand, A.H. (2022). NanoDam identifies Homeobrain (ARX) and Scarecrow (NKX2.1) as conserved temporal factors in the Drosophila central brain and visual system. Dev. Cell *57*, 1193-1207.e7. https://doi.org/10.1016/j.devcel.2022.04.008.

86. Gómez-Saldivar, G., Osuna-Luque, J., Semple, J.I., Glauser, D.A., Jarriault, S., and Meister, P. (2020). Tissue-Specific Transcription Footprinting Using RNA Pol DamID (RAPID) in Caenorhabditis elegans. Genetics *216*, 931–945. https://doi.org/10.1534/genetics.120.303774.

87. Greer, E.L., Blanco, M.A., Gu, L., Sendinc, E., Liu, J., Aristizábal-Corrales, D., Hsu, C.-H., Aravind, L., He, C., and Shi, Y. (2015). DNA Methylation on N6-Adenine in *C. elegans*. Cell *161*, 868–878. https://doi.org/10.1016/j.cell.2015.04.005.

88. Amit, M., Donyo, M., Hollander, D., Goren, A., Kim, E., Gelfman, S., Lev-Maor, G., Burstein, D., Schwartz, S., Postolsky, B., et al. (2012). Differential GC Content between Exons and Introns Establishes Distinct Strategies of Splice-Site Recognition. Cell Rep. *1*, 543–556. https://doi.org/10.1016/j.celrep.2012.03.013.

89. Kudron, M., Gevirtzman, L., Victorsen, A., Lear, B.C., Gao, J., Xu, J., Samanta, S., Frink, E., Tran-Pearson, A., Huynh, C., et al. (2024). Binding profiles for 961 Drosophila and C. elegans transcription factors reveal tissue-specific regulatory relationships. Genome Res. *34*, 2319–2334. https://doi.org/10.1101/gr.279037.124.

90. Mizumoto, K., and Sawa, H. (2007). Two βs or not two βs: regulation of asymmetric division by β-catenin. Trends Cell Biol. *17*, 465–473. https://doi.org/10.1016/j.tcb.2007.08.004.

91. Alqadah, A., Hsieh, Y., Vidal, B., Chang, C., Hobert, O., and Chuang, C. (2015). Postmitotic diversification of olfactory neuron types is mediated by differential activities of the HMG‐box transcription factor SOX‐2. EMBO J. *34*, 2574–2589. https://doi.org/10.15252/embj.201592188.

92. Melone, M., Ciriachi, C., Pietrobon, D., and Conti, F. (2019). Heterogeneity of Astrocytic and Neuronal GLT-1 at Cortical Excitatory Synapses, as Revealed by its Colocalization With Na+/K+-ATPase α Isoforms. Cereb. Cortex *29*, 3331–3350. https://doi.org/10.1093/cercor/bhy203.

93. Cholet, N., Pellerin, L., Magistretti, P.J., and Hamel, E. (2002). Similar Perisynaptic Glial Localization for the Na+,K+-ATPase α2 Subunit and the Glutamate Transporters GLAST and GLT-1 in the Rat Somatosensory Cortex. Cereb. Cortex *12*, 515–525. https://doi.org/10.1093/cercor/12.5.515.

94. Rose, E.M., Koo, J.C.P., Antflick, J.E., Ahmed, S.M., Angers, S., and Hampson, D.R. (2009). Glutamate Transporter Coupling to Na,K-ATPase. J. Neurosci. *29*, 8143–8155. https://doi.org/10.1523/JNEUROSCI.1081-09.2009.

95. Romanos, J., Benke, D., Pietrobon, D., Zeilhofer, H.U., and Santello, M. (2020). Astrocyte dysfunction increases cortical dendritic excitability and promotes cranial pain in familial migraine. Sci. Adv. *6*, eaaz1584. https://doi.org/10.1126/sciadv.aaz1584.

96. Nagai, J., Yu, X., Papouin, T., Cheong, E., Freeman, M.R., Monk, K.R., Hastings, M.H., Haydon, P.G., Rowitch, D., Shaham, S., et al. (2021). Behaviorally consequential astrocytic regulation of neural circuits. Neuron *109*, 576–596. https://doi.org/10.1016/j.neuron.2020.12.008.

97. Wang, L., Wang, C., Moriano, J.A., Chen, S., Zuo, G., Cebrián-Silla, A., Zhang, S., Mukhtar, T., Wang, S., Song, M., et al. (2025). Molecular and cellular dynamics of the developing human neocortex. Nature, 1–10. https://doi.org/10.1038/s41586-024-08351-7.

98. Frazel, P.W., Labib, D., Fisher, T., Brosh, R., Pirjanian, N., Marchildon, A., Boeke, J.D., Fossati, V., and Liddelow, S.A. (2023). Longitudinal scRNA-seq analysis in mouse and human informs optimization of rapid mouse astrocyte differentiation protocols. Nat. Neurosci. *26*, 1726–1738. https://doi.org/10.1038/s41593-023-01424-2.

99. Szewczyk, L.M., Lipiec, M.A., Liszewska, E., Meyza, K., Urban-Ciecko, J., Kondrakiewicz, L., Goncerzewicz, A., Rafalko, K., Krawczyk, T.G., Bogaj, K., et al. (2024). Astrocytic β-catenin signaling via TCF7L2 regulates synapse development and social behavior. Mol. Psychiatry *29*, 57–73. https://doi.org/10.1038/s41380-023-02281-y.

100. Freeman, M.R., and Doe, C.Q. (2001). Asymmetric Prospero localization is required to generate mixed neuronal/glial lineages in the Drosophila CNS. Development *128*, 4103–4112. https://doi.org/10.1242/dev.128.20.4103.

101. Stergiopoulos, A., Elkouris, M., and Politis, P.K. (2015). Prospero-related homeobox 1 (Prox1) at the crossroads of diverse pathways during adult neural fate specification. Front. Cell. Neurosci. *8*, 454. https://doi.org/10.3389/fncel.2014.00454.

102. Anderson, S.A., Eisenstat, D.D., Shi, L., and Rubenstein, J.L.R. (1997). Interneuron Migration from Basal Forebrain to Neocortex: Dependence on Dlx Genes. Science *278*, 474–476. https://doi.org/10.1126/science.278.5337.474.

103. Andrews, G.L., Yun, K., Rubenstein, J.L.R., and Mastick, G.S. (2003). Dlx transcription factors regulate differentiation of dopaminergic neurons of the ventral thalamus. Mol. Cell. Neurosci. *23*, 107–120. https://doi.org/10.1016/S1044-7431(03)00016-2.

104. Brill, M.S., Snapyan, M., Wohlfrom, H., Ninkovic, J., Jawerka, M., Mastick, G.S., Ashery-Padan, R., Saghatelyan, A., Berninger, B., and Götz, M. (2008). A Dlx2- and Pax6-Dependent Transcriptional Code for Periglomerular Neuron Specification in the

Adult Olfactory Bulb. J. Neurosci. *28*, 6439–6452. https://doi.org/10.1523/JNEUROSCI.0700-08.2008.

105. Le, T.N., Zhou, Q.-P., Cobos, I., Zhang, S., Zagozewski, J., Japoni, S., Vriend, J., Parkinson, T., Du, G., Rubenstein, J.L., et al. (2017). GABAergic Interneuron Differentiation in the Basal Forebrain Is Mediated through Direct Regulation of Glutamic Acid Decarboxylase Isoforms by Dlx Homeobox Transcription Factors. J. Neurosci. *37*, 8816–8829. https://doi.org/10.1523/JNEUROSCI.2125-16.2017.

106. Uhlén, M., Fagerberg, L., Hallström, B.M., Lindskog, C., Oksvold, P., Mardinoglu, A., Sivertsson, Å., Kampf, C., Sjöstedt, E., Asplund, A., et al. (2015). Tissue-based map of the human proteome. Science *347*, 1260419. https://doi.org/10.1126/science.1260419.

107. Doitsidou, M., Flames, N., Topalidou, I., Abe, N., Felton, T., Remesal, L., Popovitchenko, T., Mann, R., Chalfie, M., and Hobert, O. (2013). A combinatorial regulatory signature controls terminal differentiation of the dopaminergic nervous system in C. elegans. Genes Dev. *27*, 1391–1405. https://doi.org/10.1101/gad.217224.113.

108. Marshall, C.A.G., and Goldman, J.E. (2002). Subpallial Dlx2-Expressing Cells Give Rise to Astrocytes and Oligodendrocytes in the Cerebral Cortex and White Matter. J. Neurosci. *22*, 9821–9830. https://doi.org/10.1523/JNEUROSCI.22-22-09821.2002.

109. Zhang, Y., Li, B., Cananzi, S., Han, C., Wang, L.-L., Zou, Y., Fu, Y.-X., Hon, G.C., and Zhang, C.-L. (2022). A single factor elicits multilineage reprogramming of astrocytes in the adult mouse striatum. Proc. Natl. Acad. Sci. *119*, e2107339119. https://doi.org/10.1073/pnas.2107339119.

110. Lin, R., Hill, R.J., and Priess, J.R. (1998). POP-1 and Anterior–Posterior Fate Decisions in C. elegans Embryos. Cell *92*, 229–239. https://doi.org/10.1016/S0092-8674(00)80917-4.

111. Park, F.D., and Priess, J.R. (2003). Establishment of POP-1 asymmetry in early C. elegansembryos. Development *130*, 3547–3556. https://doi.org/10.1242/dev.00563.

112. Paina, S., Garzotto, D., DeMarchis, S., Marino, M., Moiana, A., Conti, L., Cattaneo, E., Perera, M., Corte, G., Calautti, E., et al. (2011). Wnt5a Is a Transcriptional Target of Dlx Homeogenes and Promotes Differentiation of Interneuron Progenitors In Vitro and In Vivo. J. Neurosci. *31*, 2675–2687. https://doi.org/10.1523/JNEUROSCI.3110-10.2011.

113. Hobert, O. (2008). Regulatory logic of neuronal diversity: Terminal selector genes and selector motifs. Proc. Natl. Acad. Sci. *105*, 20067–20071. https://doi.org/10.1073/pnas.0806070105.

114. Hobert, O., and Kratsios, P. (2019). Neuronal identity control by terminal selectors in worms, flies, and chordates. Curr. Opin. Neurobiol. *56*, 97–105. https://doi.org/10.1016/j.conb.2018.12.006.

115. Stefanakis, N., Jiang, J., Liang, Y., and Shaham, S. (2024). LET-381/FoxF and its target UNC-30/Pitx2 specify and maintain the molecular identity of C. elegans mesodermal glia that regulate motor behavior. EMBO J. *43*, 956–992. https://doi.org/10.1038/s44318-024-00049-w.

116. Stefanakis, N., Xi, J., Jiang, J., and Shaham, S. (2025). Caenorhabditis elegans LET-381 and DMD-4 control development of the mesodermal HMC endothelial cell. Development *152*, dev204622. https://doi.org/10.1242/dev.204622.

117. Mizeracka, K., Rogers, J.M., Rumley, J.D., Shaham, S., Bulyk, M.L., Murray, J.I., and Heiman, M.G. (2021). Lineage-specific control of convergent differentiation by a Forkhead repressor. Development *148*, dev199493. https://doi.org/10.1242/dev.199493.

118. EPIC database: Expression Patterns In Caenorhabditis. https://epic.gs.washington.edu/Epic2/.

119. Cole, A.G., Hashimshony, T., Du, Z., and Yanai, I. (2023). Gene regulatory patterning codes in early cell fate specification of the C. elegans embryo. eLife *12*. https://doi.org/10.7554/eLife.87099.2.

120. Burght, S.N. van der, Carelli, F.N., Appert, A., Dong, Y., Hill, M., Buttress, T., Butler, R., and Ahringer, J. (2024). A lineage-resolved multimodal single-cell atlas reveals the genomic dynamics of early C. elegans development. Preprint at bioRxiv, https://doi.org/10.1101/2024.12.02.626321 https://doi.org/10.1101/2024.12.02.626321.

121. Large, C.R.L., Khanal, R., Hillier, L., Huynh, C., Kubo, C., Kim, J., Waterston, R.H., and Murray, J.I. (2025). Lineage-resolved analysis of embryonic gene expression evolution in C. elegans and C. briggsae. Science *388*, eadu8249. https://doi.org/10.1126/science.adu8249.

122. Qiu, C., Martin, B.K., Welsh, I.C., Daza, R.M., Le, T.-M., Huang, X., Nichols, E.K., Taylor, M.L., Fulton, O., O'Day, D.R., et al. (2024). A single-cell time-lapse of mouse prenatal development from gastrula to birth. Nature *626*, 1084–1093. https://doi.org/10.1038/s41586-024-07069-w.

123. Labouesse, M., Hartwieg, E., and Horvitz, H.R. (1996). The Caenorhabditis elegans LIN-26 protein is required to specify and/or maintain all non-neuronal ectodermal cell fates. Development *122*, 2579–2588. https://doi.org/10.1242/dev.122.9.2579.

124. The C. elegans Deletion Mutant Consortium (2012). Large-Scale Screening for Targeted Knockouts in the Caenorhabditis elegans Genome. G3 GenesGenomesGenetics *2*, 1415–1425. https://doi.org/10.1534/g3.112.003830.

125. Reilly, M.B., Tekieli, T., Cros, C., Aguilar, G.R., Lao, J., Toker, I.A., Vidal, B., Leyva-Díaz, E., Bhattacharya, A., Cook, S.J., et al. (2022). Widespread employment of conserved C. elegans homeobox genes in neuronal identity specification. PLOS Genet. *18*, e1010372. https://doi.org/10.1371/journal.pgen.1010372.

126. Zacharias, A.L., Walton, T., Preston, E., and Murray, J.I. (2015). Quantitative Differences in Nuclear β-catenin and TCF Pattern Embryonic Cells in C. elegans. PLOS Genet. *11*, e1005585. https://doi.org/10.1371/journal.pgen.1005585.

127. Sarov, M., Schneider, S., Pozniakovski, A., Roguev, A., Ernst, S., Zhang, Y., Hyman, A.A., and Stewart, A.F. (2006). A recombineering pipeline for functional genomics applied to Caenorhabditis elegans. Nat. Methods *3*, 839–844. https://doi.org/10.1038/nmeth933.

128. Niu, W., Lu, Z.J., Zhong, M., Sarov, M., Murray, J.I., Brdlik, C.M., Janette, J., Chen, C., Alves, P., Preston, E., et al. (2011). Diverse transcription factor binding features revealed by genome-wide ChIP-seq in C. elegans. Genome Res. *21*, 245–254. https://doi.org/10.1101/gr.114587.110.

129. Stempor, P., and Ahringer, J. (2016). SeqPlots – Interactive software for exploratory data analyses, pattern discovery and visualization in genomics. Wellcome Open Res. *1*, 14. https://doi.org/10.12688/wellcomeopenres.10004.1.

130. Bao, Z., Murray, J.I., Boyle, T., Ooi, S.L., Sandel, M.J., and Waterston, R.H. (2006). Automated cell lineage tracing in Caenorhabditis elegans. Proc. Natl. Acad. Sci. *103*, 2707–2712. https://doi.org/10.1073/pnas.0511111103.

131. Brenner, S. (1974). THE GENETICS OF CAENORHABDITIS ELEGANS. Genetics *77*, 71–94. https://doi.org/10.1093/genetics/77.1.71.

132. Stiernagle, T. (2006). Maintenance of C. elegans. In WormBook: The Online Review of C. elegans Biology [Internet] (WormBook).

133. Doyle, J.P., Dougherty, J.D., Heiman, M., Schmidt, E.F., Stevens, T.R., Ma, G., Bupp, S., Shrestha, P., Shah, R.D., Doughty, M.L., et al. (2008). Application of a Translational Profiling Approach for the Comparative Analysis of CNS Cell Types. Cell *135*, 749–762. https://doi.org/10.1016/j.cell.2008.10.029.

134. Zhang, S., and Kuhn, J.R. (2018). Cell isolation and culture. In WormBook: The Online Review of C. elegans Biology [Internet] (WormBook).

135. Fleming, S.J., Chaffin, M.D., Arduini, A., Akkad, A.-D., Banks, E., Marioni, J.C., Philippakis, A.A., Ellinor, P.T., and Babadi, M. (2022). Unsupervised removal of systematic background noise from droplet-based single-cell experiments using

CellBender. Preprint at bioRxiv, https://doi.org/10.1101/791699 https://doi.org/10.1101/791699.

136. Germain, P.-L., Lun, A., Meixide, C.G., Macnair, W., and Robinson, M.D. (2022). Doublet identification in single-cell sequencing data using *scDblFinder*. Preprint at F1000Research, https://doi.org/10.12688/f1000research.73600.2 https://doi.org/10.12688/f1000research.73600.2.

137. McGinnis, C.S., Murrow, L.M., and Gartner, Z.J. (2019). DoubletFinder: Doublet Detection in Single-Cell RNA Sequencing Data Using Artificial Nearest Neighbors. Cell Syst. *8*, 329-337.e4. https://doi.org/10.1016/j.cels.2019.03.003.

138. Murray, J.I., Boyle, T.J., Preston, E., Vafeados, D., Mericle, B., Weisdepp, P., Zhao, Z., Bao, Z., Boeck, M., and Waterston, R.H. (2012). Multidimensional regulation of gene expression in the C. elegans embryo. Genome Res. *22*, 1282–1294. https://doi.org/10.1101/gr.131920.111.

139. Reilly, M.B., Cros, C., Varol, E., Yemini, E., and Hobert, O. (2020). Unique homeobox codes delineate all the neuron classes of C. elegans. Nature *584*, 595–601. https://doi.org/10.1038/s41586-020-2618-9.

140. Jacoby, W.G. (2000). Loess:: a nonparametric, graphical tool for depicting relationships between variables. Elect. Stud. *19*, 577–613. https://doi.org/10.1016/S0261-3794(99)00028-1.

141. Wu, T., Hu, E., Xu, S., Chen, M., Guo, P., Dai, Z., Feng, T., Zhou, L., Tang, W., Zhan, L., et al. (2021). clusterProfiler 4.0: A universal enrichment tool for interpreting omics data. The Innovation *2*, 100141. https://doi.org/10.1016/j.xinn.2021.100141.

142. Yu, G., Wang, L.-G., Han, Y., and He, Q.-Y. (2012). clusterProfiler: an R Package for Comparing Biological Themes Among Gene Clusters. OMICS J. Integr. Biol. *16*, 284–287. https://doi.org/10.1089/omi.2011.0118.

143. Trapnell, C., Cacchiarelli, D., Grimsby, J., Pokharel, P., Li, S., Morse, M., Lennon, N.J., Livak, K.J., Mikkelsen, T.S., and Rinn, J.L. (2014). The dynamics and regulators of cell fate decisions are revealed by pseudotemporal ordering of single cells. Nat. Biotechnol. *32*, 381–386. https://doi.org/10.1038/nbt.2859.

144. Qiu, X., Mao, Q., Tang, Y., Wang, L., Chawla, R., Pliner, H.A., and Trapnell, C. (2017). Reversed graph embedding resolves complex single-cell trajectories. Nat. Methods *14*, 979–982. https://doi.org/10.1038/nmeth.4402.

145. Cao, J., Spielmann, M., Qiu, X., Huang, X., Ibrahim, D.M., Hill, A.J., Zhang, F., Mundlos, S., Christiansen, L., Steemers, F.J., et al. (2019). The single-cell transcriptional landscape of mammalian organogenesis. Nature *566*, 496–502. https://doi.org/10.1038/s41586-019-0969-x.

146. Marshall, O.J., Southall, T.D., Cheetham, S.W., and Brand, A.H. (2016). Cell-type-specific profiling of protein–DNA interactions without cell isolation using targeted DamID with next-generation sequencing. Nat. Protoc. *11*, 1586–1598. https://doi.org/10.1038/nprot.2016.084.

147. Rohland, N., and Reich, D. (2012). Cost-effective, high-throughput DNA sequencing libraries for multiplexed target capture. Genome Res. *22*, 939–946. https://doi.org/10.1101/gr.128124.111.

148. Kim, W., Underwood, R.S., Greenwald, I., and Shaye, D.D. (2018). OrthoList 2: A New Comparative Genomic Analysis of Human and Caenorhabditis elegans Genes. Genetics *210*, 445–461. https://doi.org/10.1534/genetics.118.301307.

149. Dyer, S.C., Austine-Orimoloye, O., Azov, A.G., Barba, M., Barnes, I., Barrera-Enriquez, V.P., Becker, A., Bennett, R., Beracochea, M., Berry, A., et al. (2025). Ensembl 2025. Nucleic Acids Res. *53*, D948–D957. https://doi.org/10.1093/nar/gkae1071.

150. Conte Jr., D., MacNeil, L.T., Walhout, A.J.M., and Mello, C.C. (2015). RNA Interference in Caenorhabditis elegans. Curr. Protoc. Mol. Biol. *109*, 26.3.1-26.3.30. https://doi.org/10.1002/0471142727.mb2603s109.

151. Kamath, R.S., and Ahringer, J. (2003). Genome-wide RNAi screening in *Caenorhabditis elegans*. Methods *30*, 313–321. https://doi.org/10.1016/S1046-2023(03)00050-1.

152. Boyle, T.J., Bao, Z., Murray, J.I., Araya, C.L., and Waterston, R.H. (2006). AceTree: a tool for visual analysis of Caenorhabditis elegans embryogenesis. BMC Bioinformatics *7*, 275. https://doi.org/10.1186/1471-2105-7-275.

153. Medrihan, L., Knudsen, M.G., Ferraro, T., Del Cioppo Vasques, P., Romin, Y., Fujisawa, S., Greengard, P., and Milosevic, A. (2025). Projections from ventral hippocampus to nucleus accumbens' cholinergic neurons are altered in depression. J. Gen. Physiol. *157*, e202413693. https://doi.org/10.1085/jgp.202413693.

STAR★METHODS

KEY RESOURCES TABLE

REAGENT OR RESOURCE	SOURCE	IDENTIFIER
Antibodies		
DLX1 (E4T1L) Rabbit mAb	Cell Signaling Technology	96585
DLX2 Polyclonal antibody (rabbit)	Proteintech	26244-1-AP
Goat anti-Rabbit IgG (H+L) Secondary Antibody, Alexa Fluor™ 488	Invitrogen	A-11008
Goat anti-Chicken IgY (H+L) Cross-Adsorbed Secondary Antibody, Alexa Fluor™ Plus 488	Invitrogen	A32931
Goat anti-Rabbit IgG (H+L) Highly Cross-Adsorbed Secondary Antibody, Alexa Fluor™ 568	Invitrogen	A-11036
Goat anti-Chicken IgY (H+L) Secondary Antibody, Alexa Fluor™ 594	Invitrogen	A-11042
Anti-Glial Fibrillary Acidic Protein Antibody	Aves Labs	GFAP
Anti-GFP antibody	Abcam	ab13970
Bacterial and virus strains		
E. coli OP50	CGC	https://cgc.umn.edu/strain/OP50
E. coli dam–/dcm–	NEB	C2925
Biological samples		
Mouse CD1 Brain Mixed Astrocytes	Lonza	M-ASM-430
Chemicals, peptides, and recombinant proteins		
DpnI	New England Biolabs	R0176S
DpnII	New England Biolabs	R0543S
AlwI	New England Biolabs	R0513S
T4 DNA Ligase	New England Biolabs	M0202S
T4 DNA polymerase	New England Biolabs	M0203S
Klenow fragment	New England Biolabs	M0210S
T4 Polynucleotide Kinase	New England Biolabs	M0201S
Klenow Fragment (3'→5' exo-)	New England Biolabs	M0212S
EDTA (0.5 M), pH 8.0, RNase-free	Invitrogen	AM9260G
NEBNext® High-Fidelity 2X PCR Master Mix	New England Biolabs	M0541S
IPTG	Sigma-Aldrich	I6758
Sodium hypochlorite solution	Sigma-Aldrich	239305-500ML
Sucrose (Crystalline/Certified ACS)	Fisher Chemical	S5-3
Chitinase from *Trichoderma viride*	Sigma-Aldrich	C8241
Protease from *Streptomyces griseus*	Sigma-Aldrich	P8811
Bovine Serum Albumin	Sigma-Aldrich	A9647-50G
DAPI (4' ,6-diamidino-2-phenylindole)	Thermo Fisher Scientific	62248
Poly-L-Lysine, 0.01% solution	Sigma-Aldrich	P4832
Poly-D-lysine	Sigma-Aldrich	P1024-50MG

Laminin	Gibco	23-017-015
DPBS	Gibco	14190-144
Triton X-100	Sigma-Aldrich	T8787
Normal Goat Serum Blocking Solution	Vector Laboratories	S-1000-20
Tween-20	Sigma-Aldrich	P9416
SlowFade™ Gold Antifade Mountant	Invitrogen	S36940
Hoechst 33342	Thermo Fisher Scientific	62249
Critical commercial assays		
QIAamp® DNA Micro Kit	Qiagen	56304
QIAquick PCR Purification Kit	Qiagen	28104
Sera-Mag Speed Bead Magnetic Carboxylate	Cytiva	65152105050250
Advantage 2 cDNA polymerase	Clontech	639201
Qubit™ 1X dsDNA High Sensitivity	Invitrogen	Q33230
Millex™-SV 5.0 µm Filter Unit (Sterile)	Sigma-Aldrich	SLSV025LS
Fisherbrand 24×50-1 microscope cover glass	Thermo Fisher Scientific	12545F
Posi-Click Microcentrifuge Tubes	Denville Scientific Inc.	C2170
AGM™ Astrocyte Growth Medium BulletKit	Lonza	CC-3186
Deposited data		
Raw scRNA-seq and NanoDam data	This study	PRJDB37786
Raw and processed scRNA-seq and NanoDam data, and code for analysis and generating figures	This study	Zenodo (DOI: 10.5281/zenodo.17114839)
Experimental models: Cell lines		
P19 cell line	ATCC	CRL-1825
Experimental models: Organisms/strains		
Mouse: *B6;FVB-Tg(Aldh1l1-EGFP/Rpl10a)JD130Htz/J*	The Jackson Laboratory	# 030247
C. elegans: Strain N2	Caenorhabditis Genetics Center	WormBase: N2; WormBase: WBStrain00000001
unc-119(ed3) III; zuIs178 [his-72(1kb 5' UTR)::his-72::SRPVAT::GFP::his-72 (1KB 3' UTR) + 5.7 kb XbaI - HindIII unc-119(+)]; stIs10462[[ceh-32::H1-wCherry::his-24::mCherry + unc-119(+)]	CGC, Waterston lab	RW10584
ujIs113 [pie-1p::mCherry::H2B::pie-1 3'UTR + nhr-2p::mCherry::his-24::let-858 3'UTR + unc-119(+)] II; vab-3(dev190([vab-3::mNeonGreen]) X	CGC[60]	SYS633
vab-3(dev190([vab-3::mNeonGreen]) X; stIs10462 [ceh-32::H1-Wcherry::his-24::mCherry + unc-119(+)]	This study, generated from strains from Waterston lab and Ma et al., Du lab[60]	OS14872
unc-119(ed3) III; zuIs178 [his-72(1kb 5' UTR)::his-72::SRPVAT::GFP::his-72 (1KB 3' UTR) + 5.7 kb XbaI - HindIII unc-119(+)]; stIs10501 [ceh-36::H1-wCherry::his-24::mCherry + unc-119(+)]	CGC, Waterston lab	RW10598
stIs10501 [ceh-36::H1-wCherry::his-24::mCherry + unc-119(+)];wgIs707 [sptf-1::TY1::EGFP::3xFLAG + unc-119(+)] (May still have *unc-119(tm4063) III* or *unc-119(ed3) III*)	This study, generated from strains from Waterston lab	OS14282
unc-119(tm4063) III; wgIs707 [sptf-1::TY1::EGFP::3xFLAG + unc-119(+)]	CGC, Waterston lab	OP707
nsIs105 [hlh-17p::gfp] I	Shaham lab[52]	OS1914

nsIs105 [hlh-17p::gfp] I; eri-1 (mg366)	Shaham lab[52] Ruvkun lab[71]	OS8753
lin-26(n156) II	CGC[123]	MT156
nsIs105 [hlh-17p::gfp] I; lin-26(n156) II	This study	OS15214
ztf-29(gk561) III	CGC[124]	VC1238
nsIs105 [hlh-17p::gfp] I; ztf-29(gk561) III	This study	OS15122
nsIs105 [hlh-17p::gfp] I; ztf-29(gk561) III; nsEx7511[pKB001(ztf-29p(3kb)::ztf-29::ztf-29 3'UTR) + elt-2::mCherry]	This study	OS15508
ceh-43(ot406) III; vtIs1 [dat-1p::GFP + rol-6(su1006)] vsIs33 [dop-3::RFP] V	CGC[107]	OH7323
nsIs105 [hlh-17p::gfp] I; ceh-43(ot406) III	This study	OS14820
nsIs105 [hlh-17p::gfp] I; ceh-43(ot406) III; nsIs975 [mir-228p::2xNLS::iBlueberry + unc-122::RFP] X	This study	OS14781
nsIs105 [hlh-17p::gfp] I; nsIs975 [mir-228p::2xNLS::iBlueberry + unc-122::RFP] X	This study	OS13802
ceh-43(tm480) III; otIs287 [rab-3::NLS::YFP + rol-6(su1006)]; norEx41 [ceh-43 fosmid + dat-1::mCherry]	CGC[107], Mitani lab	OH10279
ceh-43(syb5073[ceh-43::SL2::GFP::H2B]) III	CGC[125]	PHX5073
ceh-43(syb5073[ceh-43::SL2::GFP::H2B]) III; nsIs975 [mir-228p::2xNLS::iBlueberry) + unc-122::RFP] X	This study	OS14922
nsIs105 [hlh-17p::gfp] I; ceh-43(ot406) III; nsEx7406[ceh-43 fosmid (WRM0633cC03) + elt-2::mCherry] (Line 1)	This study	OS15096
nsIs105 [hlh-17p::gfp] I; ceh-43(ot406) III; nsEx7407[ceh-43 fosmid (WRM0633cC03) + elt-2::mCherry] (Line 2)	This study	OS15097
nsIs105 [hlh-17p::gfp] I; ceh-43(ot406) III; nsEx7408[ceh-43 fosmid (WRM0633cC03) + elt-2::mCherry] (Line 3)	This study	OS15098
nsIs105 [hlh-17p::gfp] I; ceh-43(ot406) III; nsIs975 [mir-228p::2xNLS::iBlueberry + unc-122::RFP] X; nsEx7452 [ceh-43p::ceh-43 + pSL037 (nhr-2p::his-24::mCherry) + elt-2::mCherry] (Line 1)	This study	OS15331
nsIs105 [hlh-17p::gfp] I; ceh-43(ot406) III; nsIs975 [mir-228p::2xNLS::iBlueberry + unc-122::RFP] X; nsEx7453 [ceh-43p::ceh-43 + pSL037 (nhr-2p::his-24::mCherry) + elt-2::mCherry] (Line 2)	This study	OS15332
nsIs105 [hlh-17p::gfp] I; ceh-43(ot406) III; nsIs975 [mir-228p::2xNLS::iBlueberry + unc-122::RFP] X; nsEx7454 [ceh-43p::ceh-43 + pSL037 (nhr-2p::his-24::mCherry) + elt-2::mCherry] (Line 3)	This study	OS15333
nsIs105 [hlh-17p::gfp] I; ceh-43(ot406) III; nsIs975 [mir-228p::2xNLS::iBlueberry + unc-122::RFP] X; nsEx7498 [pros-1pS::ceh-43(cDNA) + elt-2::mCherry] (Line 1)	This study	OS15476
nsIs105 [hlh-17p::gfp] I; ceh-43(ot406) III; nsIs975 [mir-228p::2xNLS::iBlueberry + unc-122::RFP] X; nsEx7499 [pros-1pS::ceh-43(cDNA) + elt-2::mCherry] (Line 2)	This study	OS15477
nsIs105 [hlh-17p::gfp] I; ceh-43(ot406) III; nsIs975 [mir-228p::2xNLS::iBlueberry + unc-122::RFP] X; nsEx7500 [pros-1pS::ceh-43(cDNA) + elt-2::mCherry] (Line 3)	This study	OS15478
nsIs105 [hlh-17p::gfp] I; ceh-43(ot406) III; nsIs975 [mir-228p::2xNLS::iBlueberry + unc-122::RFP] X; nsEx7501 [pSL056 (sox-2p::ceh-43 cDNA::SL2::his-24::mCherry) + pSL046 (nhr-2p::his-24:TagBFP(I174A)) + elt-2::mCherry] (Line 1)	This study	OS15479
nsIs105 [hlh-17p::gfp] I; ceh-43(ot406) III; nsIs975 [mir-228p::2xNLS::iBlueberry + unc-122::RFP] X; nsEx7502 [pSL056 (sox-2p::ceh-43 cDNA::SL2::his-24::mCherry) + pSL046 (nhr-2p::his-24:TagBFP(I174A)) + elt-2::mCherry] (Line 2)	This study	OS15480

nsIs105 [hlh-17p::gfp] I; ceh-43(ot406) III; nsIs975 [mir-228p::2xNLS::iBlueberry + unc-122::RFP] X; nsEx7503 [pSL056 (sox-2p::ceh-43 cDNA::SL2::his-24::mCherry) + pSL046 (nhr-2p::his-24:TagBFP(I174A)) + elt-2::mCherry] (Line 3)	This study	OS15481
nsIs105 [hlh-17p::gfp] I; ceh-43(ot406) III; nsIs975 [mir-228p::2xNLS::iBlueberry + unc-122::RFP] X; nsEx7504 [pSL047 (mir-228p::ceh-43 cDNA::SL2::his-24::mCherry) + elt-2::mCherry] (Line 1)	This study	OS15482
nsIs105 [hlh-17p::gfp] I; ceh-43(ot406) III; nsIs975 [mir-228p::2xNLS::iBlueberry + unc-122::RFP] X; nsEx7504 [pSL047 (mir-228p::ceh-43 cDNA::SL2::his-24::mCherry) + elt-2::mCherry] (Line 2)	This study	OS15483
nsIs105 [hlh-17p::gfp] I; ceh-43(ot406) III; nsIs975 [mir-228p::2xNLS::iBlueberry + unc-122::RFP] X; nsEx7504 [pSL047 (mir-228p::ceh-43 cDNA::SL2::his-24::mCherry) + elt-2::mCherry] (Line 3)	This study	OS15484
nsIs105 [hlh-17p::gfp] I; ceh-43(ot406) III; nsIs975 [mir-228p::2xNLS::iBlueberry + unc-122::RFP] X; nsEx7504 [pSL047 (mir-228p::ceh-43 cDNA::SL2::his-24::mCherry) + elt-2::mCherry] (Line 4)	This study	OS15485
nsIs105 [hlh-17p::gfp] I; ceh-43(ot406) III; nsIs975 [mir-228p::2xNLS::iBlueberry + unc-122::RFP] X; nsEx7431 [ceh-43 fosmid (WRM0633cC03) + pSL037 (nhr-2p::his-24::mCherry) + elt-2::mCherry]	This study	OS15197
nsIs105 [hlh-17p::gfp] I; ceh-43(tm480) III; nsIs975 [mir-228p::2xNLS::iBlueberry + unc-122::RFP] X; nsEx7450 [ceh-43 fosmid (WRM0633cC03) + pSL037 (nhr-2p::his-24::mCherry) + elt-2::mCherry]	This study	OS15437
nsIs105 [hlh-17p::gfp] I; nsEx7490 [pSL048 (Phsp16.41::ceh-43 cDNA::SL2::his-24::mCherry::let-858 3'UTR) + elt-2::mCherry]	This study	OS15465
nsIs408[ceh-24::GFP + odr-1::RFP]	Shaham lab[50]	OS7698
ceh-43(ot406) III; nsIs408 [ceh-24::GFP + odr-1::RFP]	This study, Shaham lab[50]	OS15207
mgIs18 [ttx-3p::GFP] IV	CGC	OH99
mgIs18 [ttx-3p::GFP] IV; nsIs978 [mir-228p::2xNLS::iBlueberry + unc-122::RFP]	This study	OS15298
ceh-43(ot406) III; mgIs18 [ttx-3p::GFP] IV	This study	OS15212
ceh-43(ot406) III; mgIs18 [ttx-3p::GFP] IV; nsIs978 [mir-228p::2xNLS::iBlueberry + unc-122::RFP]	This study	OS15299
ceh-43(ot406) III; mgIs18 [ttx-3p::GFP] IV; nsIs978 [mir-228p::2xNLS::iBlueberry + unc-122::RFP]; nsEx7459 [ceh-43p::ceh-43 + pSL037 (nhr-2p::his-24::mCherry) + elt-2::mCherry] (Line 1)	This study	OS15351
ceh-43(ot406) III; mgIs18 [ttx-3p::GFP] IV; nsIs978 [mir-228p::2xNLS::iBlueberry + unc-122::RFP]; nsEx7460 [ceh-43p::ceh-43 + pSL037 (nhr-2p::his-24::mCherry) + elt-2::mCherry] (Line 2)	This study	OS15352
ceh-43(ot406) III; mgIs18 [ttx-3p::GFP] IV; nsIs978 [mir-228p::2xNLS::iBlueberry + unc-122::RFP]; nsEx7461 [ceh-43p::ceh-43 + pSL037 (nhr-2p::his-24::mCherry) + elt-2::mCherry] (Line 3)	This study	OS15353
syb9593 [hsp-16.2p::lox::degron::dam::vhhGFP4::unc-54 3'UTR; unc-119(+)] II; nsIs975 [mir-228p::2xNLS::iBlueberry + unc-122::RFP] X; nsIs1044 [hlh-17p::nls::tagrfp]	This study (*syb9593* is modified from IS3675 from the Peter Meister lab)[86]	OS15367
syb9593 [hsp-16.2p::lox::degron::dam::vhhGFP4::unc-54 3'UTR; unc-119(+)] II; ceh-43(syb9080[ceh-43::3xGAS::GFP::AID]) III; nsIs975 [mir-228p::2xNLS::iBlueberry + unc-122::RFP] X; nsIs1044 [hlh-17p::nls::tagrfp]	This study (*syb9593* is modified from IS3675 from the Peter Meister lab)[86]	OS15368
nsIs978 [mir-228p::2xNLS::iBlueberry + unc-122::RFP]; nsIs616 [glt-1p::gfp; unc-122::RFP]	This study, Shaham lab[48]	OS15160
ceh-43(ot406) III; nsIs978 [mir-228p::2xNLS::iBlueberry + unc-122::RFP]; nsIs616 [glt-1p::gfp; unc-122::RFP]	This study, Shaham lab[48]	OS15162

ujIs113 [pie-1p::mCherry::H2B::pie-1 3'UTR + nhr-2p::his-24::mCherry::let-858 3'UTR + unc-119(+)] II; wgIs500 [ceh-26::TY1::EGFP::3xFLAG + unc-119(+)]	This study, generated from strains from Murray lab[126] and the Regulatory Element Project of modENCODE[127,128]	OS14597
ces-2(dev112([mNeonGreen::ces-2]) I; ujIs113 [pie-1p::mCherry::H2B::pie-1 3'UTR + nhr-2p::mCherry::his-24::let-858 3'UTR + unc-119(+)] II	CGC, Du lab[60]	SYS443
ujIs113 [pie-1p::mCherry::H2B::pie-1 3'UTR + nhr-2p::mCherry::his-24::let-858 3'UTR + unc-119(+)] II; sox-2(dev153([sox-2::mNeonGreen]) X	CGC, Du lab[60]	SYS516
lim-7(dev125([mNeonGreen::lim-7]) I; ujIs113 [pie-1p::mCherry::H2B::pie-1 3'UTR + nhr-2p::mCherry::his-24::let-858 3'UTR + unc-119(+)] II	CGC, Du lab[60]	SYS473
ieSi57 [eft-3p::TIR1::mRuby::unc-54 3'UTR + Cbr-unc-119(+)] II; unc-119(ed3) III	CGC, Dernburg lab[84]	CA1200
nsIs105 [hlh-17p::gfp] I; ieSi57 [eft-3p::TIR1::mRuby::unc-54 3'UTR + Cbr-unc-119(+)] II; ceh-43(syb9080[ceh-43::3xGAS::GFP::AID]) III	This study	OS15343
nsIs105 [hlh-17p::gfp] I; ieSi57 [eft-3p::TIR1::mRuby::unc-54 3'UTR + Cbr-unc-119(+)] II	This study	OS15344
nsIs105 [hlh-17p::gfp] I; ceh-43(syb9080[ceh-43::3xGAS::GFP::AID]) III	This study	OS15345
ieSi57 [eft-3p::TIR1::mRuby::unc-54 3'UTR + Cbr-unc-119(+)] II; ceh-43(syb9080[ceh-43::3xGAS::GFP::AID]) III	This study	OS15346
ieSi57 [eft-3p::TIR1::mRuby::unc-54 3'UTR + Cbr-unc-119(+)] II; ceh-43(syb9080[ceh-43::3xGAS::GFP::AID]) III; nsIs978 [mir-228p::2xNLS::iBlueberry + unc-122::RFP]; nsIs616 [glt-1p::gfp; unc-122::RFP]	This study	OS15505
ieSi57 [eft-3p::TIR1::mRuby::unc-54 3'UTR + Cbr-unc-119(+)] II; nsIs978 [mir-228p::2xNLS::iBlueberry + unc-122::RFP]; nsIs616 [glt-1p::gfp; unc-122::RFP]	This study	OS15503
ceh-43(syb9080[ceh-43::3xGAS::GFP::AID]) III; nsIs978 [mir-228p::2xNLS::iBlueberry + unc-122::RFP]; nsIs616 [glt-1p::gfp; unc-122::RFP]	This study	OS15504
ieSi57 [eft-3p::TIR1::mRuby::unc-54 3'UTR + Cbr-unc-119(+)] II; ceh-43(syb9080[ceh-43::3xGAS::GFP::AID]) III; nsIs978 [mir-228p::2xNLS::iBlueberry + unc-122::RFP]	This study	OS15502
Oligonucleotides		
pros-1 promoter forward primer: GTTTGGTTACGGGATGGC	This study	NA
pros-1 promoter reverse primer: TGATGACGTCACTAGCTA	This study	NA
sox-2 promoter forward primer: CGGAAACGAGTAAAACCC	This study	NA
sox-2 promoter reverse primer: CTTGTTAAACAACAATGA	This study	NA
mir-228 promoter forward primer: GTGACGTCATACTCTTGC	This study	NA
mir-228 promoter reverse primer: AGTTTTTGGGAGGCGACG	This study	NA
hsp-16.41 promoter forward primer: ACGTTGAGCTGGACGGA	This study	NA
hsp-16.41 promoter reverse primer: CTTTCGAAGTTTTTTA	This study	NA
ceh-43 genomic locus PCR fragment (*ceh-43p::ceh-43*) forward primer: TTGATGAACTCCTGAAACC	This study	NA
ceh-43 genomic locus PCR fragment (*ceh-43p::ceh-43*) reverse primer: AGACATGAGGAAGGGAAAG	This study	NA
Recombinant DNA		

pSL037 (*nhr-2p::his-24::mCherry::let-858 3'UTR*)	This study, cloned from sequence amplified from *ujIs113* (Murray lab[126])	NA
pSL046 (*nhr-2p::his-24:TagBFP(I174A)::let-858 3'UTR*)	This study	NA
pSL047 (*mir-228p::ceh-43 cDNA::SL2::his-24::mCherry::let-858 3'UTR*)	This study	NA
pSL048 (*hsp16.41p::ceh-43 cDNA::SL2::his-24::mCherry::let-858 3'UTR*)	This study	NA
pSL056 (*sox-2pS::ceh-43 cDNA::SL2::his-24::mCherry::let-858 3'UTR*)	This study	NA
pKB001 (*ztf-29p::ztf-29::ztf-29 3'UTR*)	This study	NA
WRM0633Cc03 fosmid	*C. elegans* Vancouver fosmid library, Source BioScience	NA
Software and algorithms		
Cell Ranger v7.1.0	10x Genomics	https://www.10xgenomics.com/support/software/cell-ranger/latest
CellBender v0.2.1	Broad Institute	https://github.com/broadinstitute/CellBender
Seurat v4	Integrated analysis of multimodal single-cell data[62]	https://satijalab.org/seurat/
SeqPlots v3.0.12	SeqPlots – Interactive software for exploratory data analyses, pattern discovery and visualization in genomics[129]	https://przemol.github.io/seqplots/
StarryNite	Automated cell lineage tracing in *Caenorhabditis elegans*[130]	https://github.com/zhirongbaolab/StarryNite
AceTree	AceTree: a tool for visual analysis of *Caenorhabditis elegans* embryogenesis	https://github.com/zhirongbaolab/AceTree

EXPERIMENTAL MODEL AND STUDY PARTICIPANT DETAILS

Husbandry conditions of C. elegans

C. elegans were maintained at 20 °C on NGM agar plates supplemented with cholesterol and seeded with OP50 *E.coli* strain as food, following standard protocols[131,132].

Mouse

All experiments using mice were reviewed and approved by the Rockefeller University IACUC and adhere to the institutional and NIH rules and regulations. We utilized two mouse strains purchased from the Jackson Laboratory: C57Bl/6J mice (JAX strain # 000664) and astrocyte specific TRAP mouse line in which L10a-GFP is expressed under the astrocyte specific *Aldh1l1* promoter[133], *b6;fvb-tg(aldh1l1-egfp/rpl10a)jd130htz/j* (JAX strain # 030247). Mice were group housed in conventional rooms in a 12-hour light/dark cycle and access to food and water ad libitum. Mice were perfused by transcardial perfusion at 20-24 weeks. Prior to transcardial perfusion and tissue harvesting, mice were anesthetized with a lethal intraperitoneal injection of ketamine (300 mg/kg in saline).

METHOD DETAILS

Preparation of synchronized embryos for single-cell dissociation

C. elegans embryos were harvested using a standard hypochlorite bleaching protocol[132] and incubated in M9 buffer[132] without food until L1 larvae hatched. L1s were then plated onto standard 150 mm NGM plates seeded with *E. coli* OP50, with no more than 15,000 L1s per plate, and raised at 20°C. Plates were monitored regularly, and concentrated OP50 was added as needed when food became scarce. After 48–48.5 hours (timing may vary by strain), young adult animals were checked under a dissecting microscope to assess embryo content. Three fields of view from each of three plates were examined. When 20–30% of animals had a single embryo in one arm of the gonad, the population was collected via hypochlorite bleaching. The time of hypochlorite treatment was designated as t = 0. Embryos that survived the bleach treatment were washed three times with M9 and once with egg buffer[134], then brought to 2 mL total volume in a 15 mL Falcon

tube. To remove debris, embryos were purified via one round of sucrose density gradient centrifugation: 4 mL of 50% sucrose solution was added, vortexed to mix, and centrifuged at 450 g for 3 minutes. A layer of pure embryos was collected from the top, while debris and animal carcasses were pelleted at the bottom. Embryos were transferred with a glass pipette to a fresh 15 mL tube and washed three times with egg buffer (fill to 15 mL, centrifuge at 450 g for 3 minutes). After the final wash, embryos were resuspended in 10 mL egg buffer and grown on a rotor at 20°C.

Single-cell dissociation, FACS, and single-cell RNA sequencing

At the desired developmental stage, embryos were spun down, and the volume was reduced to 0.5 mL. Chitinase (15.6 µL of 20 mg/mL stock; Sigma C8241-25UN) was added to reach a final concentration of 1 U/mL. Embryos were then incubated on a shaker/rotor at 20 °C for 25 minutes. Following digestion, embryos were pelleted with a desk-top centrifuge, the chitinase solution was removed, and 100 µL of freshly prepared pronase (15 mg/mL, Sigma P8811-1G) was added. Embryos were dissociated by repeated passage through a 22-gauge, 1½-inch needle attached to a 3 mL syringe for 2–3 minutes. Dissociation was stopped by adding 1 mL ice-cold egg buffer with 1% BSA. From this point onward, all steps were carried out on ice. The time of ice-cold BSA addition (i.e. cells put on ice) was considered the endpoint (t_end). Dorsal samples were collected at t_end = 240, 270 (two replicates), 330 (two replicates), and 420 minutes. Ventral samples were collected at t_end = 240, 330, and 420 minutes.

Cells were centrifuged at 1,500 g for 5 minutes at 4 °C and washed three times with 1 mL ice-cold egg buffer containing 0.15% BSA. During the final wash, a Millex™-SV 5.0 µm

filter was pre-wetted with 1 mL egg buffer with 0.15% BSA. After washing, the cell pellet was resuspended in 500 µL ice-cold egg buffer with 0.15% BSA and passed through the filter into a 1.7 mL low-retention tube (Denville Scientific Inc., Cat. C2170). Residual cells were recovered by rinsing the filter with an additional 0.5–0.6 mL egg buffer into the same tube. Cell density was measured with a hemocytometer and adjusted to ≤1 × 10^7 cells/mL prior to FACS. DAPI (10 ng/mL, diluted from Thermo Scientific™ Cat. 62248) was used to exclude dead cells during the sorting.

Collection tubes for FACS were pre-coated overnight at 4 °C with egg buffer containing 5% BSA. Target cell populations were sorted into these pre-coated tubes. DAPI (10 ng/mL final concentration) was used for dead cell exclusion. Sorted cells were immediately processed for single cell capture and library preparation using the 10x Genomics Chromium Next GEM Single Cell 3' Reagent Kits v3.1. Each sample was loaded into a separate channel. For dorsal and ventral samples collected at t_end = 420 minutes, 20,000 cells were loaded. For all other samples, 10,000 cells were loaded.

Single-cell RNA-seq data processing, quality control, and integration

The *C. elegans* reference genome (WBcel235) was appended with fluorescent marker transgene sequences. For each sample, sequencing reads were aligned to the modified reference genome using 10x Genomics Cell Ranger (v7.1.0) with default settings, including the inclusion of intronic reads. The resulting feature-barcode matrices were processed using the CellBender (v0.2.1) pipeline[135] for ambient RNA removal. Filtered matrices were then imported into Seurat (v4)[62] for downstream analysis. Cells with fewer

than 200 detected genes (nFeature_RNA ≤ 200) or with >5% mitochondrial RNA content were excluded.

Doublets were identified using the scDblFinder pipeline[136] and DoubletFinder[137]. For CEPshD lineages defined based on *pros-1* and *ham-2* expression, doublets were identified by scDblFinder. Clusters dominated by doublets were removed. For remaining clusters, doublets identified by scDblFinder were also removed. For the ventral dataset, doublets were identified with both methods, and clusters with >20% doublet rates according to both methods were excluded. Additional intermediate clusters were also removed if their top enriched genes were predominantly mitochondrial, or if they were located between major lineage branches and consistently co-expressed marker genes from both. Finally, lineages not belonging to targeted lineages shown in Figure 1B were excluded from further analysis.

For the ventral dataset, 2000 integration features were used to perform Seurat (v4) integration to remove batch effects. Integration did not affect the temporal relationships among cells, but did eliminate batch differences between samples collected at the same developmental time.

Cell type annotation and embryo time estimation

Cell lineages and types were annotated based on marker genes curated from previously published datasets[53,60,138,139]. For the ventral dataset, only cells from the ABpl/rpaa lineage were retained for analysis. For the dorsal dataset, initial cell type labels were assigned via label transfer using Seurat's FindTransferAnchors() and TransferData() functions, referencing the VisCello dataset[53]. Two parallel rounds of label transfer were

conducted: one using only ABa lineage cells as the reference, and another using the full VisCello dataset. Final annotations were refined based on these results in conjunction with curated lineage data from the literature.

Embryo time analysis was performed according to a previously published method[53], with code generously provided by Dr. John I. Murray. Briefly, gene expression profiles of each single cell were compared to a published whole-embryo gene expression time course[55]. Time-dependent genes from the reference dataset, defined as those with >0.6 autocorrelation and >1.5 standard deviation in expression, were retained for analysis. For each single cell, genes with $\log_2$(expression) <1 or >7 were excluded. Pearson correlation coefficients were then calculated against all time points in the reference time course. After applying LOESS[140] to the correlation profile, the time point with the maximal correlation was assigned as the estimated embryo time.

Differential Gene Expression and GO Enrichment Analysis

Differential gene expression (DEG) analyses were performed using the FindMarkers() and FindAllMarkers() functions with default settings in Seurat (v4). For heatmap visualization in Figure 2B, the top six differentially expressed transcription factors were selected and supplemented with transcription factors broadly expressed across dorsal and ventral CEPsh astrocyte lineages. These were defined as transcription factors enriched in CEPsh astrocyte lineages by ≥0.5 $\log_2$FC and expressed in >50% of cells, but not highly differentially expressed within CEPsh astrocyte lineage subclusters, i.e., with all subcluster $\log_2$FC enrichment <1.3. Converged CEPsh enriched genes in Figure 2G were defined as those with log2FC >1.5 and adjusted p-value (p_val_adj) <0.05. GO

enrichment analyses were performed using the enrichGO() function in the clusterProfiler package[141,142].

To identify dynamically expressed genes in CEPsh astrocyte lineages (Figure 6D), we separately analyzed cells from the CEPshD lineage (dorsal dataset) and CEPshV lineage (ventral dataset) as two independent datasets (see Figure 2A). For each dataset, two complementary approaches were applied: (1) the FindAllMarkers() function from Seurat (v4) was used to identify differentially expressed genes across Seurat clusters, selecting genes with avg_log_2FC > 0 and p_val_adj < 0.05; and (2) the graph_test() function from Monocle3[143–145] was used to identify genes whose expression varies significantly along pseudotime trajectories, using a cutoff of q_value < 0.05. Only genes identified by both methods were retained as dynamically expressed genes. The resulting gene sets from the dorsal and ventral datasets were then combined to generate a union list of dynamically expressed genes in CEPsh astrocyte lineages.

L2-L3 CEPsh astrocyte enriched genes (Figure S6F) were obtained from a previously published RNA sequencing study (Katz et al., 2019)[48]. To identify adult CEPsh astrocyte enriched genes (Figure S6G), single-cell gene expression data was obtained from a recently published atlas (Purice et al., 2025)[79]. CEPsh astrocyte enriched genes were identified using FindMarkers() function from Seurat (v4) with avg_log2FC > 0 and p_val_adj < 0.05.

NanoDam profiling

To prepare animals for NanoDam profiling, strains carrying the NanoDam transgene alone or together with an endogenously GFP-tagged CEH-43 were maintained on *dam*–

/dcm– E. coli (NEB C2925) for at least three generations without starvation. Nine 55 mm plates densely populated with gravid adults were bleached to collect embryos. The resulting synchronized L1s were placed onto 90 mm NGM plates seeded with *dam–/dcm– E. coli*, grown at 20°C, and harvested at the L4 stage.

Two biological replicates were obtained for each condition and processed in parallel to minimize batch effects. Genomic DNA was extracted using the QIAamp® DNA Micro Kit (Qiagen), following the manufacturer's protocol for "Isolation of Genomic DNA from Tissues." Downstream steps followed a previously published DamID protocol[146]. Genomic DNA was digested with DpnI (NEB), and DamID adaptors were ligated using T4 DNA ligase (NEB). Ligated DNA was then digested with DpnII (NEB) and purified using homemade Sera-Mag beads prepared from Cytiva Sera-Mag SpeedBeads and 20% (w/v) PEG-8000 following the method of Rohland and Reich[147]. DNA was amplified with Advantage 2 cDNA Polymerase (Clontech) and quality-checked on a 0.8% agarose gel. Amplicons were purified using the QIAquick PCR Purification Kit (Qiagen), quantified with Qubit, and sonicated to ~300–400 bp fragments using a Bioruptor Plus. DamID adaptors were removed with AlwI (NEB), followed by one round of bead purification. End-repair was performed using an enzyme mix of T4 DNA polymerase, Klenow fragment, and T4 polynucleotide kinase (NEB), followed by 3′ adenylation with Klenow Fragment (3′→5′ exo–) (NEB) and ligation of indexed sequencing adaptors. Libraries were bead purified twice, amplified with NEBNext PCR Master Mix, purified again, checked for quality on a TapeStation, and pooled for Illumina sequencing.

NanoDam peak analysis

Demultiplexed data were analyzed using a previously published pipeline (GitHub: https://github.com/AHBrand-Lab/NanoDam_analysis)[85]. CEH-43 NanoDam signal z-score aggregation plots were generated using SeqPlots (v3.0.12)[129]. CEH-43 peaks with FDR $<10^{-25}$ were annotated to nearby genes using both bedtools (v.2.28) and HOMER (*annotatePeaks.pl*, v.4.11). Gene lists obtained from both methods were merged to create a unified list of candidate CEH-43 target genes.

Comparative analysis with mammalian astrocytes

Mammalian astrocyte single-cell RNA sequencing data were obtained from two previous publications[97,98], and re-analyzed according to the workflow described in these papers. Human and mouse astrocyte enriched genes were identified using FindAllMarkers() function in Seurat (v4). Ortholog matching between human and *C. elegans* genes was done with OrthoList 2[148], and ortholog matching between mouse and human genes was done with Biomart on Ensembl[149]. The module scores of the top 50 mammalian astrocyte/neuron enriched genes in *C. elegans* CEPsh astrocyte lineages were calculated with the AddModuleScore() function. The output module scores represent the average expression of the input gene set in each cell, normalized against a background of control genes with similar overall expression levels. The scores reflect the relative enrichment of mammalian astrocyte- or neuron-enriched genes in individual *C. elegans* cells.

Genes enriched in *C. elegans* CEPsh astrocytes and in different human/mouse astrocytes with average $\log_2$FC >0.5 and adjusted p-value <0.05 were identified. Shared orthologs were identified. *p*-values are as follows:

1. Wang et al., 2025 Human

Astrocyte enriched genes, compared with Converged_CEPsh astrocytes: 5.27×10^{-143}, 4.03×10^{-163}, 1.50×10^{-86}, 1.92×10^{-157}, 3.11×10^{-202}, 3.61×10^{-18}, 1.50×10^{-42}, 8.36×10^{-36}, 2.33×10^{-6}, 6.55×10^{-70}

Interneuron enriched genes, compared with URAV: 1.91×10^{-68}, 1.26×10^{-50}, 1.84×10^{-49}, 3.53×10^{-8}, 7.60×10^{-47}, 3.86×10^{-7}, 2.00×10^{-3}, 4.44×10^{-27}, 4.00×10^{-3}, 1.22×10^{-23}

2. Frazel et al., 2023 Human

Astrocyte (1) enriched genes, compared with Converged_CEPsh astrocytes: 7.35×10^{-132}, 4.50×10^{-131}, 7.12×10^{-77}, 7.65×10^{-129}, 8.30×10^{-192}, 1.58×10^{-39}, 9.56×10^{-55}, 3.64×10^{-11}, 7.35×10^{-7}, 2.62×10^{-89}

Astrocyte (2) enriched genes, compared with Converged_CEPsh astrocytes: 6.85×10^{-43}, 2.47×10^{-49}, 6.29×10^{-21}, 8.70×10^{-28}, 1.64×10^{-29}, 7.20×10^{-18}, 2.75×10^{-22}, 2.48×10^{-11}, 8.53×10^{-04}, 4.90×10^{-40}

Neuron enriched genes, compared with URAV: 2.21×10^{-4}, 3.42×10^{-13}, 9.16×10^{-1}, 6.00×10^{-3}, 5.23×10^{-34}, 5.70×10^{-14}, 4.72×10^{-7}, 3.20×10^{-30}, 2.32×10^{-7}, 1.86×10^{-1}

Frazel et al., 2023 Mouse

Astrocyte enriched genes, compared with Converged_CEPsh astrocytes: 3.47×10^{-75}, 1.90×10^{-69}, 5.04×10^{-42}, 2.33×10^{-47}, 6.60×10^{-118}, 3.50×10^{-47}, 3.47×10^{-75}, 1.18×10^{-55}, 8.42×10^{-1}, 9.93×10^{-55}

Neuron enriched genes, compared with URAV: 2.13×10^{-31}, 2.98×10^{-44}, 2.85×10^{-13}, 2.22×10^{-32}, 1.20×10^{-5}, 1.61×10^{-50}, 9.95×10^{-48}, 3.80×10^{-2}, 1.58×10^{-42}, 7.37×10^{-25}

RNAi screen

The RNAi screen was performed using the standard RNAi feeding method[150]. RNAi bacterial clones were obtained from the Ahringer RNAi feeding library[151]. Overnight cultures of RNAi bacteria were resuspended in M9 buffer and plated onto NGM plates containing 1 mM IPTG (Sigma). Plates were dried overnight. L4-stage *C. elegans* were first transferred to empty plates to remove residual bacteria from their bodies and then moved to the RNAi plates. For each genotype, F1 embryos, L1 larvae, and L4 larvae were scored for CEPsh astrocyte reporter expression.

Fluorescence imaging and quantification

Fluorescence imaging was performed using a Zeiss Imager M2 microscope equipped with an AxioCam MRm 1.4 camera and a 63x/1.4 NA oil immersion objective. Confocal images were acquired using a Zeiss LSM 900 inverted laser scanning confocal microscope with a 63x/1.4 NA oil objective. Animals were immobilized in 200 mM sodium azide either on 1% agar pads or with 20 μm polystyrene microbeads. For quantification of *glt-1p::gfp* expression in Figure 6Q, regions of interest were manually drawn around nuclei of CEPsh astrocytes. Mean fluorescence intensity was measured at the central z-plane of the cell body. Fluorescence intensities from wild-type and *ceh-43(ot406)* animals were normalized to the average intensity of the wild-type group.

iSPIM imaging and lineage tracking

A custom-built scanning iSPIM microscope was used for embryo imaging[57,58]. Two-cell stage embryos were placed on a dried poly-L-lysine spot in the center of a Fisherbrand 24 × 50-1 microscope cover glass (Thermo Fisher Scientific, Cat. 12-545-F). Embryos

were immersed in M9 buffer within an imaging chamber and imaged for 10 hours at 75-second intervals. Lineage tracking was performed with StarryNite[130], and lineages were visualized with AceTree[152].

CEPsh astrocyte rescue experiment

Rescue experiments in *ceh-43(ot406)* mutants were performed using the following DNA injection mixes:

Fosmid-based rescue: a *ceh-43* fosmid (15 ng/μL) was co-injected with *elt-2::mCherry* plasmid (10 ng/μL).

Genomic DNA rescue: *ceh-43p::ceh-43* genomic PCR product (amplified using oSL265 and oSL398, 10 ng/μL) was co-injected with pSL037(*nhr-2p::his-24::mCherry*, 15 ng/μL) and *elt-2::mCherry* plasmid (10 ng/μL).

ceh-43 cDNA driven by different promoters: pSL056(*sox-2p::ceh-43 cDNA::SL2::his-24::mCherry*) was co-injected with *elt-2::mCherry* plasmid (10 ng/μL) and pSL046(*nhr-2p::his-24::TagBFP(I174A)*, 10 ng/μL). The *pros-1* promoter (amplified using oSL453 and oSL457 from the genome) was fused to *ceh-43 cDNA::SL2::his-24::mCherry::let-858 3'UTR* by PCR. The fusion product (10 ng/μL) was injected with *elt-2::mCherry* plasmid (10 ng/μL). pSL047(*mir-228p::ceh-43 cDNA::SL2::his-24::mCherry*, 10 ng/μL) was co-injected with *elt-2::mCherry* plasmid (10 ng/μL).

The rescue experiment in *ztf-29(gk561)* mutants was performed using the following DNA injection mixes:

Genomic DNA rescue: the *ztf-29* genomic locus (*ztf-29p(3kb)::ztf-29::ztf-29 3'UTR*, cloned into pKB001, 15 ng/μL) was co-injected with *elt-2::mCherry* plasmid (10 ng/μL).

All injection mixes were supplemented with pBluescript plasmid to reach a final DNA concentration of 100 ng/µL.

Mosaic analysis

We performed mosaic analysis with two different *ceh-43* mutants. *ceh-43(ot406)* mutant animals were generated that harbor extrachromosomal transgenic DNA arrays that are stochastically transmitted to daughter cells during cell divisions. *ceh-43* fosmid was injected (15 ng/µL) together with a ubiquitous mCherry co-injection marker (*nhr-2p::his-24::mCherry*, 10 ng/µL) to mark the existence of the array. In a separate strategy, *mir-228p::ceh-43(cDNA)::SL2::H1-mCherry* (10 ng/µL) was injected, with H1-mCherry indicating sites *mir-228p* expression. For the embryonic lethal *ceh-43(tm480)* mutant, *ceh-43(tm480)/mT1* animals were injected with *ceh-43* fosmid (5 ng/µL) and *nhr-2p::his-24::mCherry* (15 ng/µL). Rescue array positive and mT1 balancer negative animals were picked as *ceh-43(tm480)* homozygous mutant animals for mosaic analysis.

Heat-shock induction of *ceh-43* expression

A heat-shock construct (*hsp16.41p::ceh-43 cDNA::SL2::his-24::mCherry::let-858 3'UTR*) was injected at 10 ng/µl, together with *elt-2*::mCherry (10 ng/µl) as a co-injection marker. Mixed-stage transgenic animals were heat-shocked at 32 °C for 10 minutes, allowed to recover at 20 °C for 4-6 hours, and then imaged and scored for reporter induction.

Cell culture

Mouse primary astrocytes (isolated from E14 or E15 mice, Lonza, Cat. No. M-ASM-330) were cultured following a protocol adapted from the manufacturer's instructions. Briefly, cells were seeded onto multi-well plates pre-coated with poly-D-lysine (Sigma, Cat. No. P1024-50MG) and laminin (Gibco, Cat. No. 23-017-015) immediately after thawing. Cultures were maintained at 37 °C in a humidified incubator with 5% CO_2. Eight hours after initial attachment, the medium was replaced with fresh growth medium. A half-medium change was performed on day 7, followed by medium changes every 4–5 days until the cultures reached confluence. Cells were then passaged once onto coverslips and maintained for 8 days before fixation to analyze immature astrocytes.

The growth medium was the AGM™ Astrocyte Medium BulletKit (Lonza, Cat. No. CC-3186), which includes fetal bovine serum (FBS), L-glutamine, GA-1000, ascorbic acid, human epidermal growth factor (hEGF), and insulin.

Immunostaining and confocal imaging

Immunostaining protocol on cultured astrocytes is as follows. Primary astrocytes (isolated from E14 or E15 mice, Lonza, Cat. M-ASM-430) grown on coverslips were fixed with 4% paraformaldehyde for 20 minutes and rinsed three times with DPBS (Gibco, Cat. 14190-144, 10 minutes each). Cells were permeabilized in 0.2% Triton X-100 (Sigma, Cat. T8787) prepared in 10% normal goat serum (NGS, Vector Laboratories, Cat. S-1000-20) for 15 minutes, followed by three DPBS washes (5 minutes each). After blocking with 10% NGS for 2 hours at room temperature, cells were incubated overnight at 4 °C with the following primary antibodies: rabbit anti-DLX1 (1:500; Cell Signaling Technology, Cat. 96585), rabbit anti-DLX2 (1:500, Proteintech, Cat. 26244-1-AP), and chicken anti-GFAP

(1:500; Aves Labs, Cat. GFAP). The next day, coverslips were washed three times with DPBS (5 minutes each) and incubated for 1 hour at room temperature with the following secondary antibodies (all at 1:1000): Alexa Fluor™ 488 Goat anti-Rabbit IgG (H+L) (Invitrogen, Cat. A-11008) and Alexa Fluor™ 594 Goat anti-Chicken IgY (H+L) (Invitrogen, Cat. A-11042). Cells were then washed three times with 1× PBST (DPBS containing 0.05% Tween-20 (Sigma, Cat. P9416), 5 minutes each) and incubated with Hoechst 33342 (1:10,000 dilution; Cat. 62249) for 5 minutes at room temperature, followed by three washes with DPBS (5 minutes each). Coverslips were mounted using SlowFade Gold Antifade Mountant (Invitrogen, Cat. S36940). Images were acquired using a Zeiss scanning confocal microscope (LSM900).

The protocol for immunocytochemistry on mouse brain slices was adapted from a published method[153]. Briefly, mice were perfused intracardially with 20 mL of ice-cold 1× PBS, followed by 20 mL of 4% paraformaldehyde (PFA) in 1× PBS. Brains were post-fixed in 4% PFA for 1-3 hours or overnight. Brains were then cryopreserved in 5% sucrose in 1× PBS for 1 hour, followed by 15% and 30% sucrose. Brains were embedded in OCT compound and stored in a -80 °C freezer until sectioning. Cryostat sections (16-20 μm thick) were collected and stored at -80 °C in air-tight boxes until use. For staining, sections were air-dried for 2 hours and washed three times (5 min each) in 1× PBS. Blocking was performed for 1 hour at room temperature in 10% normal goat or donkey serum with 0.2% Triton X-100 in 1× PBS. Primary antibodies, diluted in antibody diluent (5% normal goat serum (Vector Laboratories, Cat. S-1000-20) and 0.2% Triton X-100 in 1× PBS), were applied overnight at 4 °C. After washing the sections in 1× PBS with 0.2% Triton X-100, sections were incubated for 1 h at room temperature with appropriate fluorescent

secondary antibodies and nuclei stain DAPI, diluted in antibody diluent, in an airtight black humidified chamber box. Sections were then washed in 1× PBS, coverslipped with anti-fade mounting medium, and imaged using a confocal microscope.

Following antibodies and dilutions were used in this study: DLX1 (Cell Signaling, Cat. 96585, dilution 1:500), DLX2 (Proteintech, Cat. 26244-1-AP; dilution 1:250), GFP (Abcam, Cat. ab13970, 1:500), and secondary antibodies: Alexa Fluor 568 goat-anti-rabbit IgG (H+L) highly cross-absorbed (Invitrogen, Cat. A11036), Alexa Fluor 488 goat anti-chicken IgY (H+L) highly cross-absorbed (Invitrogen, Cat. A32931) diluted at 1:500 in antibody diluent.

Confocal images were acquired using a Zeiss LSM 900 microscope. Maximum intensity projections were generated in Fiji from z-stacks with 0.5-1 μm optical sections. Images were cropped and adjusted for brightness and contrast in Photoshop.

QUANTIFICATION AND STATISTICAL ANALYSIS

For quantification of *glt-1p::gfp* expression shown in Figure 6Q, regions of interest (ROIs) were manually drawn around the nuclei of CEPsh glia based on the *mir-228p::2xNLS::iBlueberry* channel. Mean fluorescence intensity was measured at the central z-plane of the cell body. Fluorescence intensities from both wild-type and *ceh-43(ot406)* animals were normalized to the average intensity of the wild-type group.

Statistical analysis was performed with GraphPad Prism 10 (v10.5.0) and R (v4.2.2). All statistical details can be found in figure legends.